QUALITY ASSURANCE OF FLEXIBLE AND SEMI-FLEXIBLE PAVEMENT USING GROUND-PENETRATING RADAR

XIN SUI

PhD

The Hong Kong Polytechnic University

2026

The Hong Kong Polytechnic University

Department of Civil and Environmental Engineering

Quality assurance of flexible and semi-flexible pavement using ground-penetrating radar

Xin Sui

A thesis submitted in partial fulfilment of the requirements for the degree of Doctor of Philosophy

August 2025

CERTIFICATE OF ORIGINALITY

I hereby declare that this thesis is my own work and that, to the best of my knowledge and belief, it reproduces no material previously published or written, nor material that has been accepted for the award of any other degree or diploma, except where due acknowledgement has been made in the text.

_____________(Signed)

___Xin Sui___(Name of student)

To my family

ABSTRACT

Quality assurance (QA) is a critical component of pavement construction, ensuring the volumetric properties and surface conditions of paving materials, such as in-situ density, layer thickness, modulus, and smoothness. Traditional QA procedures rely on destructive core sampling and subsequent laboratory testing. This method is detrimental to pavement structures and only provides limited pavement information at discrete locations. Recently, advancements in multidisciplinary testing equipment and methods have led to the increasing adoption of non-destructive testing and evaluation (NDT&E) techniques, such as falling weight deflectometers (FWD), infrared thermography (IR), intelligent compaction (IC), nuclear/non-nuclear gauges, acoustic emissions (AE), lasers, and ground-penetrating radar (GPR). Among these, GPR has emerged as an attractive tool for measuring volumetric properties such as density, thickness, and moisture content (MC) due to its reasonable accuracy, rapid survey speed and extensive coverage.

GPR operates by transmitting and receiving electromagnetic (EM) waves to detect variations in the dielectric properties of pavement materials or defects. These dielectric properties, particularly the dielectric constant, can be estimated from GPR signals (A-scans) and correlated with volumetric properties. Despite its potential, GPR has yet to gain full acceptance as a reliable QA tool due to the concern on its reliability and noise interference.

The prediction errors of GPR can be caused by either suboptimal prediction models between dielectric properties and volumetric properties or from noise during GPR surveys. For example, material heterogeneity is frequently overlooked when estimating dielectric constants, resulting in inaccurate in-situ density predictions. Additionally, vibration effects caused by irregular antenna movements can distort the true reflection amplitude of GPR signals, making multi-layer thickness profiling challenging. Furthermore, the correlation between GPR attributes and

the moisture content (MC) of flexible pavements remains inadequately established, limiting the full potential of GPR for MC monitoring. On the other hand, while QA procedures using GPR for flexible pavements have been well-documented, the novel semi-flexible pavement (SFP), comprising porous asphalt (PA) skeletons filled with cement grouts, still lacks standardized QA protocols despite its growing adoption for its superior rutting resistance. This study aims to fill these gaps by enhancing GPR-based QA accuracy for flexible pavements and proposing a novel QA framework for SFP construction.

To improve GPR-based in-situ density predictions of flexible pavements, this study developed an enhanced model by introducing a random pore distribution coefficient into the Al-Qadi-Lahouar-Leng (ALL) density prediction model. This modification mitigates errors caused by the assumption of material homogeneity in the surface reflection (SR) method for dielectric constant estimation. Finite-difference time-domain (FDTD) simulations incorporating meso-scale pore characteristics were used to optimize the coefficient for open-graded PA, gap-graded stone mastic asphalt (SMA), and dense-graded asphalt concrete (AC) mixtures via non-linear curve fitting. Laboratory GPR tests on Superpave gyratory compaction (SGC) specimens demonstrated that the revised ALL model outperformed the conventional version, improving prediction accuracy by 6.7% for PA, 2.7% for SMA, and 1.9% for AC mixtures.

To address interference of noise from antenna vibrations during multi-layer thickness profiling, an antenna height shifting correction method was developed. Simulations revealed a third-order polynomial relationship between antenna height and GPR signal reflection amplitude. Based on this, a height-corrected surface reflection (HC-SR) method was proposed and validated through field GPR tests and laboratory measurements of field cores. The HC-SR method improved thickness prediction accuracy by 13.3%, 19.9%, and 17.4% for the first, second, and total asphalt layers, respectively, compared to the traditional SR method.

An automatic MC prediction model, the Leng-Sui (LS) model, was developed for wet asphalt mixtures. The model's coefficients were optimized using macro-to-meso-scale EM modelling and non-linear curve fitting. Laboratory tests on SGC specimens verified the LS model’s superior performance, achieving an average absolute MC prediction error of 0.2%, outperforming the conventional models, such as the MISO model (1.6%) and the Al-Qadi-Cao-Abufares (ACA) model (0.8%). This approach provides a practical, high-accuracy solution for continuous MC monitoring of asphalt pavements.

For SFP construction, this study introduced an automatic method to evaluate the grouting rate, quantified as the volumetric ratio of grout to air voids within the PA matrix. A novel dielectric constant prediction model, the Leng-Wang-Sui (LWS) model, was developed based on EM mixing theory for grouting rate estimation. Sensitivity analyses, numerical simulations of meso-scale GPR-SFP models, and laboratory tests validated the model, achieving an average relative estimation error below 7.0%. A practical QA workflow integrating GPR with the LWS model was proposed for on-site SFP grouting rate assessments.

Overall, this study aims to enhance GPR’s reliability during the QA procedure of flexible and semi-flexible pavement as a full replacement of traditional coring method. To achieve this, revisions were made upon existing models (e.g., ALL model and SR method) and novel models were established (e.g., LWS model and LS model). Deliverables of this study contribute to the field, and potential forward-looking implications on pavement QA events.

LIST OF PUBLICATIONS

Journal papers (Published)

Sui, X., Wang, S., Leng, Z.*, and Gong, M. (2025). In-situ density measurement using GPR considering random pore distribution of asphalt pavement. *Measurement*, *243*, 116479.

Sui, X., Leng, Z.*, Wang, S., Cai, X., Gong, M., and Zhang, L. (2024). In-situ grouting rate prediction of semi-flexible pavement based on a novel composite dielectric constant model and ground-penetrating radar. *Construction and Building Materials*, *438*, 137209.

Sui, X., Leng, Z.*, Wang, S., and Zhang, S. (2024). Removal of the GPR antenna vibration effect through height shifting correction for enhanced multi-layer asphalt pavement thickness determination. *Automation in Construction*, *161*, 105335.

Journal papers (Submitted to Journal)

Sui, X. Chen, Z. Leng, Z.*, and Wang, S. (2025). Moisture content quantification of asphalt pavement using GPR and macro-to-meso-scale electromagnetic modelling. *Computer-Aided Civil and Infrastructure Engineering*.

ACKNOWLEDGEMENTS

I would like to express my sincere gratitude to my supervisor, Prof. Zhen Leng, for his guidance, encouragement, and support during this research. His dedication, unselfishness and vision have inspired me in every step of my journey. I really appreciate his support not only in research, but also in shaping my personality, as he always told me: keep humble in life and keep rigorous in research. His words and deeds benefited me throughout the journey and will also guide me the direction in my future career.

I want to thank Dr. Siqi Wang, who is not only an excellent postdoctoral fellow but also a nice mentor in my PhD study. I still remember those days we dropped sweat on field surveys and enjoyed the beer afterwards. His invaluable guidance and suggestion convoyed the very beginning of my research and shorten my path to get familiar with GPR community.

I would like to acknowledge the technicians in our transport and highway engineering laboratories, Mr. M.C. Choi, Mr. W.K. Wong, and Mr. W.L. Wong, for their technical support in setting up equipment and daily companionship.

Special thanks had to be given to our research group members. In particular, I would like to express my sincere thanks to Dr. Bin Yang, Dr. Meizhao Han, Dr. Zhifei Tan, Dr. Ruijun Cao, Dr. Binbin Yin, Dr. Fuliao Zou, Dr. Xing Cai, Dr. Danning Li, Dr. Linyi Yao, Dr. Chuanqi Yan, Dr. Mingyang Gong, Dr. Haopeng Wang, Dr. Guoyang Lu, Dr. Yubo Sun, Dr. Xi Jiang, Dr. Zihang Weng, Dr. Dong Lu, Dr, Xinqiang Zhang, Dr. Gaoyang Li, Mr. Ruiqi Chen, Mr. Jiaqiu Xu, Ms. Jingting Lan, Mr. Shaowei Zhang, Mr. Kunpeng Zheng, Mr. Zijian He, Ms. Hanxi Li, Mr. Zhaojie Chen, Mr. Yulou Fan, Mr. Yijie Wang, … Sincerely appreciate your assistance and accompany during my PhD journey.

Finally, my highest gratitude goes to my dear wife, Zhuo, for her care, understanding, and unconditioned love. Same gratitude also goes to my father, my grandmother, my uncle and aunt, and my little sister. Without their endless love, I would not have accomplished this work.

LIST OF TABLES

LIST OF FIGURES

LIST OF ABBREVIATIONS

AC	Asphalt concrete
ACA	Al-Qadi-Cao-Abufares
AE	Acoustic emission
ALL	Al-Qadi-Lahouar-Leng
AV	Air void
DCP	Dynamic cone penetrometer
DMI	Distance measurement instrument
EM	Electromagnetic
EMD	Empirical model decomposition
FDTD	Finite-difference time-domain
FWD	Falling weight deflectometer
GPR	Ground-penetrating radar
GSSI	Geophysical Survey System, Inc.
HC-SR	Height correction surface reflection
HMA	Hot mix asphalt
IC	Intelligent compaction
IR	Infrared tomography
ISO	Influence and shape optimization
LS	Leng-Sui
LWD	Light weight deflectometer
LWS	Leng-Wang-Sui
MA	Mastic asphalt
MC	Moisture Content
MISO	Moisture influence and shape optimization
MSE	Mean square error
NCHRP	National Cooperative Highway Research Program
NDT & E	Non-Destructive Testing and Evaluation
NMAS	Nominal maximum aggregate size

PA	Porous asphalt
PML	Perfect matched layer
POM	Polyoxymethylene
QA	Quality assurance
QC/QA	Quality control & quality acceptance
RMSE	Root mean square error
Rx	Receiver
SASW	Spectral analysis of surface wave
SFP	Semi-flexible pavement
SGC	Superpave gyratory compactor
SMA	Stone mastic asphalt
SR	Surface reflection
SSD	Saturated surface dry
TOF	Time-of-flight
TWTT	Two-way travel time
Tx	Transmitter
VMD	Variational mode decomposition

TABLE OF CONTENTS

CHAPTER 1 INTRODUCTION

1.1 Background

Quality assurance (QA) plays a crucial role in pavement construction, encompassing a range of field and laboratory test to evaluate the physical and volumetric properties of asphalt mixtures. This program benefits both owners and contractors by enabling the monitoring of construction quality through the comparison of in-place data with design documents and specified standards. Traditional quality control and quality acceptance (QC/QA) programs rely on collecting data by drilling core samples from newly constructed pavements. While this method provides accurate, ground-truth data, it comes at the cost of damaging the pavement structure. Moreover, the limited number of the core samples often restricts the ability to gain a comprehensive understanding of the entire pavement section, leaving large areas unassessed.

Over recent decades, researchers and practitioners have increasingly explored the feasibility of incorporating non-destructive testing (NDT) methods into QA programs for flexible pavements. The National Cooperative Highway Research Program (NCHRP) launched a project titled "*NDT technology for quality assurance of HMA pavement construction*", which systematically evaluated various NDT methods for their applicability in the flexible pavement QC/QA procedures [1]. These methods included deflection-based technologies, dynamic cone penetrometer (DCP), ground penetrating radar (GPR), seismic pavement analyzer, geogauge, surface condition system, infrared tomography (IR), ultrasonic-based methods, as well as noise and friction methods. Among these, GPR has emerged as a particularly promising technique due to its ability to collect data at traffic speed, conduct non-invasive testing, and provide extensive spatial coverage.

GPR is a widely commercialized NDT tool, which has been successfully applied to various transportation infrastructures, including roads, bridges, tunnels, and airport runways for QA and concealed defects detection [2]. GPR operates by emitting electromagnetic (EM) waves through a transmitter toward the target. When these waves encounter materials or objects with different dielectric properties, they produce reflections and refractions, which are captured by a receiver to form the raw GPR signal, also known as an A-scan. From this signal, the dielectric constant (or relative permittivity) of the material can be estimated [3, 4]. According to EM mixing theory, the bulk dielectric constant of a porous medium is determined by the dielectric constant and volumetric fractions of each component [5]. This allows the dielectric constant to be linked to other volumetric properties of the material through correlation models, enabling GPR to measure key volumetric properties of pavements, particularly during QA programs. Recent applications of GPR in flexible pavement QA include thickness profiling, in-situ density prediction, and moisture content determination.

Despite being recognized as one of the most promising QA tools for flexible pavement construction, GPR's adoption as a full replacement for conventional coring methods remains limited due to challenges in estimation accuracy and success rates [6, 7]. Errors in GPR-based measurements typically arise from inaccuracies in dielectric constant estimation or the absence of robust correlation models. For instance, during continuous GPR surveys, antenna swaying and shifting caused by the tire-pavement interactions introduce vibration noise. This vibration effect camouflages the amplitude of the surface reflection and interface reflections. Thus, the dielectric constant estimation became inaccurate, complicating multi-layer thickness profiling in flexible pavements [8]. In the case of in-situ density prediction, existing correlation models are often undermined by the oversimplified dielectric constant estimation methods, which fail to account for material heterogeneity, leading to inaccuracies [9]. Similarly, for moisture content estimation, the lack of well-established correlation models hampers the ability to achieve higher prediction accuracy using GPR [10].

In addition to flexible pavement, a novel road type known as semi-flexible pavement (SFP) also lacks a robust QA procedure, which could be addressed using GPR. SFP consists of a porous asphalt (PA) skeleton (20% to 30% air void content) filled with cement grouts, offering improved rutting resistance compared with conventional flexible pavements [11, 12]. This innovative pavement type has been increasingly adopted in applications requiring high load-bearing capacities, such as bus terminals, airport runways, and urban arterial road subjected to channelized traffic flows. Research efforts have primarily focused on the design of grouting materials to ensure satisfactory fluidity, sufficient strength, and reduced curing time for early traffic reopening. However, QA program for SFP remains underexplored. One critical quality control parameter is grouting rate, which is defined as the degree of saturation of grouting material within the interconnected air voids of the PA matrix [13]. Currently, measurements of the grouting rate are limited to laboratory tests on manufactured specimens, and no effective method for in-situ field QA has been proposed. GPR presents a promising solution for profiling the grouting rate of SFP due to the dielectric constant contrast between bituminous and cementitious materials. However, a correlation model between the bulk dielectric constant and the grouting rate of SFP has yet to be developed.

1.2 Research Objectives and Scope

Building upon the knowledge gaps identified above, this research aims to significantly improve the accuracy of volumetric property estimation using GPR during the quality assurance processes of flexible pavement construction and propose a novel GPR-based method for estimating in-situ grouting rate in SFP construction QA programs. To achieve these objectives, the following research tasks were undertaken:

1. Literature review: A comprehensive review of the QA program of flexible pavement using NDT methods, sources of volumetric properties estimation error using GPR, as well as the composition of SFP and the measurement of in-situ grouting rate.

2. Development of an improved in-situ density prediction model using GPR, eliminating the inaccuracies caused by oversimplified assumption of the material heterogeneity during dielectric constant estimation procedure.

3. Development of a multi-layer asphalt pavement thickness profiling method using GPR, mitigating the vibration effect of irregular antenna shifting and swaying due to tire-pavement interactions.

4. Development of a novel MC prediction model based on EM mixing theory for flexible pavement.

5. Development of a novel SFP grouting rate estimation model based on EM mixing theory, along with a corresponding GPR-based QA procedure for SFP.

1.3 Significance of This Research

Upon completion of this research, the following contributions were achieved:

1. Achieve higher accuracy in the in-situ density prediction of flexible pavement using GPR.

2. Eliminates the vibration effects in multi-layer asphalt pavement thickness profiling using GPR.

3. Provides accurate estimation of MC in asphalt pavements using GPR.

4. Enables large-coverage, non-invasive measurement of the in-situ grouting rate for SFP using GPR, supported by a corresponding QA procedure.

1.4 Organization of This Thesis

This thesis is organized into seven chapters. Four key volumetric properties, namely in-situ density, thickness, moisture content, and grouting rate, are independently predicted using GPR. As a result, the content of these four chapters remains independent of each other, and no specific sequence is required. However, the development of the LS model for MC prediction relies on the derivation of the LWS model for grouting rate prediction. Consequently, the chapter on the LWS model for SFP grouting rate prediction precedes the chapter on the LS model for flexible pavement MC prediction. The detailed organization of the thesis is outlined as follows:

Chapter 1 introduces the background, objectives, scope, and significance of this research.

Chapter 2 presents a comprehensive literature review, covering the following topics:

(1) quality assurance of flexible pavement construction using NDT methods.

(2) working principle of GPR.

(3) GPR-based QA applications of flexible pavement construction.

(4) semi-flexible pavement.

Chapter 3 proposes a modified in-situ density prediction model of flexible pavement using GPR, incorporating meso-scale pore characteristics by introducing a random pore distribution coefficient into the ALL model. This modification addresses the previously overlooked dielectric constant variation along the depth in SR methods. The optimal coefficients for PA, SMA, and AC mixtures were determined through a non-linear curve fitting technique. The proposed model was validated via controlled laboratory tests on SGC specimens, conducted using a spacer-inserted antenna configuration.

Chapter 4 proposed a revised multi-layer asphalt pavement thickness prediction model using GPR, referred to as the HC-SR model. This model calculates the reflection amplitude of each asphalt layer through the antenna height–reflection amplitude relationship, rather than directly extracting values from GPR A-scan data. This approach removes the vibration effects caused by tire-pavement interaction. A third-order polynomial relationship between antenna height and reflection amplitude was revealed using FDTD simulations. The model's effectiveness was validated through field GPR surveys, including a bouncing test and continuous GPR measurements.

Chapter 5 develops a novel composite dielectric model, referred to as the LWS model, for predicting the grouting rate in SFP using the power-law EM mixing theory. Sensitivity analyses were performed to explore the effects of key model parameters, particularly the selection of power-law indices. The model's performance was validated using both simulation and laboratory test data. Additionally, a workflow for GPR-based grouting rate prediction in SFP was proposed.

Chapter 6 presents a novel internal MC prediction model, referred to as the LS model, based on the LWS model. The key power-law indices were optimized using a macro-to-meso-scale EM modelling approach. The model was validated through vacuuming tests and laboratory GPR measurements.

Chapter 7 concludes the thesis by summarizing the main findings and providing recommendations for future research.

The overall research framework is illustrated in Figure 1.1. The primary research content is organized into four key chapters:

(1) Development of an in-situ density prediction model using GPR with enhanced accuracy.

(2) Development of a multi-layer asphalt pavement thickness prediction model with improved precision.

(3) Development of an MC prediction model for internal pavement condition analysis.

(4) Development of a composite dielectric model for grouting rate prediction in SFP.

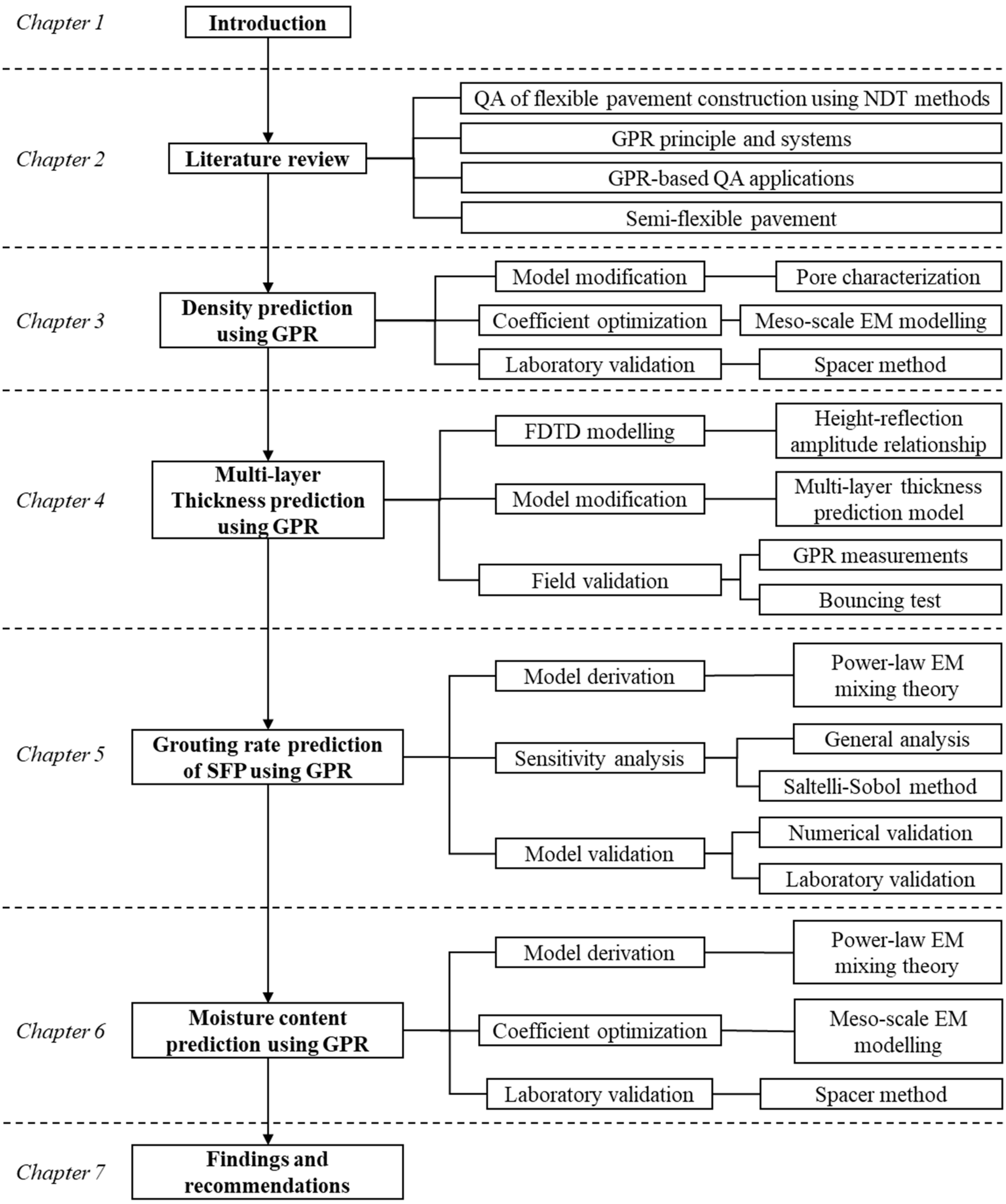

Figure 1.1 Research framework

CHAPTER 2 LITERATURE REVIEW

This chapter provides a comprehensive review of previous studies on asphalt pavement QA and corresponding GPR-based applications. Section 2.1 presents common QA programs during flexible pavement construction using NDT methods. Section 2.2 introduces GPR working principle and systems. Section 2.3 discusses the current research and applications of QA endeavours using GPR. Section 2.4 discusses the fundamentals of SFP.

2.1 QA programs of flexible pavement construction using NDT methods

Conducting QA program is crucial for flexible pavement construction, allowing the producers and contractors to have a close monitoring of the quality of the paved material properties before acceptance. This process encompasses sampling, testing, and assessing test results upon certain asphalt mixture and layer properties. According to a NCHRP project titled "*NDT technology for quality assurance of HMA pavement construction*", these properties can be grouped as volumetric, structural, and functional, serving for structural design, mixture design, and acceptance. Specifically, the volumetric properties include density, air void, moisture content, gradation, and voids in mineral aggregate; Structural properties include layer thickness and dynamic modulus; functional properties include surface profiles, noise and friction.

NDT methods are preferred for material or layer property measurement due to their non-destructive detection manner. According to their working principle, these NDT methods can be categorized into deflection-based methods, such as FWD and light weight deflectometer (LWD) [14, 15]; stress wave-based methods, such as impact echo, ultrasonic method, and the spectral analysis of surface wave (SASW) method [16-18]; electromagnetic (EM) wave-based methods, such as GPR, Nuclear/non-nuclear gauges, infrared tomography, and laser profiler [19-22]; as well as some other NDT technologies, such as intelligent compaction (IC) [23]. Specific material or layer property of the asphalt layer for flexible pavement construction are presented in Table 2.1, as well as suitable NDT methods. Among different types of NDT technologies, GPR has been more frequently applied for volumetric properties and layer thickness prediction.

Table 2.1 NDT technology for material or layer properties measurement of asphalt layer for flexible pavement construction [1]

Type of Property or Feature		NDT Technologies and Methods
Volumetric	Density	GPR Nuclear/Non-Nuclear Gauges
	Air Voids	GPR Infrared Tomography Acoustic Emissions Intelligent Compaction
	Moisture Content	GPR
	Gradation	GPR Infrared Tomography Road Surface ANalyzer
	Voids in Mineral Aggregate	GPR
Structural	Thickness	GPR Ultrasonic Magnetic Tomography
	Dynamic Modulus	Ultrasonic Deflection-based: FWD, LWD Roller-Mounted Response Systems
Functional	Profile: IRI	Profilometer, Inertial Profilers
	Noise	Noise Trailers
	Friction	Circular Texture Meter Road Surface ANalyzer

2.2 GPR principle and systems

2.2.1 EM theories

GPR works by transmitting and receiving EM waves, whose propagation in continuous medium is governed by a set of Maxwell's equations [24, 25], including Gauss' law (2-1), Gauss' law for magnetism (2-2), Faraday's induction law (2-3), and Maxwell-Ampere's law (2-4):

$$\nabla \vec{E} = \frac{\rho}{\varepsilon} \quad (2-1)$$

$$\nabla \vec{H} = 0 \quad (2-2)$$

$$\nabla \times \vec{H} = -\mu \frac{\partial \vec{H}}{\partial t} \quad (2-3)$$

$$\nabla \times \vec{E} = \vec{J} + \frac{\partial \vec{E}}{\partial t} \qquad (2-4)$$

where $\vec{E}$ is electric field intensity (Volts/meter); $\vec{H}$ is magnetic field intensity (Amps/meter); $\vec{J}$ is the electric current density (Amperes/meter^2); ρ is the electric charge density (coulombs/meter^2); ε is the permittivity (Farads/meter), and μ is permeability of free space (Henrys/meter). In GPR's applications of pavement, the target is usually in the far field of the antennas [4, 19, 26]. In this case, the EM waves can be assumed to be plane wave, whose propagation velocity v in a lossless medium can be calculated as:

$$v = \frac{1}{\sqrt{\mu\varepsilon}} \qquad (2-5)$$

2.2.2 GPR systems

Various GPR systems are commercially employed for a range of pavement detection tasks. The selection of an appropriate GPR system requires a careful balance between the target's burial depth and the desired resolution. At present, ground-coupled 2D and 3D radar systems are more commonly utilized for subgrade distress inspections due to their superior detection depth. In contrast, for predicting material properties of asphalt layers, air-coupled horon antennas with higher central frequencies are more preferred, as they offer enhanced lateral and depth resolution. An air-coupled GPR system typically consists of a control unit, antenna, power supply, distance measurement instrument (DMI), and GPS. The control unit is responsible for generating the incident electrical signal for the antenna, as well as managing and storing GPR operations and data. The antennas function as both transmitters and receivers, converting electrical signals into electromagnetic waves and vice versa. Meanwhile, the DMI and GPS can provide precise location information for each GPR scan. Depending on the application, the GPR system can either be mounted on a vehicle for high-speed traffic surveys or carried by a cart for localized measurements.

In this study, two primary GPR systems were employed. For the field tests, a cart-mounted air-coupled horn antenna with a central frequency of 2 GHz, manufactured by Geophysical Survey Systems, Inc. (GSSI), was utilized [27]. Figure 2.1 illustrates the setup, including a 2 GHz horn antenna and a SIR30 control unite, both custom-mounted on a UtilityScan Pro cart. For the laboratory tests, a GSSI 2GHz palm radar, integrated with a SIR4000 control unit, was used, as shown in Figure 2.2 [27].

Figure 2.1 GSSI 2GHz air-coupled horn antenna for field surveys

Figure 2.2 GSSI 2GHz palm antenna for laboratory tests

2.3 GPR-based QA applications

2.3.1 In-situ density prediction

Flexible pavement QA program requires accurate measurement of in-situ density during construction, as a critical parameter reflecting compaction degree [28]. Both under- and over-compaction hinder the mixture obtaining design air void (AV) content. The former (AV lower than 3%) leads to distress, such as rutting, shoving, and bleeding. The latter (AV higher than

8%) results in moisture-indued damage, as well as ravelling and cracking [29, 30]. In this study density and AV were used interchangeably. Recently, GPR has been widely used for in-situ density prediction for flexible pavement. The first step is determining the dielectric constant of asphalt mixture from GPR A-scan data, which can be estimated using two methods, including the time-of-flight (TOF) method and surface SR method. The TOF method calculates the dielectric constant using two-way travel time (TWTT) and the layer thickness [31]:

$$\varepsilon = \left(\frac{ct}{2d}\right)^2 \qquad (2-6)$$

where *c* is the speed of light (3×10^8m/s); *t* is the TWTT of EM wave in the layer, as illustrated in Figure 2.3, and *d* is the layer thickness.

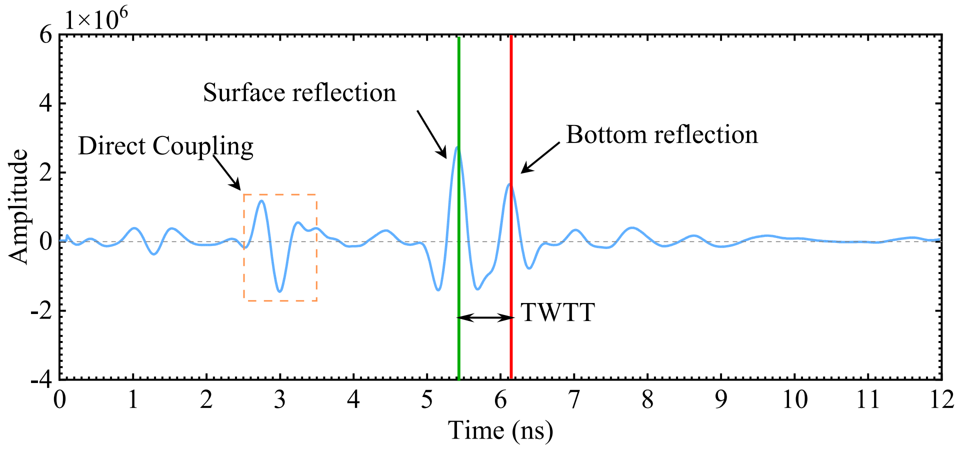

Figure 2.3 Determination of TWTT and reflection amplitude from GPR A-scan

The TOF method provides the bulk dielectric constant of the asphalt mixture and takes the material heterogeneity into account. However, this method requires a known layer thickness profile, which can hardly achieve in real-world applications. Therefore, the dielectric constant is more practically estimated using SR method [32, 33]:

$$\varepsilon = \left(\frac{1+\frac{A_0}{A_{inc}}}{1-\frac{A_0}{A_{inc}}}\right)^2 \qquad (2-7)$$

where A_0 is the surface reflection amplitude of the AC layer, and A_{inc} is the incident signal amplitude, which can be measured by placing a metal plate on the AC surface. This method does not require layer thickness information. However, it only estimates the dielectric constant of skin depth, overlooking the material heterogeneity along depth [9].

The dielectric constant can be then mapping to the in-situ density, referred to as the density prediction model. Existing density prediction models can be categorized as regression and EM mixing theory models. Regression models establish the correlations using lab tests of fabricated or field core specimens. The model coefficients can be determined after conducting GPR measurements and laboratory density measurements [34, 35]. However, the prediction accuracy depends on extensive amounts of specimens for calibration, which requires recalibration of model coefficients for different asphalt mixtures across projects. In contrast, EM mixing theory-based models incorporate the volumetric properties of asphalt mix components to predict the bulk dielectric constant of the mixture [9]. This approach only requires limited sample cores for calibration and provides accurate density predictions across multiple projects. The ALL model, derived from the modified Bottcher EM mixing model, has been developed and well accepted for in-situ density profiling for field applications [9, 36]:

$$G_{mb} = \frac{\frac{\varepsilon_{AC}-\varepsilon_b}{3\varepsilon_{AC}-2.3\varepsilon_b} - \frac{1-\varepsilon_b}{1+2\varepsilon_{AC}-2.3\varepsilon_b}}{\left(\frac{\varepsilon_s-\varepsilon_b}{\varepsilon_s+2\varepsilon_{AC}-2.3\varepsilon_b}\right)\left(\frac{1-P_b}{G_s}\right) - \left(\frac{1-\varepsilon_b}{1+2\varepsilon_{AC}-2.3\varepsilon_b}\right)\left(\frac{1}{G_{mm}}\right)} \quad (2-8)$$

where ε_{AC}, ε_b, and ε_s is the dielectric constant of the asphalt mixture, asphalt binder, and the aggregate, respectively; G_s is the specific gravity of aggregate; G_{mb} and G_{mm} is the bulk and theoretical maximum specific gravity of mixture, respectively, and P_b is the binder content.

Reported inaccurate in-situ density prediction using ALL model occurred in different projects, ranging from 1% to 13.4% [37]. The inaccuracies arise primarily from the dielectric constant estimation of asphalt mixture using SR method, which simplifies the representation of the thick porous medium to its surface reflection amplitude of skin depth (close to the surface of asphalt structural layer), potentially overlooking the material heterogeneity of the actual asphalt mixture along depth. Xiong et al. proposed an influence and shape optimization (ISO) model based on the ALL model [38]. This model optimizes the shape factor in the ALL model from a purely statistical perspective, while the inherent limitation of the SR method has not been considered. Moreover, while the ALL model performs well with dense-graded asphalt mixtures, such as AC, its accuracy diminishes with PA mixtures. It is yet to be determined for SMA mixtures.

2.3.2 Thickness profiling

Determining the thickness of asphalt pavement plays a critical role in QC/QA of newly constructed flexible pavement, as well as in routine condition assessments of in-service pavement [39, 40]. GPR has been widely utilized to replacing drilling methods to fulfil thickness profiling of the asphalt layer using Equation (2-6) [41, 42]. The dielectric constant of the mixture is usually estimated using SR method. Except the inherent estimation error of the SR method, other factors that influence the prediction accuracy includes system instability, environmental noises, and vibrations caused by the tire-pavement interaction during field surveys. Recent advancements in GPR equipment have addressed signal instability through circuit/hardware modifications [19]. Environmental noise can be minimized by utilizing filters, such as bandpass filtering and adaptive filtering [43, 44]. However, vibrations caused by tire-pavement interaction, especially in vehicle- or van-mounted GPR systems where antennas are typically attached to wooden or metal supporting frames at the front or rear of the vehicle, present a significant source of error. These vibrations introduce irregular fluctuations that obscure the target reflections. Recent studies have explored methods, such as wavelet transform, empirical mode decomposition (EMD), and variational mode decomposition (VMD), as well as their variants to address this issue [45-47]. However, these methods primarily focus on statistically smoothing the signal rather than correcting the effects of vibrations on reflection amplitude values. Reported errors in asphalt layer thickness estimation by different researchers at the project or network level have ranged from 2.9% [6] to 7.5% [48], and 5-10% [7].

The vibrations resulting from vehicle tire-pavement interaction during air-coupled GPR survey can generally be divided into two categories: high-frequency micro-scale vibrations caused by pavement surface roughness and the low-frequency macro-scale vibration caused by antenna swaying or shifting. The macro-scale vibration is typically induced by poor surface conditions of in-service pavements and horizontal joint areas left by regular maintenance work using sealants in newly built highways. Both scales of vibrations affect the antenna-pavement height and consequently the total reflected EM energy from the pavement structure. Correspondingly, the amplitude, which is highly determined by the emitted EM energy, will fluctuate away from its original value. In essence, irregular shifts in antenna height are the origin of all vibration effects. Models that correlate surface reflection amplitude to antenna height (or converted to the time delay in free space) have been developed, including the inverse model [49], power model [8], and exponential model [50].

2.3.3 Moisture content prediction

Moisture infiltration is a key factor contributing to the time-progressive deterioration of asphalt pavements. Moisture trapped within connected air voids or unexcepted microcracks undermines the cohesive bond between asphalt binder and aggregates under repeated traffic loadings. During the service life, asphalt pavement may experience unsaturated or saturated conditions, accelerating moisture-induced damage, such as stripping, potholes, and ravelling [51, 52]. Monitoring the MC within the surface asphalt layer is crucial for timely maintenance and effective rehabilitation of asphalt pavements. In-situ MC quantification, however, poses significant challenges in field applications. While drilling core samples is a reliable method for QC/QA, providing insights into layer thickness, density, and modulus [20, 53], it is rarely employed for MC quantification due to the involvement of cooling water during core extraction. Embedded sensors or probes are commonly used in loose porous materials such as soils and sand but are impractical for asphalt pavements due to the higher stiffness. Additionally, the excavation required for sensor placement can compromise pavement structural integrity, creating weak region susceptible to further moisture infiltration.

Since the dielectric constant of water (approximately 81) is significantly higher than that of typical pavement materials (approximately 4–8), GPR demonstrates strong sensitivity to moisture, making it an efficient NDT technique for MC quantification [54, 55]. Despite its potential, GPR-based MC monitoring faces challenges due to the lack of well-established correlations between MC and GPR attributes, limiting its application at project or network scales. Earlier studies, such as Topp et al.'s regression models for soil MC prediction, laid the groundwork for such correlations [56]. For asphalt mixtures, Cao et al. proposed a regression model based on the normalized ratio of the dielectric constants of wet and dry asphalt mixtures [57]. However, these regression models often fail to generalize across projects due to variations in material composition. Alternatively, models based on EM mixing theory predict the bulk dielectric constant of porous media by considering the dielectric properties and volumetric fractions of individual components. For instance, Abufares et al. developed an ACA model using modified Bottcher mixing theory to estimate MC in cold in-place recycled asphalt [58]:

$$MC = \frac{-\left(\left(G_{mb}(C+D-B)\right)^2 - 4DG_{mb}\left(A+G_{mb}(C-B)\right)\right)^{\frac{1}{2}} + G_{mb}(B-C-D)}{2DG_{mb}} \quad (2-9)$$

$$A = \frac{\varepsilon_{WAC} - \varepsilon_b}{3\varepsilon_{WAC} - 2.3\varepsilon_b} - \frac{1-\varepsilon_b}{1+2\varepsilon_{WAC} - 2.3\varepsilon_b} \quad (2-10)$$

$$B = \frac{\varepsilon_s - \varepsilon_b}{\varepsilon_s - 2.3\varepsilon_b + 2\varepsilon_{WAC}}\left(\frac{1-P_b}{Gse}\right) \quad (2-11)$$

$$C = \frac{1-\varepsilon_b}{1-2.3\varepsilon_b + 2\varepsilon_{WAC}}\left(\frac{1}{Gmm}\right) \quad (2-12)$$

$$D = \frac{1-\varepsilon_b}{1-2.3\varepsilon_b + 2\varepsilon_{WAC}} - \frac{81-\varepsilon_b}{81-2.3\varepsilon_b + 2\varepsilon_{WAC}} \quad (2-13)$$

where ε_{WAC} is the dielectric constant of wet asphalt concrete. MC predicted using ACA model is basically one of the two roots to a quadratic equation, leaving the formular complex. Xiong et al. proposed a MISO model that incorporates a shape factor optimized through non-linear curve fitting [38]:

$$MC = \frac{1}{G_{mb}\left(\frac{81-\varepsilon_b}{81+A} - \frac{1-\varepsilon_b}{1+A}\right)} \times \left(\frac{\varepsilon_{WAC} - \varepsilon_b}{\varepsilon_{WAC} + A} - \left(1 - \frac{G_{mb}}{G_{mm}}\right)\frac{1-\varepsilon_b}{1+A} - \frac{G_{mb}(1-P_b)}{G_{se}}\frac{\varepsilon_s - \varepsilon_b}{\varepsilon_s + A}\right) \quad (2-14)$$

$$A = \mu\varepsilon_b + \nu(\varepsilon_{WAC} - \varepsilon_b) \quad (2-15)$$

where μ and ν are 5.1 and -4.5, respectively. Although EM mixing theory-based models offer broader applicability than regression models, their limited prediction accuracy and reliance on sparse ground-truth or laboratory data hinder their reliability and generalizability.

2.4 Semi-Flexible Pavement

SFP consists of a PA matrix with a high air void content ranging from 20% to 35% filled with grouting materials, such as pure cement paste and cement mortar [59, 60]. The hybrid nature of SFP, integrating the beneficial features of both flexible and rigid pavements, has catalysed its growing interest in pavement construction. This innovative pavement form is increasingly adopted for applications demanding high load-bearing capacities, including bus terminals, airport runways, and urban arterial roads subject to channelized traffic flows [61, 62]. The distinctive secondary skeleton structure of SFP imparts superior rutting resistance while maintaining enough load-bearing capabilities [63]. The mechanical behaviour of SFP has been evaluated and studied through both lab tests and field validations, demonstrating its suitability for pavement systems [64-66]. However, it is acknowledged that its performance is significantly influenced by the construction quality [67].

SFP construction entails a sequential two-phase process: the paving of the PA matrix followed by the infusion of the cementitious grouts [68]. A specific curing interval, contingent upon the particular grout composition, is requisite post-construction to facilitate the attainment of the necessary material strength, after which the pavement can be opened to traffic [69]. The water-to-cement ratio of the cement grouts is a pivotal determinant, necessitating careful design and adjustment to ensure the attainment of optimal compressive and flexural strengths, as well as satisfactory workability. Poor grout fluidity may lead to air voids within the PA matrix remaining unfilled [70], which, as research indicates, can initiate the formation of micro-cracks under traffic loading, potentially progressing to macro-cracks [71]. Mechanical test outcomes have unveiled that insufficient grouting markedly impairs the functional and performance attributes of SFP, thereby reducing its longevity and service life. Current literature suggests that a remaining air void content between 3% and 6% is optimal for maintaining the structural integrity and durability of SFP in service [72, 73].

For the purpose of assessing the grouting adequacy within SFP, the grouting rate represents a critical metric indicative of the residual air void content. This rate is quantified as the volumetric ratio of grouting material to the air void volume within the PA matrix [74]. Accurate profiling of the SFP's in-situ grouting rate contributes to localized milling and excavation of newly built section with low mechanical strength. Real-time monitoring of in-situ grouting rate also led to timely adjustment of the grouting formula during the following construction activities. Traditional determination of the grouting rate has been through laboratory mass measurements of the grouted material [75]. However, this approach is impractical for large-scale, in-situ evaluations due to the invasive nature and limited spatial assessment capabilities of drilling field cores. Consequently, the necessity for a non-destructive, accurate grouting rate assessment technique is evident. It is applicable to build a dielectric model for SFP based on the general power-law model by selecting the right power indexes. Given the higher dielectric constant of cement grouts (ranging from 6 to 10) relative to PA matrix components (with aggregate at 3-5, asphalt binder at 2-4, and air at 1) [62], it is feasible to utilize the dielectric constant as a surrogate measure for the grouted volume fraction [63].

2.5 Summary

GPR demonstrates significant potential in the QA processes for flexible and semi-flexible pavements, particularly in the characterization of volumetric properties. However, its application as a reliable alternative to traditional drilling methods remains constrained by several limitations, including the challenges of accurately predicting dielectric constants, susceptibility to vibration interference, and the need for more robust attribute prediction models. Through a comprehensive literature review, the current research efforts and advancements in GPR-based QA methods for flexible pavements were analyzed. The findings from these studies serve as a foundation and inspiration for this dissertation. The key insights from the literature review are summarized as follows:

(1) To address inaccuracies in the SR method when estimating dielectric constants, a refinement parameter that accounts for the spatial distribution variations of particles within asphalt mixtures is recommended. This refinement ideally involves comparing actual air void content measurements from in-situ core samples with predictions from the ALL model. However, the difficulty of obtaining large amounts of in-situ data poses a challenge. To overcome this, computer-aided methods could simulate field conditions, incorporating material heterogeneity, specific gradation characteristics, and unique spatial particle distributions. Such simulations would augment the dataset, enabling a more representative and robust revision of the ALL model.

(2) The influence of antenna height variation on pavement thickness measurements has not been thoroughly investigated. Existing models only describe the relationship between antenna height and surface reflection amplitude, which limits their capability to estimate the bulk dielectric constant of the asphalt layer. This approach is inadequate for predicting the thickness of multi-asphalt-layer pavements. Furthermore, these models have not been validated through continuous GPR surveys, and a comprehensive correction method that improves the accuracy of multi-layer thickness profiling under varying antenna heights is currently lacking.

(3) Predicting MC using GPR remains a challenge due to the absence of a highly accurate MC prediction model. The development of such a model could benefit from computer-aided technologies, which would allow for improved accuracy and validation across major flexible pavement mixture types. Rigorous validation protocols should also be implemented to ensure reliability.

(4) The use of dielectric constants for estimating SFP grouting rates faces numerous challenges. The electrical properties specific to SFP composites are not yet fully understood, and no theoretical model currently exists to accurately predict the

dielectric constant of SFP materials. While a positive correlation between grouting rate and bulk dielectric constant has been identified, the quantitative relationship between these variables remains undefined. Additionally, a standardized workflow for onsite grouting rate assessment using GPR-derived dielectric constant measurements is still absent. Addressing these gaps is essential before this method can be considered a viable alternative to conventional coring approaches.

The research gaps identified from the literature review are as follows:

(1) The ALL model requires refinement to eliminate inaccuracies in dielectric constant estimation using the SR method by incorporating material heterogeneity.

(2) The impact of antenna vibrations on multi-asphalt-layer thickness profiling using GPR must be addressed.

(3) A novel MC prediction model should be developed to account for different types of asphalt mixtures.

(4) A new grouting rate prediction model for SFP is required, along with a corresponding QA procedure using GPR.

Therefore, the following works were conducted with the expectation of minimizing those research gaps.

CHAPTER 3 IN-SITU DENSITY MEASUREMENT USING GPR CONSIDERING RANDOM PORE DISTRIBUTION OF ASPHALT PAVEMENT

This chapter aims to achieve accurate measurement of asphalt pavement in-situ density using GPR. To fulfil this, an advanced EM mixing-based density prediction model that improves accuracy by considering the random pore distribution of materials was proposed. ALL model's applicability to PA, and SMA mixtures is also revealed. FDTD simulations were utilized, incorporating meso-scale electromagnetic models established through a random aggregate generation technique. A random pore distribution coefficient was proposed to mitigate the estimation errors inherent in the SR method assumption. The influence of antenna height and air void content on the accuracy of the refined model was examined. Optimal random pore distribution coefficients for different asphalt mixtures were determined by minimizing the sum of squared errors between the bulk specific gravity of the asphalt mixture predicted using the ALL model and the proposed model through non-linear curve fitting. Controlled laboratory experiments on SGC specimens were performed for validation purposes. A specialized spacer method was used for GPR measurements on SGC samples, eliminating the edge diffraction effect. The outcomes of this research could significantly enhance the precision of in-situ density estimations for asphalt pavements using GPR.

3.1 Random Pore Distribution Coefficient Considering Material Heterogeneity

According to Bottcher mixing model, the dielectric constant of asphalt mixture is composed of asphalt binder as the background material with inclusions of spherical-shaped coarse aggregate, and air particles [76, 77]. A modified form of Bottcher model was proposed by Behari (2005) by introducing a shape factor μ to represent the shape of the inclusions as arbitrary [78]. Leng (2011) suggested an optimum shape factor of -0.3 that could be generally applied to different asphalt mixes [37]. This value was obtained by examining the in-situ density prediction error of five mixes using GPR and in-situ cores. By examining the composition and volumetric parameters of asphalt mixture, as presented in Figure 3.1, The bulk specific gravity of asphalt mixture, G_{mb}, can be obtained with the measured bulk dielectric constant of the asphalt mixture ε_{AC} using ALL model. Among all parameters, ε_s, and ε_b can be determined empirically. ε_s is usually within the range of 6 to 8, and 4 to 7 for limestone and granite, respectively. ε_b is usually constant at around 3.0; P_b, G_s, G_b, and G_{mm} can be obtained from the mix design. ε_{AC} can be estimated using SR method.

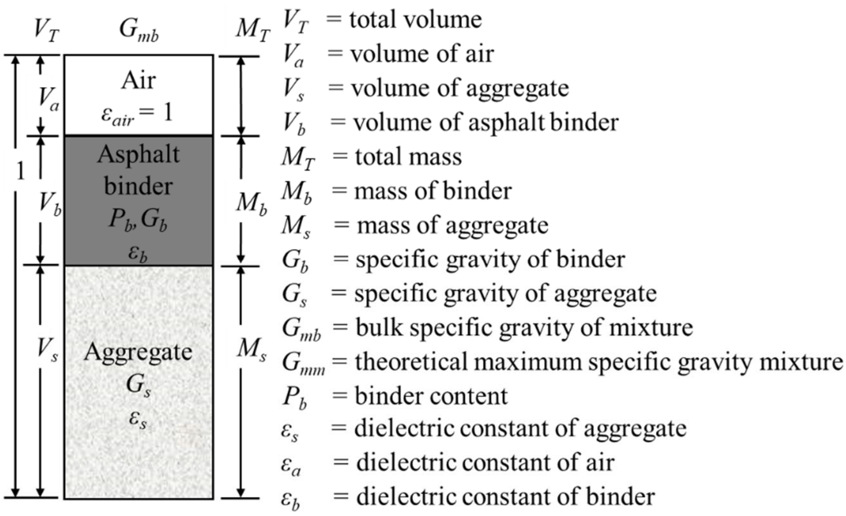

Figure 3.1 Asphalt mixture composition and parameters

Sensitivity analysis of the ALL Model revealed that the estimated error of the asphalt mixture dielectric constant results in a comparable estimated error of the bulk specific gravity [37]. For example, an ε_{AC} estimation error of 10% gives a G_{mb} error of 8.8% [37]. In this study, the SR method was modified by introducing a random pore distribution coefficient γ to consider the meso-scale material heterogeneity characteristics:

$$\varepsilon_{AC}^{*} = \gamma\varepsilon_{AC} = \gamma\left(\frac{1+\frac{A_0}{A_p}}{1-\frac{A_0}{A_p}}\right)^2 \qquad (3-1)$$

A modified ALL model was obtained by substituting Equation (3-1) into Equation (2-8) and rearranging:

$$G_{mb} = \frac{\frac{\gamma\varepsilon_{AC}-\varepsilon_b}{3\gamma\varepsilon_{AC}-2.3\varepsilon_b} - \frac{1-\varepsilon_b}{1+2\gamma\varepsilon_{AC}-2.3\varepsilon_b}}{\left(\frac{\varepsilon_s-\varepsilon_b}{\varepsilon_s+2\gamma\varepsilon_{AC}-2.3\varepsilon_b}\right)\left(\frac{1-P_b}{G_s}\right) - \left(\frac{1-\varepsilon_b}{1+2\gamma\varepsilon_{AC}-2.3\varepsilon_b}\right)\left(\frac{1}{G_{mm}}\right)} \quad (3-2)$$

Affecting factors of the value of γ include meso-scale asphalt mixture characteristics, such as mix type, nominal maximum aggregate sizes, random pore distribution and air void ratio. GPR antenna configuration parameters, such as antenna surface height, will also affect the radiation pattern of short EM pulse. A comprehensive exploration of these factors on γ will be implemented in the next section.

3.2 Optimization of Random Pore Distribution Coefficient Using Meso-Scale EM Modelling

3.2.1 Meso-Scale EM Models

The purpose of this section is to find the optimal random pore distribution coefficient γ in the proposed model and explore factors that affect model performance through computer-aided approaches. Numerical simulations of the GPR-asphalt pavement system were performed. GprMax 2D, an open-source Python written software capable of conducting FDTD simulations was utilized [79]. Asphalt pavement structures with meso-scale characteristics and the corresponding GPR antenna configuration were illustrated in Figure 3.2.

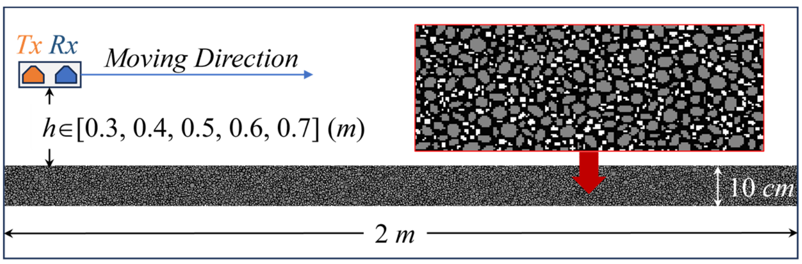

Figure 3.2 Asphalt pavement geometry and GPR antenna configuration setting

A 2 m-long, 10 cm-thick asphalt pavement structure was selected. The models were established using a random aggregate generation technique [80-82], which contains four subsequent steps:

1. Calculate the total number of aggregates in each sieve size based on the model geometry and mix information.
2. Randomly generate and place the coarse aggregate (≥2.36 mm) within the designed zone, followed by a check procedure to avoid particle overlaps.
3. Randomly generate and place air void in unoccupied space.
4. Define the left region as asphalt mortar containing asphalt binder and fine aggregate (<2.36mm).

Eleven mix designs were collected from previous literature, covering commonly used asphalt mixture types in practices, including AC, PA, and SMA [83-89]. The gradation of each mix type was listed in Table 3.1, categorized by mix type and the nominal maximum aggregate size (NMAS). Five air void contents were considered for each mix to examine the effect of air void contents on the proposed random pore distribution coefficient. Five antenna-surface heights were considered to unveil the effect of the distance between the antenna and the pavement surface. Three parallel structures were generated for each mix to eliminate the statistical and system error. In total, 825 (11×5×5×3) models were built for model parameter fine-tuning purpose. The detailed arrangement of model settings is illustrated in Figure 3.3. The dielectric constant of asphalt binder and aggregate was set to 3 and 6, respectively, according to previous literature [37].

Table 3.1 Gradation of selected mixes [83-89]

	Passing Percent (%)										
	PA			SMA				AC			
Sieve Size (mm)	10	13	16	10	13	16	20	10	13	16	20
28	-	-	-	-	-	-	100	-	-	-	100
20	-	-	100	-	-	100	97.5	-	-	100	98
16	-	100	95	-	100	93.4	97.5	-	100	95	98
14	100	91.6	80	100	95.5	79.9	82.5	100	97.5	82.5	85
10	96	61.5	58	96	64.5	54.8	82.5	96	97.5	70	75
5	21	18.9	20	32	27	23.9	35	73	62.5	46	61
2.36	11	16.4	16	23	21.7	22.8	27.5	52	42.5	32	44
0.075	2.5	5.7	3.2	12.2	9.7	8.9	10.5	7.5	6	4	5.5
Binder content (%)	5.5	4.7	5.0	6.1	5.7	6.1	5.3	6.0	5.6	4.4	5.0

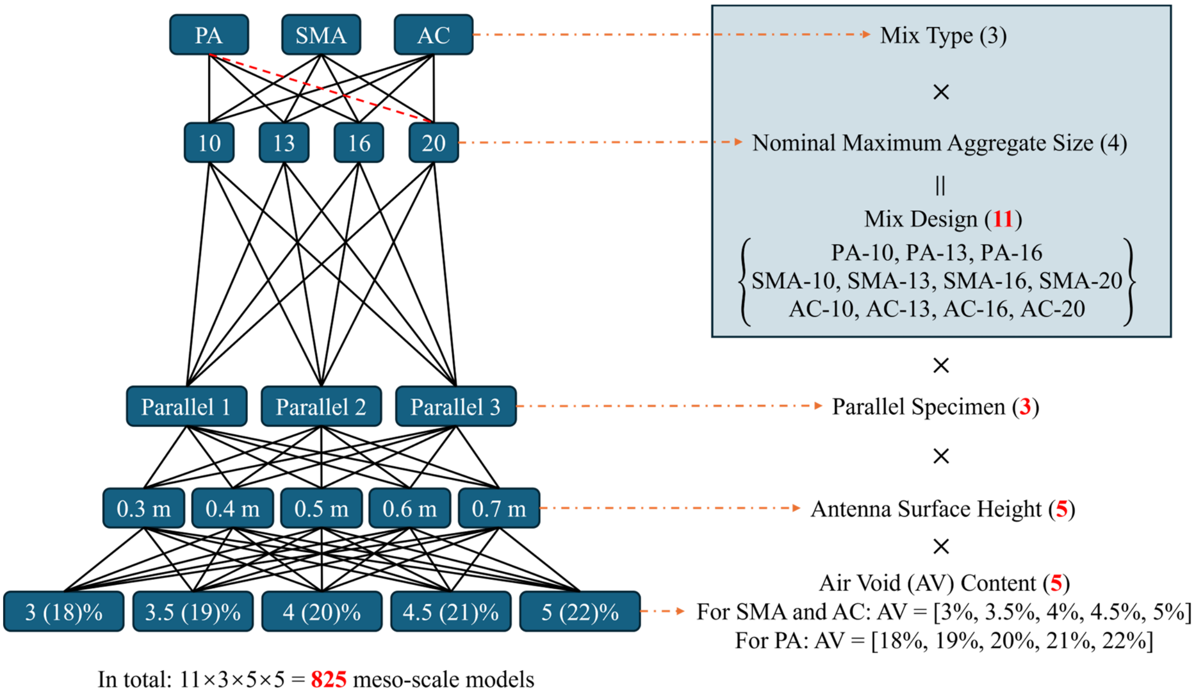

Figure 3.3 Arrangement of meso-scale FDTD models of asphalt pavement

A decoupling process was applied to the raw GPR data to isolate the camouflaged target pavement signal from the antenna direct coupling signal, as depicted in Figure 3.4. The adopted decoupling process enabled the clear distinction of reflections generated from both the surface and bottom interfaces of the asphalt pavement structural layer. The characteristic waveform ripples, commonly observed in field GPR B-scan profiles but typically absent in the numerical datasets, were successfully simulated. This achievement underscores the efficacy of the employed meso-scale EM modelling approach, demonstrating its potential to accurately mimic the real-world subsurface conditions of the pavement structures. This superiority can also be visualized by examining the GPR A-scans of homogeneous and heterogeneity models, as shown in Figure 3.5. Compared with the field test data, the used heterogeneous model realizes the same ripple pattern with the field survey data. Meanwhile, the surface reflection from both the simulation dataset and the field dataset can be distinguishable identified, leaving no error generated during the following optimization process.

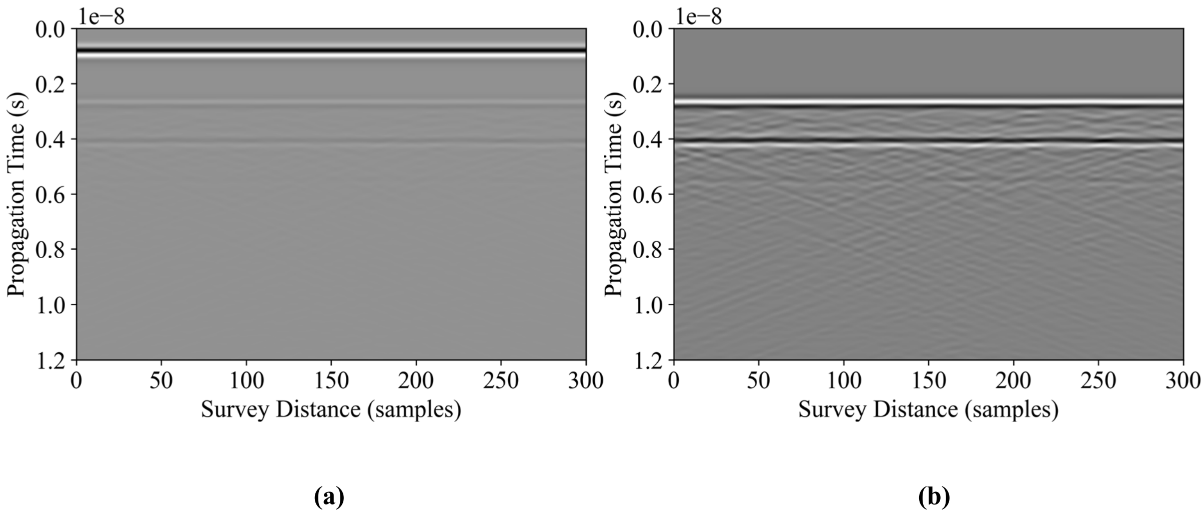

Figure 3.4 GPR B-scan radargram of the meso-scale asphalt mixture model and the decoupling process: (a) raw B-scan radargram; (b) decoupled GPR B-scan radargram

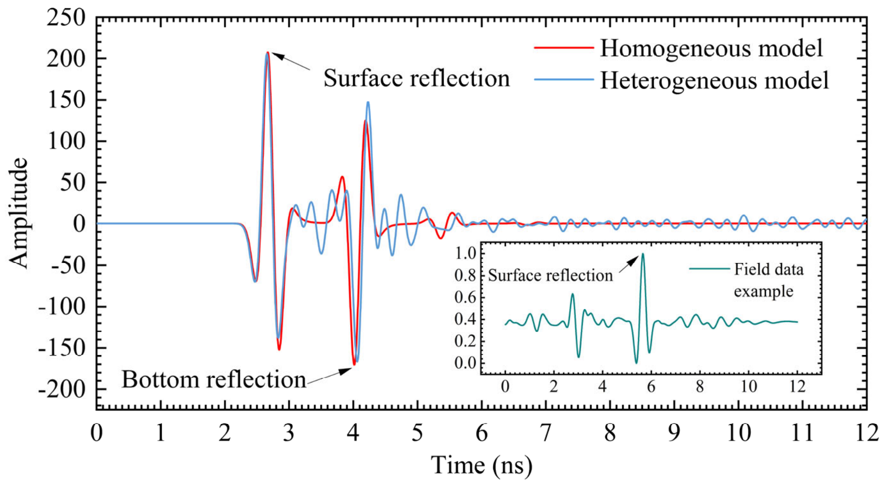

Figure 3.5 GPR A-scan signal of the pavement model with/without considering the material heterogeneity in EM modelling

3.2.2 Simulation Results and Discussion

Figure 3.6 displays the simulation outcomes for a PA-10 asphalt mixture possessing an air void content of 18% and an antenna-surface height of 0.3 meters as an example. Analysis of Figure 3.6 (a) reveals that the dielectric constant profile estimated via the SR method exhibits significant fluctuations compared to the benchmark values. This may be caused by the non-uniform distribution of aggregates within the skin depth of the asphalt pavement surface. Results in Figure 3.6 (b) illustrates that the inaccuracies in the dielectric constant could directly translate into erroneous G_{mb} predictions using the ALL model. The ALL model is sensitive to the dielectric constant of the asphalt mixture as an input parameter. Hence, any fluctuation in the dielectric property estimations can affect the G_{mb} results significantly. The observed deviation underscores the necessity for refined modelling approaches. It can effectively integrate the complex, material vertical heterogeneity nature of asphalt mixtures to improve the precision of in-situ G_{mb} estimations.

To find the optimal random pore distribution coefficient for each case, non-linear least square curve fitting was executed using Equation (3-3). The optimal random pore distribution coefficient γ was ascertained through the minimization of the root mean square error (RMSE) between G_{mb} derived from the refined SR method and those determined by the TOF method:

$$\gamma_{opt} = \underset{\gamma}{argmin} \sqrt{\frac{1}{N}\sum_{i=1}^{N}\left(G_{bm,SR}^{corrected}(i,\gamma) - G_{mb,TOF}(i)\right)^2} \qquad (3-3)$$

where $G_{bm,SR}^{corrected}(i,\gamma)$ is the G_{mb} estimated using SR method after considering the random pore distribution coefficient; $G_{mb,TOF}(i)$ is the G_{mb} estimated using TOF method; and N is the number of samples for each case, which equals to 300. The optimal random pore distribution coefficient γ is thus the value that yields the lowest RMSE, signifying the highest correspondence between the two methods across the dataset of N measurements. The layer thickness is a predefined and known input during simulations. This enables the computation of the benchmark value for the dielectric constant using TOF method, which in turn facilitates the refinement of the random pore distribution coefficient.

The optimal random pore distribution coefficient for PA-10 asphalt mixture with an air void content of 18% and an antenna-surface height of 0.3 meters is listed in Figure 3.6 (b) as an example. The figure also displays the modified G_{mb} profile, achieved using the refined SR method, delineated by a red dashed line. The methodology proposed herein effectively rectifies the inaccuracies induced by the homogeneous material assumption inherent in the traditional SR method. Moreover, it preserves the integrity of the horizontal variations in the dielectric constant, offering a more accurate depiction of the subsurface conditions.

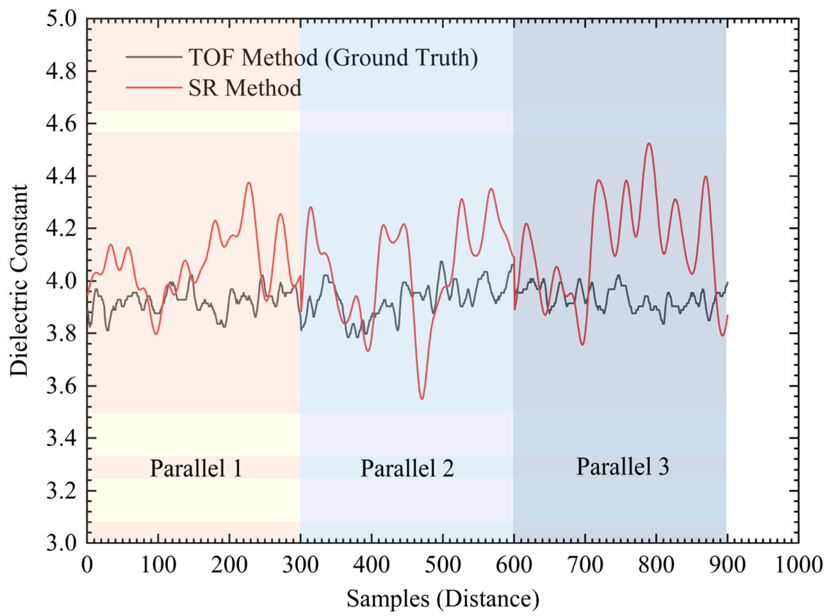

(a)

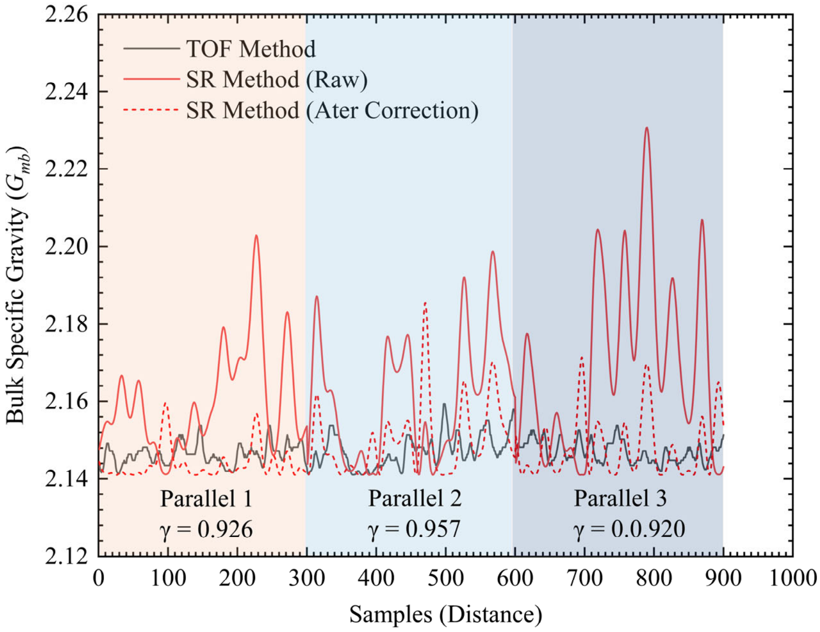

(b)

Figure 3.6 Simulation results of dielectric constant and bulk specific gravity of PA-10 mixture with an air void content of 18% and an antenna surface height of 0.3 m: (a) dielectric constant profile using TOF method and SR method; (b) corresponding bulk specific gravity before/after random pore distribution coefficient correction

The optimal random pore distribution coefficient for the other cases was also computed following the same optimization procedure. The random pore distribution coefficient for PA, SMA, and AC mixtures with different air void content and under different antenna surface height configurations was listed in Tables 3.2, 3.3, and 3.4, respectively. Each value in these tables is the average value of three parallels for each case. Lower random pore distribution coefficients were found in the PA mixture, compared with those of SMA and AC mixtures. This indicates that the ALL model deserves modification with a larger degree for PA pavement.

Table 3.2 Optimal random pore distribution coefficient for PA mixture

		Random Pore Distribution Coefficient				
		Antenna Height (m)				
NMAS (mm)	AV (%)	0.3	0.4	0.5	0.6	0.7
10	18	0.934	0.929	0.927	0.926	0.924
	19	0.933	0.933	0.936	0.936	0.935
	20	0.937	0.935	0.934	0.935	0.935
	21	0.939	0.937	0.937	0.938	0.938
	22	0.946	0.944	0.941	0.940	0.940
13	18	0.922	0.925	0.927	0.929	0.930
	19	0.922	0.924	0.926	0.928	0.930
	20	0.930	0.931	0.931	0.929	0.925
	21	0.929	0.930	0.931	0.931	0.931
	22	0.937	0.937	0.937	0.936	0.945
16	18	0.914	0.915	0.917	0.918	0.918
	19	0.917	0.916	0.917	0.916	0.915
	20	0.924	0.923	0.924	0.924	0.923
	21	0.926	0.926	0.926	0.926	0.925
	22	0.934	0.934	0.934	0.935	0.933

Table 3.3 Optimal random pore distribution coefficient for SMA mixture

		Random Pore Distribution Coefficient				
		Antenna Height (m)				
NMAS (mm)	AV (%)	0.3	0.4	0.5	0.6	0.7
10	3	0.968	0.969	0.968	0.969	0.969
	3.5	0.962	0.962	0.962	0.962	0.963
	4	0.961	0.962	0.963	0.963	0.963
	4.5	0.962	0.963	0.964	0.965	0.965
	5	0.963	0.964	0.964	0.964	0.964
13	3	0.969	0.970	0.971	0.971	0.971
	3.5	0.965	0.966	0.967	0.967	0.968
	4	0.965	0.967	0.968	0.968	0.968
	4.5	0.964	0.965	0.965	0.966	0.966
	5	0.960	0.962	0.962	0.962	0.963
16	3	0.964	0.966	0.966	0.967	0.967
	3.5	0.966	0.969	0.969	0.969	0.969
	4	0.966	0.968	0.969	0.969	0.969
	4.5	0.960	0.962	0.963	0.963	0.963
	5	0.960	0.962	0.963	0.964	0.964
20	3	0.966	0.968	0.969	0.970	0.971
	3.5	0.966	0.967	0.968	0.969	0.970
	4	0.964	0.966	0.960	0.968	0.968
	4.5	0.961	0.962	0.967	0.969	0.970
	5	0.960	0.963	0.964	0.966	0.967

Table 3.4 Optimal random pore distribution coefficient for AC mixture

		Random Pore Distribution Coefficient				
		Antenna Height (m)				
NMAS (mm)	AV (%)	0.3	0.4	0.5	0.6	0.7
10	3	0.968	0.969	0.969	0.969	0.969
	3.5	0.970	0.970	0.969	0.969	0.969
	4	0.965	0.966	0.966	0.965	0.965
	4.5	0.964	0.964	0.965	0.965	0.965
	5	0.966	0.966	0.966	0.966	0.966
13	3	0.967	0.967	0.967	0.967	0.967
	3.5	0.967	0.967	0.967	0.967	0.967
	4	0.963	0.963	0.964	0.964	0.964
	4.5	0.965	0.966	0.966	0.967	0.966
	5	0.963	0.964	0.963	0.963	0.962
16	3	0.960	0.961	0.962	0.963	0.964
	3.5	0.957	0.959	0.960	0.961	0.962
	4	0.958	0.960	0.961	0.962	0.962
	4.5	0.951	0.953	0.955	0.957	0.958
	5	0.957	0.959	0.960	0.960	0.960
20	3	0.980	0.981	0.981	0.981	0.981
	3.5	0.976	0.976	0.976	0.977	0.977
	4	0.980	0.982	0.983	0.984	0.984
	4.5	0.977	0.979	0.979	0.980	0.981
	5	0.976	0.977	0.977	0.978	0.978

3.2.3 Effect of Air Void Content and Antenna-Surface Height on Random Pore Distribution Coefficient

The effects of the air void content and antenna-surface height on the proposed coefficient were systematically investigated. Figure 3.7 illustrates the variation in the random pore distribution coefficient as a function of air void content within asphalt pavements. For SMA and AC mixtures, the random pore distribution coefficient remained relatively constant, ranging from 0.96 to 0.97, with a standard deviation of approximately 0.01. Contrastingly, the random pore distribution coefficient for the PA mixture exhibited an upward trend from 0.924 to 0.938 when the air void content increased from 18% to 22%. The standard deviation for this trend varied from 0.015 to 0.019, indicating a slight increase in variability. This phenomenon unveiled that a global random pore distribution coefficient can be used for AC and SMA mixture due to the relative same variation in air void. Inherent error exists for situations where a universal random pore distribution coefficient was used for PA mixture since an increasing trend can be observed.

This indicates that the accuracy increment of the proposed method on PA pavement density prediction exists but might be limited.

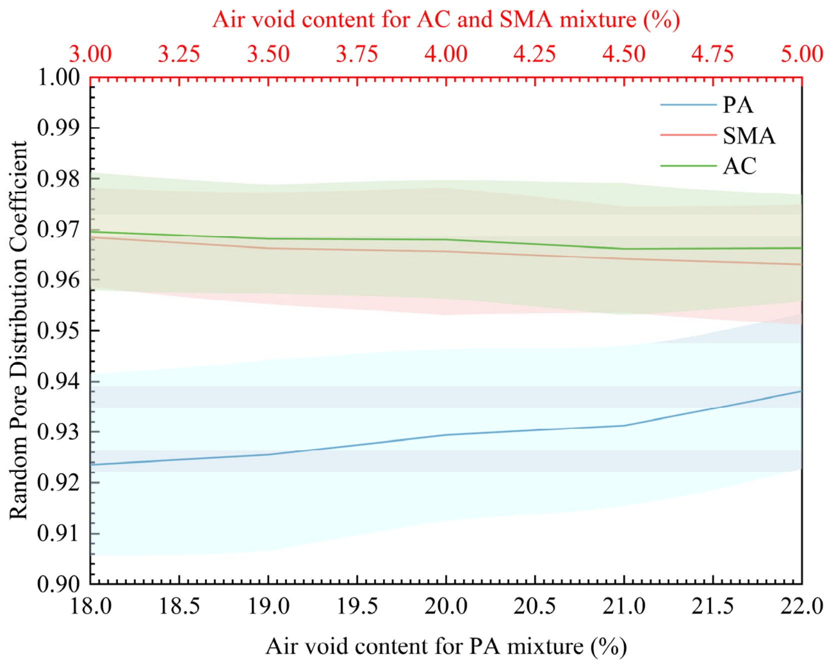

Figure 3.7 Effect of air void content of asphalt mixture on the proposed random pore distribution coefficient

In Figure 3.8, the random pore distribution coefficient sensitivity to variations in antenna-surface height was presented, which spanned from 0.3 m to 0.7 m. The random pore distribution coefficient for the PA mixture is stable at an average of 0.9, with a standard deviation of 0.18. For SMA and AC mixtures, the random pore distribution coefficient exhibited similar stability, fluctuating between 0.96 and 0.97, and a reduced standard deviation of 0.11 was observed. The alterations in the antenna-surface height are expected to influence the amplitude of surface reflected and refracted EM waves, which is caused by the energy attenuation within the air medium [90]. Nonetheless, the empirical results shown in Figure 3.8 suggest that this factor exerts a negligible impact on the determination of the random pore distribution coefficient within the scope of this study.

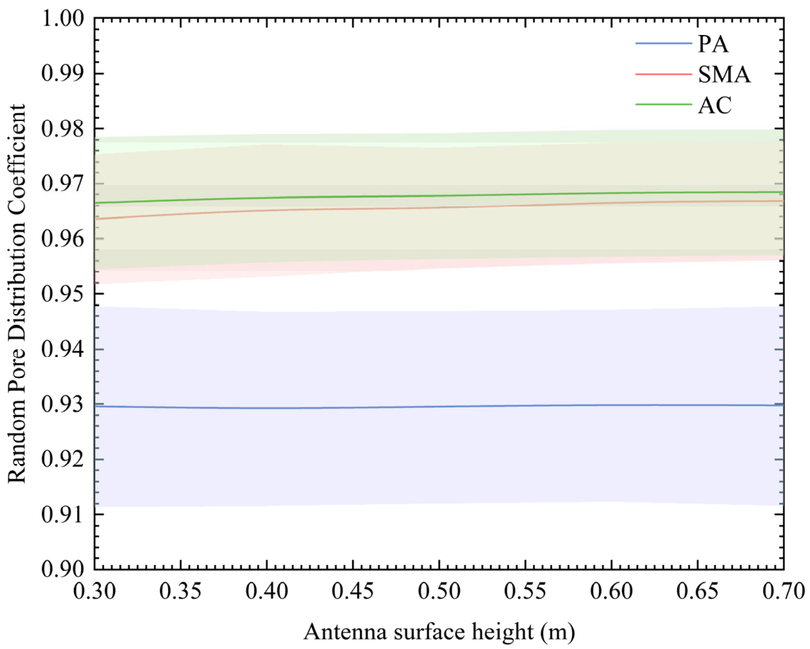

Figure 3.8 Effect of antenna surface height of asphalt mixture on the proposed random pore distribution coefficient

Dielectric constant profiles predicted through the SR method are presented in Figure 3.9 to further explore the influence of antenna-surface height. These profiles demonstrate that the antenna-surface height induces variations in the dielectric constant at different survey locations. An increase in antenna-surface height tends to result in an underestimation of the dielectric constant in regions with higher aggregate concentration (peaks). Simultaneously, antenna-surface height increment will overestimate the dielectric constant in areas with lower aggregate concentration presence (valleys) and vice versa. The degree of the under- and over-estimation of the dielectric constant increases as the antenna height increases. However, these concurrent underestimations and overestimations statistically counterbalance each other. The possible reason lies in the pore structure patterns. The air void distribution within the asphalt mixture obeys the normal distribution, which is symmetrical. This leads to an observed insensitivity of the proposed coefficient to changes in antenna-surface height. It is suggested to disregard the effect of antenna-surface height in the determination of the proposed coefficient for practical applications. According to results from next chapter, a lower antenna height decreases the inherent error caused by the SR method. Therefore, the lowest antenna height from the GPR vendor's recommendation is suggested for in-situ density prediction.

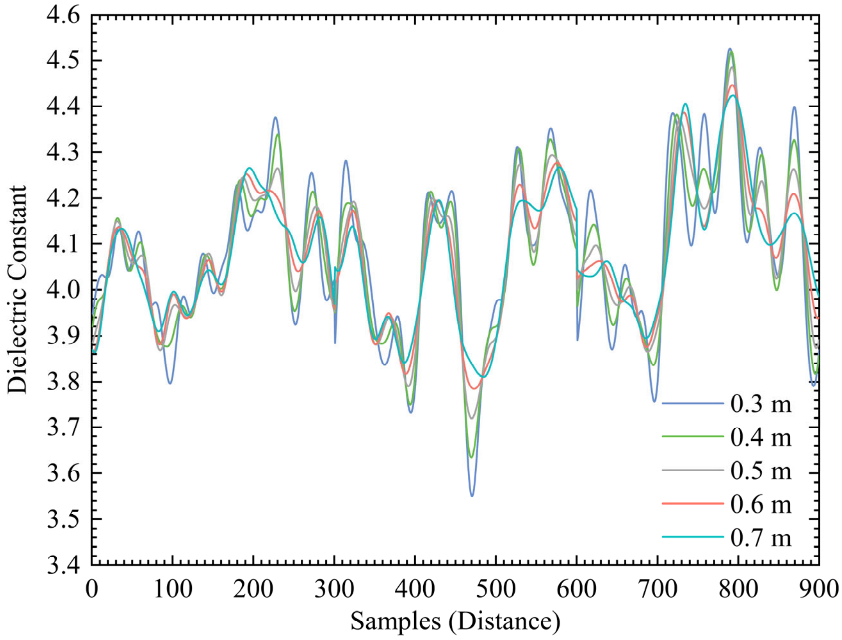

Figure 3.9 Dielectric constant profile of PA-10 mixture with an air void content of 18% using SR method with varying antenna surface height

3.2.4 Random Pore Distribution Coefficient Determination

To obtain the optimal random pore distribution coefficient for each mixture type, the sum of RMSE for all test cases corresponding to a specific mixture type was computed by iteratively adjusting the coefficient within a range of 0.9 to 1. This iterative process aimed to find the minimal sum of RMSE, thereby identifying the most suitable coefficient for each mixture type. Figure 3.10 graphically represents this optimization procedure.

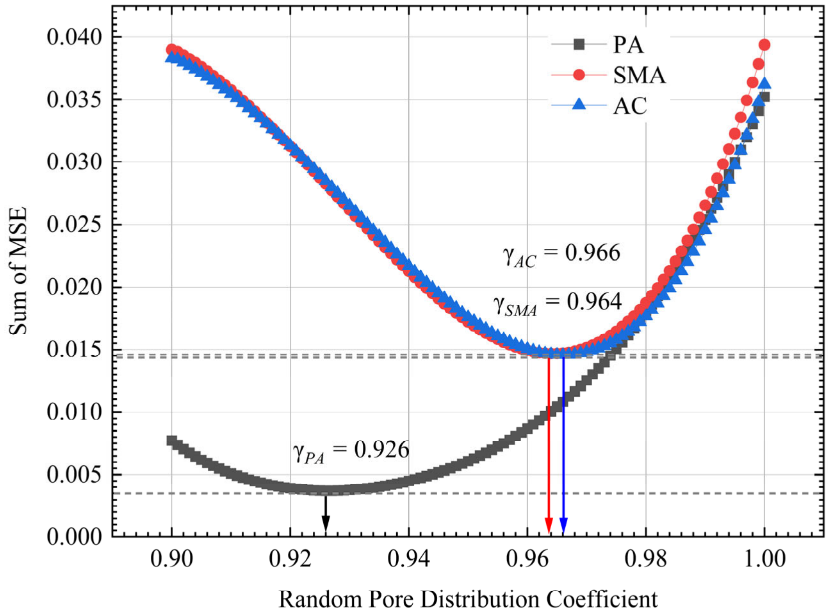

Figure 3.10 Optimal value of random pore distribution coefficient for PA, SMA and AC mixture

The analysis yielded the optimal random pore distribution coefficient that minimizes the G_{mb} estimation error for each mixture type. Specifically, the random pore distribution coefficient of 0.926 was found to be optimal for the PA mixture, while SMA and AC mixtures achieved their minimal estimation errors with random pore distribution coefficients of 0.964 and 0.966, respectively. Incorporating these optimized coefficients into equation 4 enables the formulation of modified ALL models tailored to each mixture type, as expressed in the following equations:

$$G_{mb} = \frac{\frac{0.928\varepsilon_{PA}-\varepsilon_b}{2.784\varepsilon_{PA}-2.3\varepsilon_b} - \frac{1-\varepsilon_b}{1+1.856\varepsilon_{PA}-2.3\varepsilon_b}}{\left(\frac{\varepsilon_s-\varepsilon_b}{\varepsilon_s+1.856\varepsilon_{PA}-2.3\varepsilon_b}\right)\left(\frac{1-P_b}{G_s}\right) - \left(\frac{1-\varepsilon_b}{1+1.856\varepsilon_{PA}-2.3\varepsilon_b}\right)\left(\frac{1}{G_{mm}}\right)} \quad (3-4)$$

$$G_{mb} = \frac{\frac{0.964\varepsilon_{SMA}-\varepsilon_b}{2.892\varepsilon_{SMA}-2.3\varepsilon_b} - \frac{1-\varepsilon_b}{1+1.928\varepsilon_{SMA}-2.3\varepsilon_b}}{\left(\frac{\varepsilon_s-\varepsilon_b}{\varepsilon_s+1.928\varepsilon_{SMA}-2.3\varepsilon_b}\right)\left(\frac{1-P_b}{G_s}\right) - \left(\frac{1-\varepsilon_b}{1+1.928\varepsilon_{SMA}-2.3\varepsilon_b}\right)\left(\frac{1}{G_{mm}}\right)} \quad (3-5)$$

$$G_{mb} = \frac{\frac{0.966\varepsilon_{AC}-\varepsilon_b}{2.898\varepsilon_{AC}-2.3\varepsilon_b} - \frac{1-\varepsilon_b}{1+1.932\varepsilon_{AC}-2.3\varepsilon_b}}{\left(\frac{\varepsilon_s-\varepsilon_b}{\varepsilon_s+1.932\varepsilon_{AC}-2.3\varepsilon_b}\right)\left(\frac{1-P_b}{G_s}\right) - \left(\frac{1-\varepsilon_b}{1+1.932\varepsilon_{AC}-2.3\varepsilon_b}\right)\left(\frac{1}{G_{mm}}\right)} \quad (3-6)$$

3.3 Laboratory Test Validation

3.3.1 Ground Truth Density Measurement

Controlled laboratory tests on SGC specimens were conducted to validate the proposed model's performance. 22 SGC specimens were manufactured under Superpave specification [91], including 11 mix types of the same gradation as those used in numerical simulations. G_{mm} was measured before specimen manufacturing using loose aggregate coated with asphalt binder [92]. Saturated surface dry (SSD) method was used to measure G_{mb} of AC and SMA mixture, while the CoreLok method was used for the PA mixture due to its high air void content [93]. SSD and CoreLok methods use the following equations to calculate the bulk specific gravity, respectively:

$$G_{mb} = \frac{A}{B - C} \qquad (3-7)$$

where A is the air-dried weight of the specimen in air; B is the saturated surface dry weight; and C is the submerged weight.

$$G_{mb} = \frac{A}{(A + B - C) - \left(\frac{B}{D}\right)} \qquad (3-8)$$

where A is the sample weight; B is the plastic bag weight; C is the wrapped sample weight in water; and D is the plastic bag density. The manufactured SGC specimen and testing procedure is depicted in Figure 3.11.

(a) (b) (c)

Figure 3.11 SGC specimen preparation and ground truth density measurement: (a) Manufactured SGC specimens; (b) SSD method; (c) CoreLok method

3.3.2 Density Prediction Using GPR

The dielectric constant of the SGC specimens was measured using 2GHz palm radar. The interaction of the multiple reflected or refracted EM waves at the specimen surface can lead to the edge diffraction effect. This phenomenon manifests when the antenna is in direct contact with the specimen, operating as a ground-coupled antenna, or when it is elevated above the specimen, functioning as an air-coupled antenna. In the latter scenario, the diffraction occurs because the EM wave's footprint surpasses the boundaries of the SGC specimen surface.

The air-coupled configuration was incorporated with a spacer method to mitigate the edge diffraction effect, as illustrated in Figure 3.12 (a) [94, 95]. The fundamental concept of this approach involves diminishing the EM wave propagation velocity by inserting a dielectric spacer between the antenna and the specimen. This adjustment helps confine the EM wave's footprint within the boundaries of the specimen's surface. It is essential that the dielectric property of the spacer be intermediate, with a dielectric constant greater than that of air but less than that of the specimen. Such a demand is crucial to preserve a discernible dielectric constant contrast between the spacer and the specimen. This thereby ensures a detectable reflection is present in the GPR data.

For the purposes of this study, polyoxymethylene (POM), a thermoplastic with a known dielectric constant of 2.88, was selected as the spacer material. Utilizing this configuration, the dielectric constant of the SGC specimens was determined using the SR method based on the following equation [95]:

$$\varepsilon_{AC} = \varepsilon_{spacer} \sin^2 \theta_i + \varepsilon_{spacer} \left[\frac{1 + \frac{A_{sn}}{A_{mn}}}{1 - \frac{A_{sn}}{A_{mn}}} \right]^2 (1 - \sin^2 \theta_i) \qquad (3-9)$$

where ε_{spacer} is the dielectric constant of the spacer material; θ_i is the angle of incident wave, which is calculated from the specific configuration between the spacer and the antenna; A_{sn} is the negative peak amplitude of the sample reflection; and A_{mn} is the negative peak amplitude of the metal plate reflection.

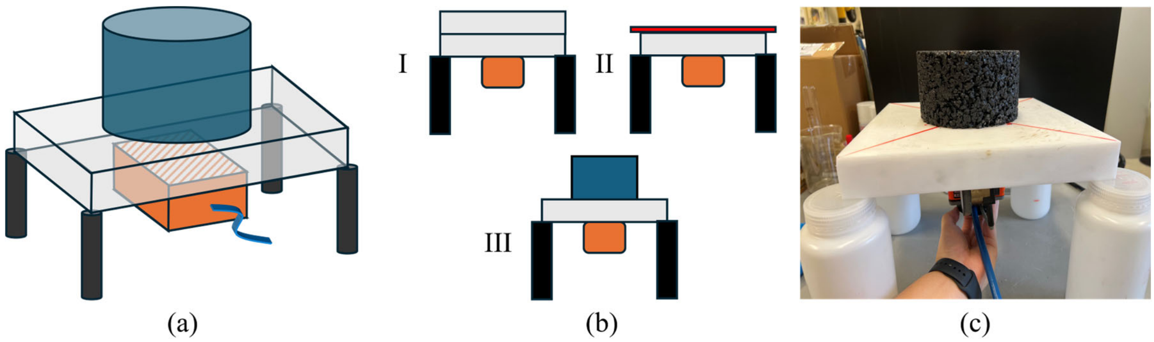

Figure 3.12 Dielectric constant measurement on SGC specimen using GPR and the spacer method: (a) diagram of the test settings; (b) configuration of synthetic signals for SR and TOF method; (c) test photo

Given the known distance between the transmitter and the receiver of the antenna equals 6 cm and the thickness of the spacer equals to 4 cm, the sin θ_i is calculated as 0.6. A_{sn} and A_{mn} can be determined by conducting GPR measurements under the specific configurations as depicted in Figure 3.12. (b). Synthetic signal I is obtained by subtracting signal I (pure spacer material) from signal II (spacer and metal plate). Synthetic signal II can be obtained by subtracting signal I from signal III (Spacer and target specimen). Then, A_{sn} and A_{mn} can be determined by searching the first negative peak amplitude of the synthetic I and II, respectively, as illustrated in Figure 3.13.

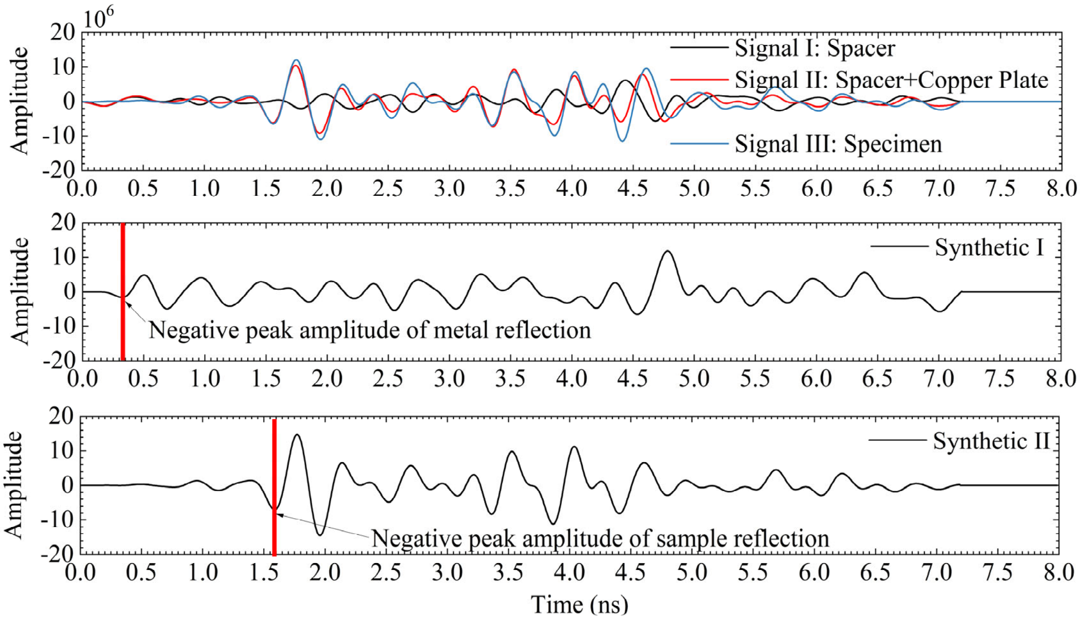

Figure 3.13 Synthetic signals for dielectric constant estimation using SR and TOF method under the spacer method configuration

3.3.3 Results and Discussion

Table 3.5 provides the ground truth compaction characteristics of the specimens as determined in a controlled laboratory setting. These characteristics encompass the specimen height, bulk specific gravity (G_{mb}), theoretical maximum specific gravity (G_{mm}), and the AV. The observed air void content for PA, SMA, and AC mixtures ranges from 17.63% to 22.58%, 2.18% to 4.61%, and 3.41% to 5.86%, respectively. The recorded span of AV values aligns with the range implemented in the numerical simulations.

Table 3.5 Test results of the ground truth density of SGC specimens

Specimen No.	Height (cm)	G_{mb} (Ground truth)	G_{mm}	AV (%)
PA-10-1	8.8	1.881	2.423	22.37
PA-10-2	8.5	1.876	2.423	22.58
PA-13-1	8.7	2.019	2.451	17.63
PA-13-2	8.6	2.001	2.451	18.36
PA-16-1	9.5	1.941	2.440	20.47
PA-16-2	8.5	1.921	2.440	21.29
SMA-10-1	9.0	2.320	2.402	3.41
SMA-10-2	8.7	2.319	2.402	3.47
SMA-13-1	8.5	2.319	2.416	4.00
SMA-13-2	9.0	2.305	2.416	4.61
SMA-16-1	8.8	2.310	2.402	3.86
SMA-16-2	8.8	2.308	2.402	3.91
SMA-20-1	8.7	2.377	2.430	2.18
SMA-20-2	8.8	2.372	2.430	2.37
AC-10-1	9.0	2.294	2.406	4.65
AC-10-2	8.5	2.312	2.406	3.89
AC-13-1	8.6	2.291	2.420	5.32
AC-13-2	8.9	2.278	2.420	5.86
AC-16-1	9.0	2.352	2.461	4.44
AC-16-2	8.6	2.378	2.461	3.41
AC-20-1	8.8	2.342	2.440	4.04
AC-20-2	8.9	2.340	2.440	4.11

The measured dielectric properties of the specimens were presented in Table 3.6. The compaction properties estimated using the ALL model in conjunction with SR and the proposed method were also given. The TOF method was involved in predicting the dielectric constant to furnish a benchmark for the efficacy of the proposed density prediction model. Concurrently, G_{mb} associated with the TOF method was also computed. It should be noted that the dielectric constant of the asphalt binder and the aggregate remain constant during the measurement, since the type of material unchanged.

Table 3.6 Predicted dielectric constant and the bulk specific gravity of asphalt mixture using SR method, TOF method, and the proposed method

Specimen No.	ε_{AC} (SR)	ε_{AC} (TOF)	G_{mb} (SR)	G_{mb} (TOF)	G_{mb} (Proposed)
PA-10-1	5.808	4.139	2.517	2.124	2.387
PA-10-2	5.797	4.198	2.514	2.132	2.384
PA-13-1	5.537	4.230	2.449	2.148	2.331
PA-13-2	5.840	4.776	2.535	2.254	2.404
PA-16-1	5.966	4.047	2.568	2.120	2.432
PA-16-2	6.175	3.981	2.630	2.114	2.486
SMA-10-1	5.084	4.705	2.312	2.220	2.261
SMA-10-2	5.398	4.786	2.395	2.239	2.337
SMA-13-1	5.622	4.883	2.462	2.267	2.399
SMA-13-2	5.872	4.815	2.534	2.251	2.466
SMA-16-1	5.289	4.796	2.366	2.241	2.310
SMA-16-2	5.053	4.683	2.304	2.216	2.254
SMA-20-1	5.881	4.902	2.540	2.276	2.473
SMA-20-2	6.049	4.910	2.590	2.278	2.519
AC-10-1	5.520	4.705	2.430	2.222	2.369
AC-10-2	5.275	4.765	2.363	2.235	2.308
AC-13-1	5.425	4.893	2.408	2.270	2.350
AC-13-2	5.643	4.367	2.469	2.158	2.406
AC-16-1	5.565	4.815	2.460	2.266	2.399
AC-16-2	5.644	4.776	2.482	2.257	2.419
AC-20-1	5.306	4.683	2.382	2.229	2.327
AC-20-2	5.564	4.694	2.453	2.232	2.392

It is noted that the dielectric constant predicted via the TOF method could be considered as the ground truth value in controlled laboratory tests. This can be theoretically implemented by embedding metal plates beneath the asphalt layer to simulate a known reference point. Nevertheless, G_{mb} estimated using the TOF method cannot be equated to a ground truth value because it can be hardly achieved in field applications. This limitation restricted its application in EM mixing-based density prediction models, including but not limited to the ALL model.

For an accurate ground truth benchmark of G_{mb}, the abovementioned laboratory-based measurement methods were employed, including SSD and CoreLok, with detailed results presented in Table 3.5. These methods are recognized for their precision in determining the actual compaction properties of pavement materials, thereby providing reliable benchmarks for validating the predicted models.

The SR method is observed to systematically overestimate the dielectric constant compared to the TOF method, which consequently leads to an inflated G_{mb} value. This discrepancy can be mitigated by incorporating the proposed random pore distribution coefficient into the ALL model (with values of 0.926, 0.964, and 0.966 for PA, SMA, and AC mixtures). The relative estimation errors for G_{mb} using the SR, the proposed random pore distribution coefficient adjusted method, and the TOF method against the ground truth measurements for each asphalt mixture type were computed to evaluate the efficacy of this corrective approach. These comparisons are depicted in Figures 3.14, 3.15, and 3.16.

Results presented in Figure 3.14 indicate that the estimation error of G_{mb} of the PA mixture fluctuates around 30% using the conventional ALL model. Incorporation of the random pore distribution coefficient into the ALL model significantly reduces the estimation error to a range between 5.85% and 7.53%. The achievement of higher prediction accuracy can also be verified by examining the sum relative error for different adopted methods. The sum error reduced from 185% to 144% after correction. Nevertheless, the corrected estimation error exceeds 15%, indicating that the precision of the ALL model for PA mixtures remains insufficient. Even when the dielectric constant is estimated using the TOF method, the resultant G_{mb} prediction error persists at approximately 10%. These findings underscore the necessity for further improvements to the ALL model to enhance its accuracy and reliability for applications in PA mixtures.

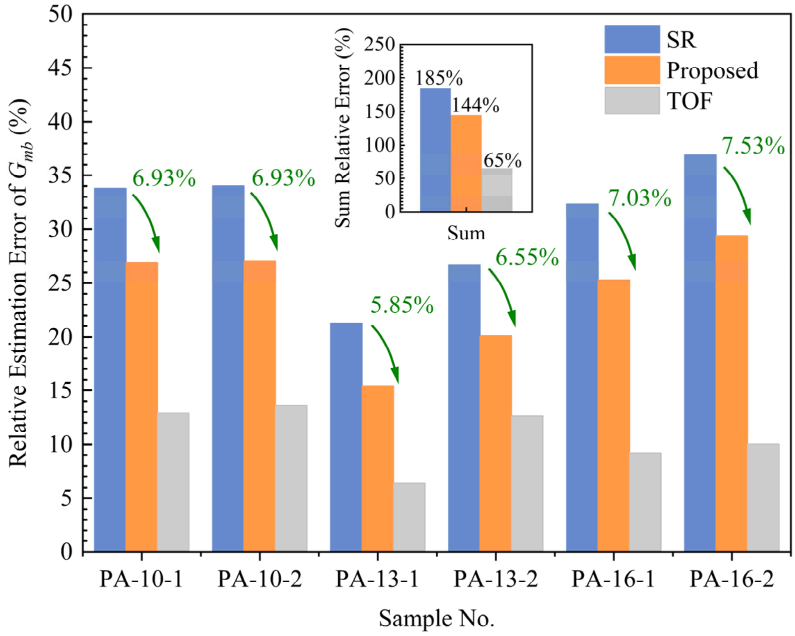

Figure 3.14 Bulk specific gravity estimation error for PA specimens using ALL model in conjunction with SR, proposed, and TOF method

Results illustrated in Figure 3.15 reveal that the implementation of the proposed correction methodology enhances the accuracy of in-situ G_{mb} estimation for SMA mixture. The application of this method yields a reduction in the relative error of G_{mb} estimates, with a diminishment ranging from 2.40% to 2.99% for most of the samples evaluated. Notably, two exceptions were observed in the cases of samples SMA-10-1 and SMA-16-2, where G_{mb} estimations via the SR method were anomalously congruent with the ground truth values. Therefore, the application of the proposed corrections inadvertently resulted in less accurate outcomes. Despite these outliers, the improvement in G_{mb} prediction across all samples is statistically significant. The sum of relative error across all samples using the proposed correction method is quantified at 26%, which exhibits an improvement compared to 28% observed when employing the TOF method. This comparative analysis reinforces the necessity and superiority of the proposed correction approach for the precision enhancement of G_{mb} estimations.

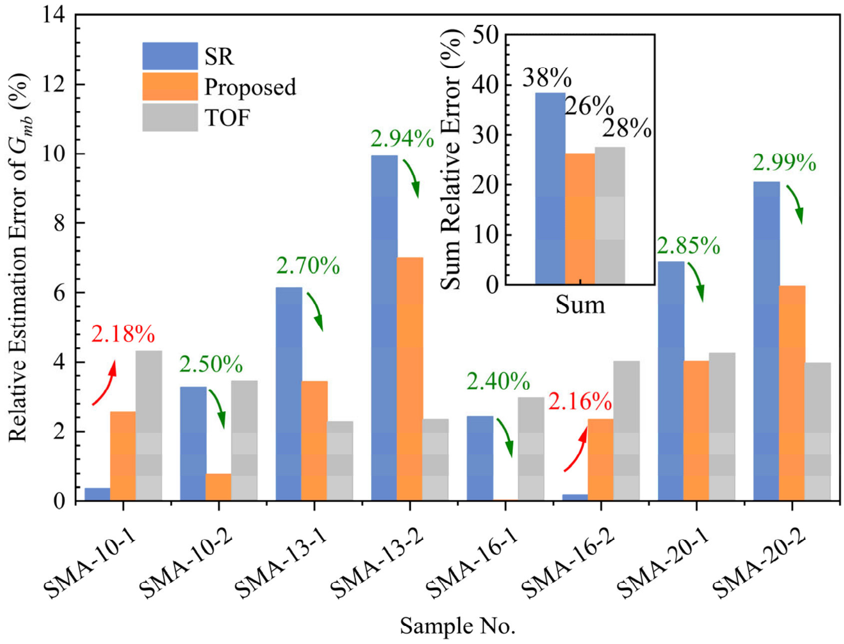

Figure 3.15 Bulk specific gravity estimation error for SMA specimens using ALL model in conjunction with SR, proposed, and TOF method

Precision improvement of G_{mb} for AC mixture is close to those of the SMA mixture, ranging from 1.08% to 2.77%, as illustrated in Figure 3.16. A better improvement occurs to the sum relative error compared to the TOF method. This indicates that the ALL model using dielectric constant estimated through the SR method can achieve comparable or better performance (18%) than that of the TOF method (31%) on the condition that the material vertical heterogeneity is taken into consideration.

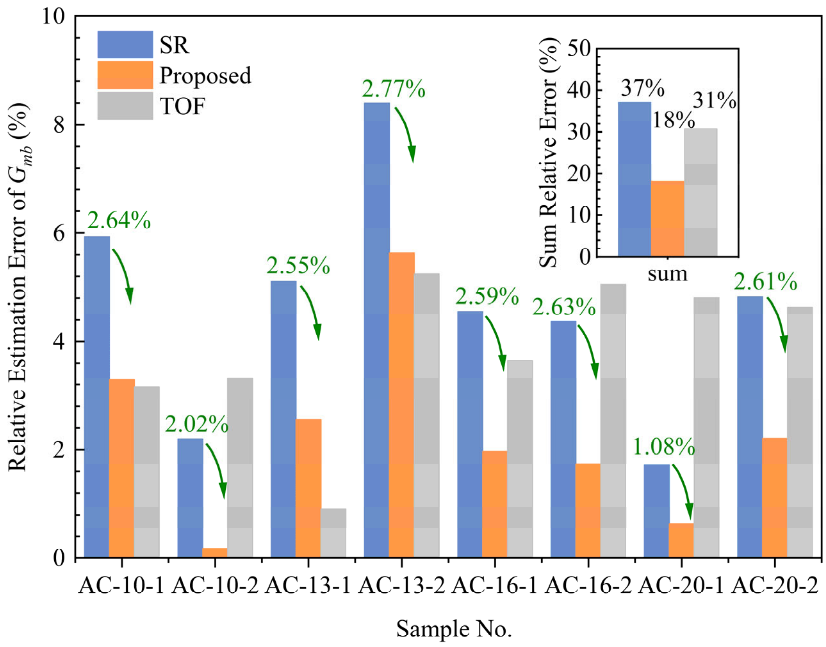

Figure 3.16 Bulk specific gravity estimation error for AC specimens using ALL model in conjunction with SR, proposed, and TOF method

Density prediction performance using the proposed revised ALL model and the ISO model were compared, as seen in Figure 3.17. Lower bulk specific gravity estimation error was achieved using the proposed method for all specimens. This result highlights the significance, and the necessity of the optimization process adopted in this research, which is in line with the other optimization process towards the GPR-based in-situ density prediction [96].

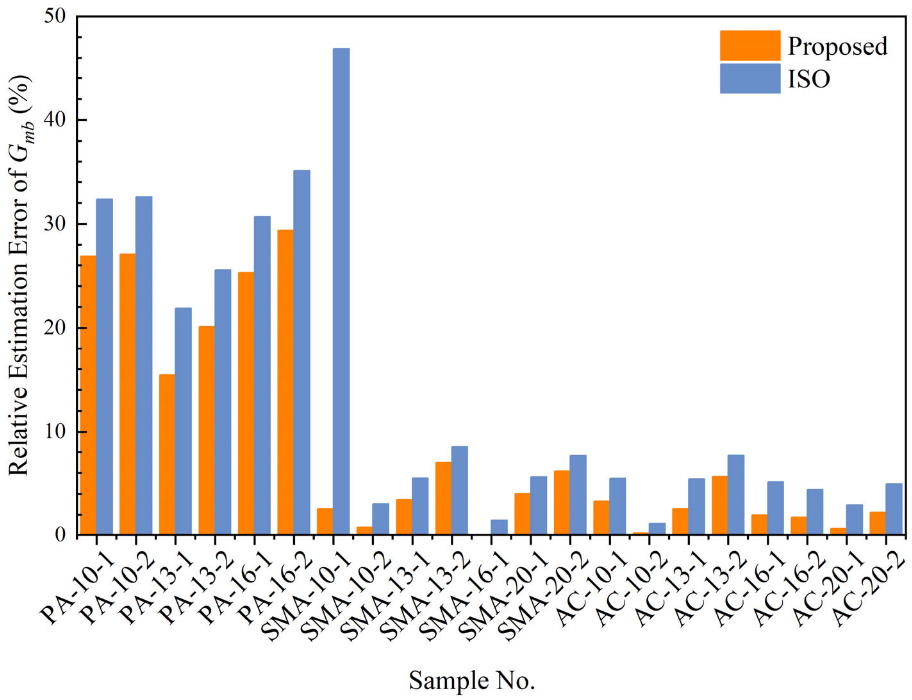

Figure 3.17 Bulk specific gravity estimation error for AC specimens using the proposed revised ALL method and the ISO method

3.4 Summary

In this chapter, the ALL model was modified to provide accurate asphalt pavement density predictions, incorporating a proposed random pore distribution coefficient considering the vertical dielectric heterogeneity. The optimal random pore distribution coefficient for PA, SMA, and AC mixtures was determined using a meso-scale EM modelling approach. Effects of air void content and antenna-surface height on the random pore distribution coefficient were systematically studied. Comprehensive laboratory tests involving SGC specimens were conducted. GPR measurements were conducted under the air-coupled configuration using a spacer method to mitigate the edge diffraction effect during laboratory tests. Main findings are drawn as follows:

(1) A random pore distribution coefficient was proposed to modify the ALL model, eliminating the potential density prediction errors caused by the homogeneity assumption. The identified optimal random pore distribution coefficient for PA, SMA,

and AC mixtures is 0.926, 0.964, and 0.966, respectively. After correction, the prediction accuracy of bulk specific gravity improved by 6.69%, 2.70%, and 1.93% for the respective mixtures. Such level of accuracy enhancement compensated density prediction using GPR (3% to 10%), as well as the corresponding reliability.

(2) The random pore distribution coefficient for PA mixtures exhibits a positive correlation when increasing the air void content, whereas it remains relatively invariant for SMA and AC mixtures. Variations in antenna-surface height were observed to influence the predicted dielectric constant profiles. Despite this, its impact on the random pore distribution coefficient determination could be statistically negligible, as the concurrent underestimation and overestimation across regions of varying aggregate concentration could effectively cancel each other out.

(3) The density prediction of PA pavement using the ALL model remains challenging. Although the proposed approach can enhance the prediction performance, the average relative estimation error exceeds 20%. Future work is required to refine the ALL model and reduce this residual error.

CHAPTER 4 REMOVAL OF THE GPR ANTENNA VIBRATION EFFECT FOR ENHANCED MULTI-LAYER ASPHALT PAVEMENT THICKNESS DETERMINATION

This chapter aims to reduce the influence of the antenna vibration effect on the GPR-based multi-asphalt layer pavement thickness determination by considering the antenna height shifting. First, the relationship between the surface, interfaces, bottom, and incident reflection amplitudes with antenna height was established by developing numerical electromagnetic models for multi-asphalt layer pavements. Subsequently, a HC-SR method was proposed to correct the estimation of the dielectric constant, followed by the development of a corresponding framework for determining the thickness of multi-asphalt layer pavement. Field tests were conducted, including stationary bouncing tests and continuous surveys. In-situ cores were extracted for validation. Ultimately, a more accurate GPR-based method for determining the thickness of multi-asphalt layer pavement, considering the effect of antenna height shifts, was proposed. This method can be applied to automated inspections of both newly paved highways and existing urban roads in the future.

4.1 Methodology

Figure 4.1 presents a flowchart summarizing the primary methodology employed in this study. This section provided an introduction to the conventional surface reflection method used for predicting the thickness of multi-asphalt layers. Subsequently, existing models describing the relationship between antenna height and the surface reflection amplitude were presented. In next section, the correlation between antenna height and interface reflection amplitude is investigated through the development of numerical models for multi-asphalt layer pavement systems. A modification of the typical surface reflection method was implemented in this section by substituting measured reflection amplitudes from raw GPR signals with calculated reflection amplitudes obtained from the antenna height-reflection amplitude relationship. The performance of the modified method was then validated using an authentic numerical model of the multi-asphalt layer pavement system, which incorporated random antenna vibration. The final section focus on the validation of the modified surface reflection method using field data.

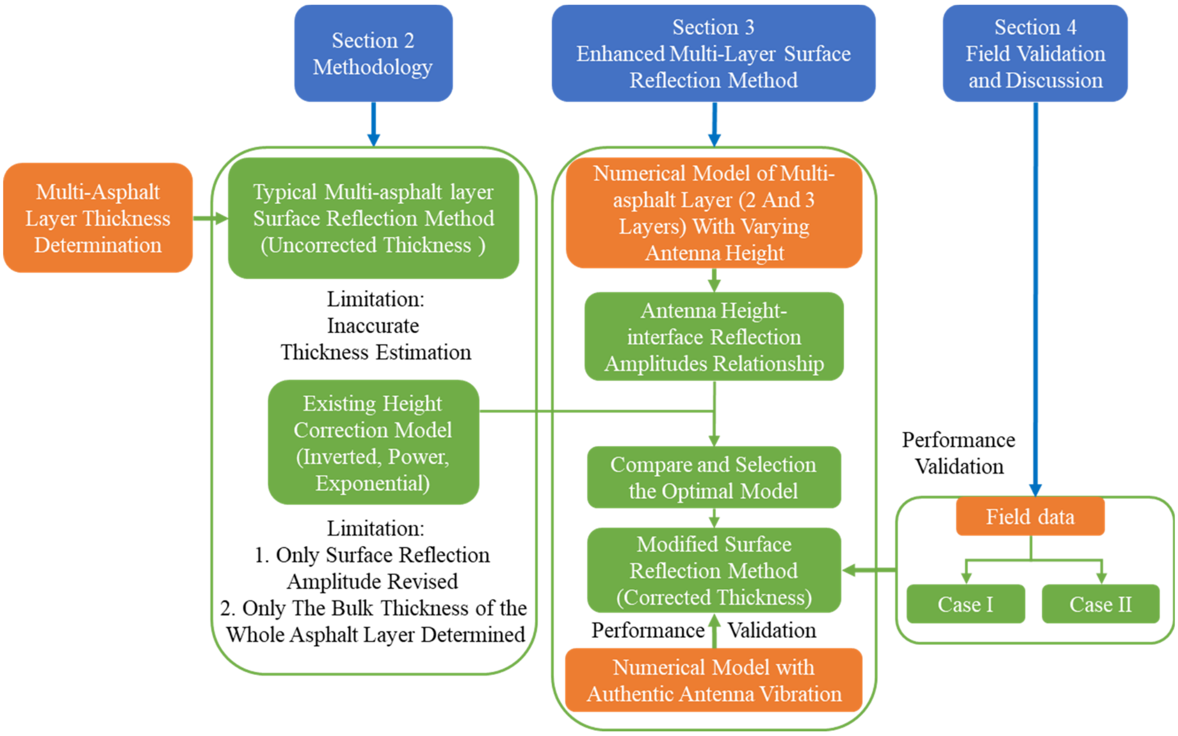

Figure 4.1 Flowchart of the adopted methodology

4.1.1 Dielectric Constant Estimation Using Surface Reflection Method

According to the EM theory, the layer thickness of a multi-asphalt layer pavement system can be determined using its relationship with the dielectric constant and the TWTT of the EM wave within the asphalt pavement structure, as shown in the following equations:

$$d_i = \frac{ct_i}{2\sqrt{\varepsilon_{r,i}}} \qquad (4-1)$$

where d_i, t_i, and $\varepsilon_{r,i}$ are the thickness, the TWTT, and the dielectric constant of the i^{th} asphalt layer, respectively. It can be seen that an accurate estimation of asphalt layer thickness depends on the accurate determination of the TWTT and the estimation of the dielectric constant. The relationship between dielectric constant and the amplitude of adjacent reflection pulses is governed by the following equation, which is derived from the expression of the reflectivity function of (*N+1*) layers pavement system [33].

$$\frac{A_n}{A_{inc}} = \frac{\sqrt{\varepsilon_{r,n+1}} - \sqrt{\varepsilon_{r,n}}}{\sqrt{\varepsilon_{r,n+1}} + \sqrt{\varepsilon_{r,n}}} \left[\prod_{i=0}^{n-1} (1 - \gamma_i^2) \right] e^{-\eta_0 \sum_{i=0}^{n} \frac{\sigma_i d_i}{\sqrt{\varepsilon_{r,i}}}} \quad n = 0, 1, \dots N - 1 \qquad (4-2)$$

where A_n is the reflection amplitude of the interface between n^{th} and $(n+1)^{th}$ layers. Particularly, when $n = 0$, A_0 represents the surface reflection amplitude; A_{inc} is the reflection amplitude of the incident EM wave. This value is normally measured in the field survey by placing a perfect reflector, such as a copper plate, right beneath the air-coupled antenna; $\varepsilon_{r,n}$, $\varepsilon_{r,n+1}$, $\varepsilon_{r,i}$ are the dielectric constant of the n^{th}, $(n+1)^{th}$, and i^{th} layer, respectively; η_0 is the wave impedance of free space; σ_i is the conductivity of the i^{th} layer; and γ_i is the reflection coefficient at the i^{th} interface, which can be calculated using the following equation:

$$\gamma_i = \frac{\sqrt{\varepsilon_{r,i+1}} - \sqrt{\varepsilon_{r,i}}}{\sqrt{\varepsilon_{r,i+1}} + \sqrt{\varepsilon_{r,i}}} \qquad (4-3)$$

Note that the conductivity of asphalt mixtures can be assumed as zero, leading to the exponential term as one. Then, Equation (4-3) becomes:

$$\frac{A_n}{A_{inc}} = \frac{\sqrt{\varepsilon_{r,n+1}} - \sqrt{\varepsilon_{r,n}}}{\sqrt{\varepsilon_{r,n+1}} + \sqrt{\varepsilon_{r,n}}} \left[\prod_{i=0}^{n-1} (1 - \gamma_i^2) \right] \quad n = 0, 1, \dots N - 1 \qquad (4-4)$$

By substituting $n = 0, 1, 2, \dots$ and n, the estimated dielectric constant of the first, second, third, and the n^{th} layer can be obtained, as shown in Equation (4-5) - (4-8).

$$\varepsilon_{r,1} = \left(\frac{1 + \frac{A_0}{A_{inc}}}{1 - \frac{A_0}{A_{inc}}} \right)^2 \qquad (4-5)$$

$$\varepsilon_{r,2} = \varepsilon_{r,1}\left(\frac{1-\left(\frac{A_0}{A_{inc}}\right)^2+\frac{A_1}{A_{inc}}}{1-\left(\frac{A_0}{A_{inc}}\right)^2-\frac{A_1}{A_{inc}}}\right)^2 \tag{4-6}$$

$$\varepsilon_{r,3} = \varepsilon_{r,2}\left(\frac{1-\left(\frac{A_0}{A_{inc}}\right)^2-\gamma_1\frac{A_1}{A_{inc}}+\frac{A_2}{A_{inc}}}{1-\left(\frac{A_0}{A_{inc}}\right)^2-\gamma_1\frac{A_1}{A_{inc}}-\frac{A_2}{A_{inc}}}\right)^2 \tag{4-7}$$

$$\varepsilon_{r,n} = \varepsilon_{r,n-1}\left(\frac{1-\left(\frac{A_0}{A_{inc}}\right)^2-\sum_{i=1}^{n-2}\gamma_i\frac{A_i}{A_{inc}}+\frac{A_{n-1}}{A_{inc}}}{1-\left(\frac{A_0}{A_{inc}}\right)^2-\sum_{i=1}^{n-2}\gamma_i\frac{A_i}{A_{inc}}+\frac{A_{n-1}}{A_{inc}}}\right)^2 \tag{4-8}$$

4.1.2 Antenna Height Correction Model

The existing antenna height correction models, such as the inverse model [49], power model [8], and exponential model [50] are given in the following equations:

$$A = \frac{b}{a + D_t} \tag{4-9}$$

$$A = ah^b \tag{4-10}$$

$$A = ae^{bh} \tag{4-11}$$

where A is the reflection amplitude at the pavement surface; a and b are regression coefficients; and D_t is the time delay of the direct wave between the transmitting and receiving antenna. Note that these models are effective when considering multiple asphalt layers as a single entity and only incorporating the surface reflection amplitude. Any variations in the dielectric constant caused by different materials and mix designs between the asphalt layers are disregarded. However, this assumption is not suitable for tasks involving the determination of multi-asphalt layer thickness, as it may introduce errors due to the uncorrected subsurface reflection amplitudes.

4.2 Enhanced Multi-Asphalt Layer Surface Reflection Method

4.2.1 Antenna Height and Reflection Amplitude Correlation Model

The multi-layer antenna height correction models were developed using gprMax2D. These models were divided into two categories: the antenna height shifting models and the validation model. In the antenna height shifting models, both two-asphalt layer and three-asphalt layer pavement system were considered, whose geometric configurations are illustrated in Figure 4.2 (a). The dielectric property settings of all models are provided in Table 4.1. In total, 90 numerical models were created, comprising 58 two-asphalt layer models, 30 three-asphalt layer models, 1 metal plate calibration model, and 1 validation model.. To efficiently compute the antenna height changes, the transmitting (Tx) and receiving (Rx) dipole antenna pair were moved both horizontally and vertically, resulting in a total antenna height variation of 0.5 m. The excitation source was set as a Ricker waveform with a central frequency of 2 GHz, which is commonly used in commercial air-coupled GPR systems. Perfectly matched layer (PML) boundary conditions were applied in both the X and Y directions. The resulting GPR B-scan (in grayscale) is depicted in Figure 4.2 (b). Notably, a strong reflection raised from the direct coupling pulse was observed, camouflaging the target pulse's reflections. To address this, a decoupling process was implemented to remove the direct coupling effect, revealing the pavement reflections, as shown in Figure 4. 2 (c). Typical GPR signals for two and three asphalt layers are presented in Figure 4.3 (a) and (b), respectively. The notable waveforms include the surface reflection, interface reflection (one for a two-layer system and two for a three-layer system), bottom reflection between the asphalt layers and base layer, and the base/subgrade reflection. It can be noticed that the surface reflection and the interface reflection between first and second layers overlap partially, which is attributed to the the thin first asphalt layer used to simulate the thin overlay scenarios encountered in field application.

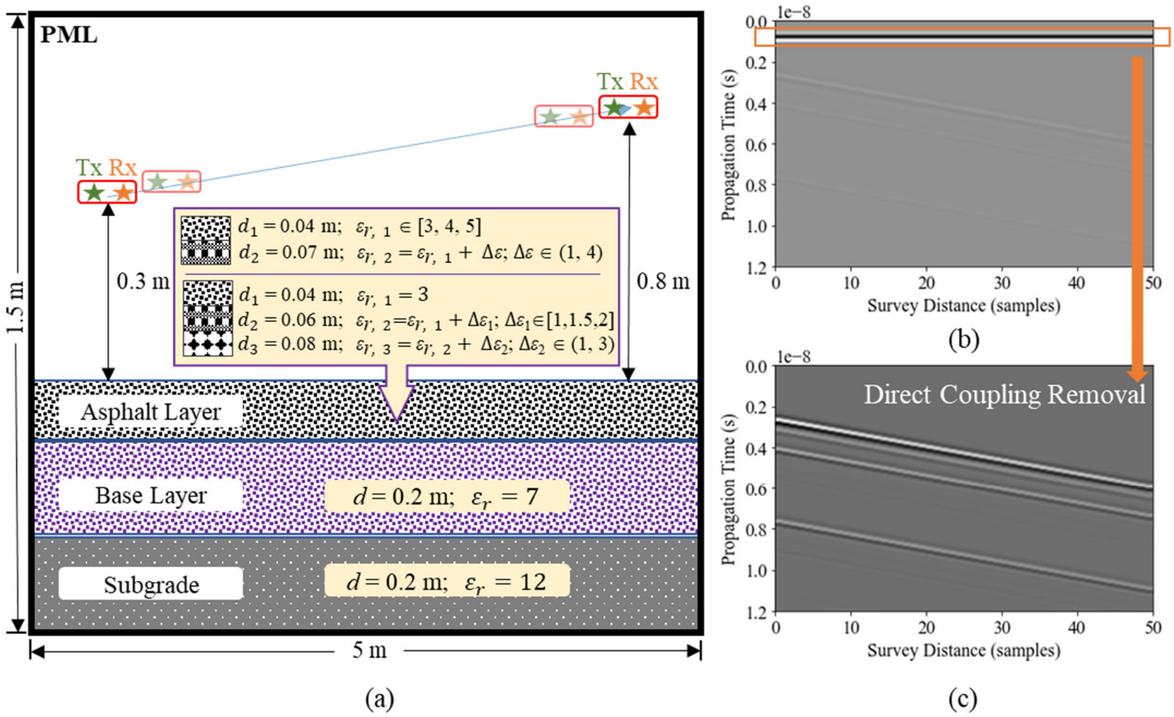

Figure 4.2 Antenna height shifting models and outputs: (a) Geometric configurations and material properties of two-asphalt and three-asphalt layers pavement systems; (b) Raw GPR B-scan; (c) Decoupled GPR B-scan after direct coupling removal

Table 4.1 Dielectric property settings of FDTD models

Model type	Subgroup 1	Subgroup 2	Number
Two-asphalt layer model	$\varepsilon_{r,1}$ varies from 3.0 to 5.0 with an interval of 0.2; $\varepsilon_{r,2} = 4.0$	$\varepsilon_{r,1} \in [3, 4, 5]$; $\varepsilon_{r,2} = \varepsilon_{r,1} + \Delta\varepsilon_{r,12}$; $\Delta\varepsilon_{r,12}$ varies from 1.0 to 4.0 with an interval of 0.2	57 (after eliminating the duplicate models)
Three-asphalt layer model	$\varepsilon_{r,1} = 3$; $\varepsilon_{r,2} \in [4, 4.5, 5]$; $\varepsilon_{r,3} = \varepsilon_{r,2} + \Delta\varepsilon_{r,23}$; $\Delta\varepsilon_{r,23}$ varies from 1.0 to 3.0 with an interval of 0.2	/	31 (after eliminating the duplicate models)
Metal plate calibration model	/	/	1
Validation model	$\varepsilon_{r,1} = 4$; $\varepsilon_{r,2} = 6$;	/	1

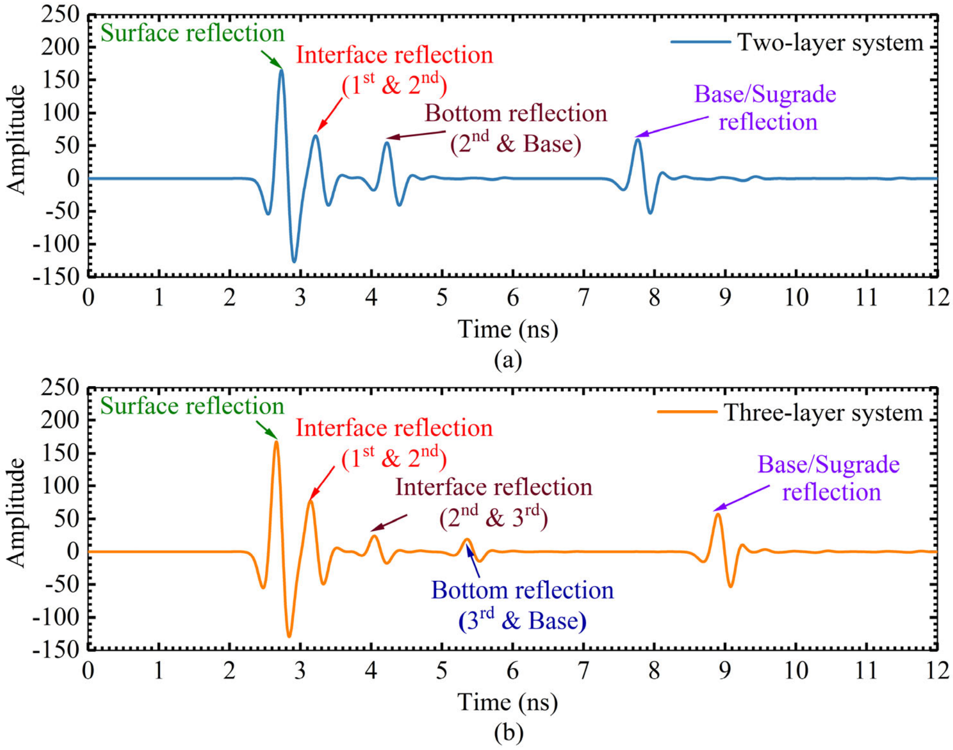

Figure 4.3 Typical GPR signal waveform for two-asphalt layer and three-asphalt layer pavement system: (a) two-asphalt layer system signal; (b) three-asphalt layer system signal

Various antenna height correction models were investigated for surface amplitude, interface amplitude, and bottom amplitude using least squares fitting methods, including the inverted model, power model, and exponential model [97]. Figure 4.4 presents the results of the surface amplitude antenna height relationship in a two-asphalt layer pavement system, and the performance of each model was evaluated using R^2, as summarized in Table 4.2. The surface reflection amplitude decreases as antenna height increases, and the power model best fits this relationship, consistent with previous studies [8]. Figure 4.5 (a), (b), and (c) illustrate the variation of interface amplitude antenna height relationship concerning the dielectric constant contrast between the first and second layer when the first layer dielectric constant equals to 3, 4, and 5, with the corresponding R^2 results presented in Table 4.3. It is noteworthy that the power model no longer exhibit superior correlation performance compared to the inverted and exponential model for all cases. Additionaly, all models struggle to achieve high regression accuracy when the dielectric constant contrast is low. To better capture the interface amplitude antenna height relationship, a 3rd order polynomial model is proposed in this study. The results demonstrate that this model surpasses others by achieving the highest R^2 values in interface reflection amplitude cases, while also showing relatively strong correlation performance with the power model in surface amplitude case. This phenomenon can be further verified by examing the bottom reflection amplitude antenna height relationship, as depicted in Figure 4.6 and summarized in Table 4.3.

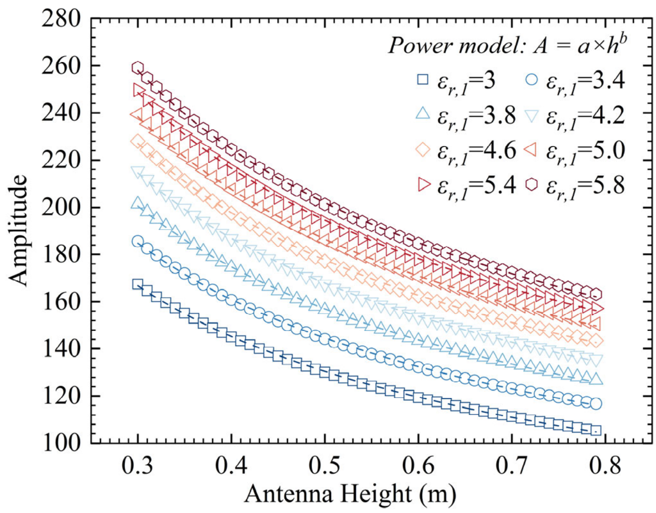

Figure 4.4 Correlation between antenna height and surface reflection amplitude in the two-asphalt layer pavement system

Table 4.2 R^2 for different type of models of surface reflection at different first layer dielectric constants in the two-asphalt layer pavement system

	R^2							
Type $\varepsilon_{r,1}$	3	3.4	3.8	4.2	4.6	5	5.4	5.8
Inverted	0.9927	0.9927	0.9927	0.9926	0.9926	0.9925	0.9925	0.9924
Power	**0.9996**	**0.9996**	**0.9996**	**0.9996**	**0.9996**	**0.9996**	**0.9996**	**0.9996**
Exponential	0.9787	0.9787	0.9786	0.9785	0.9785	0.9784	0.9783	0.9782
Polynomial	0.9995	0.9995	0.9995	0.9995	0.9995	0.9995	0.9995	0.9995

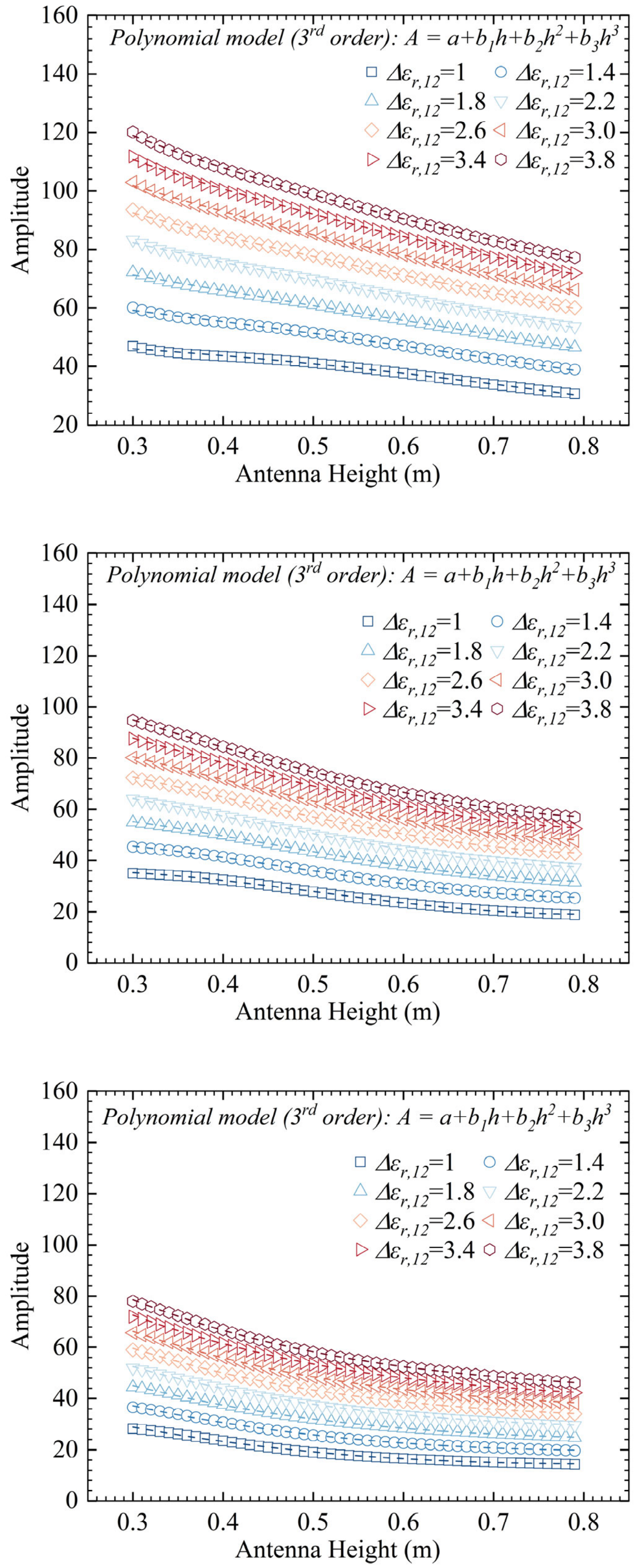

Figure 4.5 Correlation between antenna height and interface reflection amplitude in two-asphalt layer pavement system: (a) $\varepsilon_{r,1} = 3$; (b) $\varepsilon_{r,1} = 4$; (c) $\varepsilon_{r,1} = 5$

Table 4.3 R^2 for different type of models of interface reflection and bottom reflection under different dielectric constant contrasts in the two-asphalt layer pavement system

		R^2							
Location	Type $\Delta\varepsilon_{r,12}$	1	1.4	1.8	2.2	2.6	3	3.4	3.8
interface	Inverted	0.9622	0.9810	0.9888	0.9929	0.9953	0.9967	0.9977	0.9983
reflection	Power	0.9309	0.9577	0.9704	0.9776	0.9822	0.9853	0.9875	0.9891
$\varepsilon_{r,1} = 3$	Exponential	0.9782	0.9919	0.9966	0.9984	0.9990	0.9991	0.9990	0.9988
	Polynomial	**0.9971**	**0.9982**	**0.9987**	**0.9989**	**0.9991**	**0.9992**	**0.9993**	**0.9994**
interface	Inverted	0.9758	0.9875	0.9924	0.9950	0.9965	0.9973	0.9979	0.9982
reflection	Power	0.9634	0.9769	0.9835	0.9874	0.9899	0.9916	0.9929	0.9938
$\varepsilon_{r,1} = 4$	Exponential	0.9907	0.9945	0.9953	0.9952	0.9949	0.9945	0.9941	0.9936
	Polynomial	**0.9990**	**0.9992**	**0.9993**	**0.9995**	**0.9996**	**0.9996**	**0.9997**	**0.9997**
interface	Inverted	0.9895	0.9897	0.9899	0.9901	0.9902	0.9904	0.9904	0.9905
reflection	Power	0.9921	0.9941	0.9953	0.9961	0.9966	0.9969	0.9972	0.9974
$\varepsilon_{r,1} = 5$	Exponential	0.9654	0.9668	0.9682	0.9693	0.9701	0.9708	0.9713	0.9717
	Polynomial	**0.9980**	**0.9988**	**0.9992**	**0.9994**	**0.9995**	**0.9996**	**0.9997**	**0.9997**
	Type $\Delta\varepsilon_{r,23}$	3	2.6	2.2	1.8	1.4	1	0.6	0.2
Bottom	Inverted	0.9940	0.9953	0.9953	0.9949	0.9946	0.9943	0.9942	0.9944
reflection	Power	0.9999	1	1	1	1	1	1	1
$\varepsilon_{r,1} = 3$	Exponential	0.9830	0.9850	0.9850	0.9845	0.9839	0.9834	0.9832	0.9835
	Polynomial	**1**	**1**	**1**	**1**	**1**	**1**	**1**	**1**

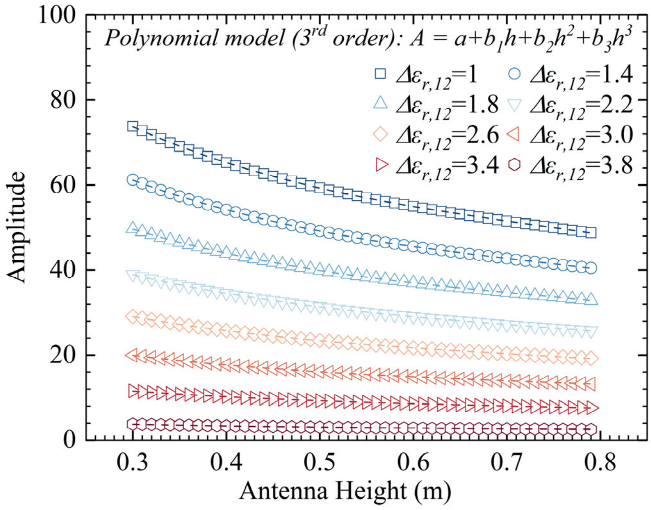

Figure 4.6 Correlation between antenna height and bottom reflection amplitude in two-asphalt layer pavement system

To assess the effectiveness of the proposed polynomial model in multi-asphalt layer scenarios, similar results were extracted from the three-asphalt layer pavement system gprMax model, and the corresponding results are shown in Figures 4.7, 4.8, and 4.9, and Table 4.4. The proposed polynomial model demonstrated stable and superior fitting performance for the interfaces between the first and second asphalt layers. Both the power model and the polynomial model performed well in the second and third asphalt layer interface and the bottom cases. Overall, the polynomial model outperformed the inverted model, power model, and exponential model in accurately estimating reflection amplitudes, particularly for the interfaces between the first and second asphalt layers.

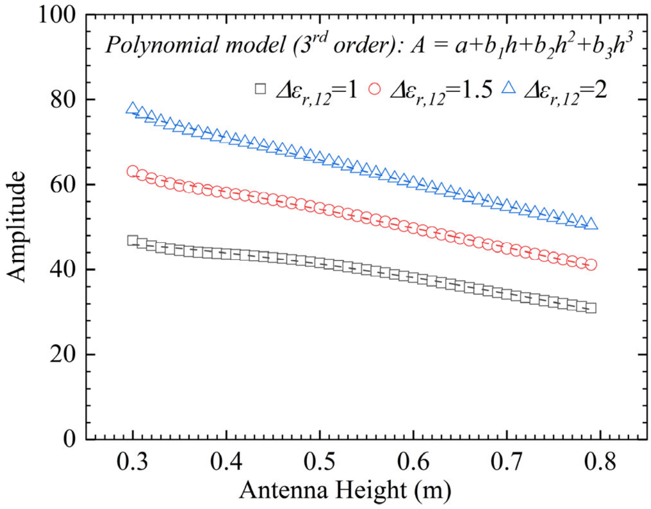

Figure 4.7 Correlation between antenna height and the first interface reflection amplitude in three-asphalt layer pavement system

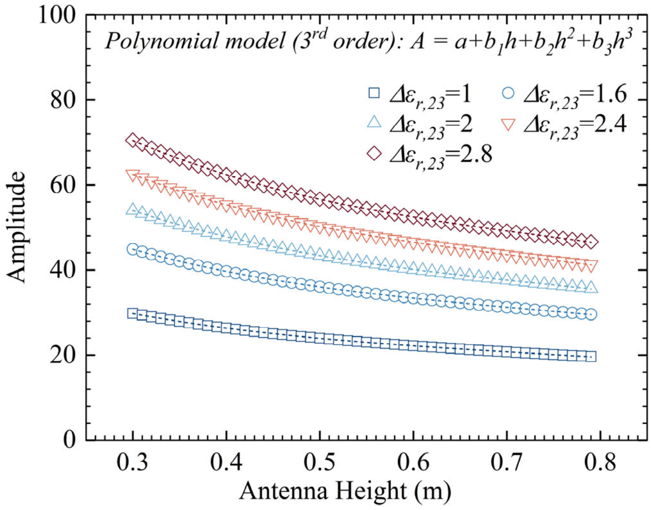

Figure 4.8 Correlation between antenna height and the second interface reflection amplitude in three-asphalt layer pavement system

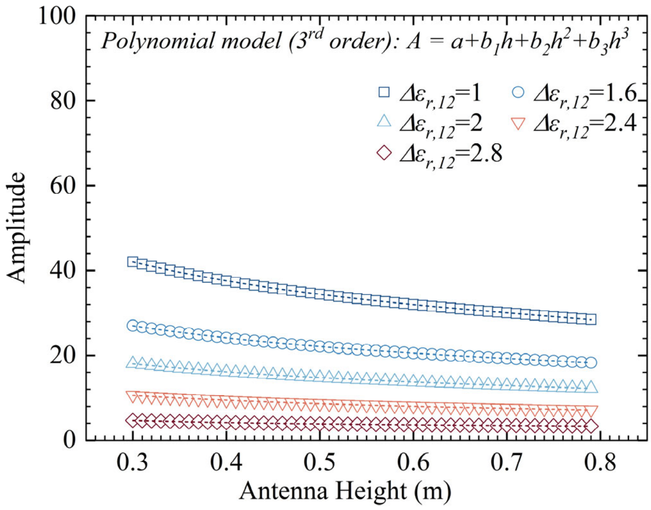

Figure 4.9 Correlation between antenna height and the bottom reflection amplitude in three-asphalt layer pavement system

Table 4.4 R^2 for different type of models of the first interface reflection amplitude, second interface reflection amplitude, and bottom reflection amplitude under different dielectric constant contrast in three-asphalt layer pavement system

			R^2				
Location	Type	$\Delta\varepsilon_{r,12}$	1		1.5		2
First interface reflection	Inverted		0.9517		0.9779		0.9876
	Power		0.9162		0.9530		0.9682
	Exponential		0.9696		0.9898		0.9959
	Polynomial		**0.9965**		**0.9980**		**0.9985**
		$\Delta\varepsilon_{r,23}$	1	1.6	2	2.4	2.8
Second interface reflection	Inverted		0.9952	0.9948	0.9946	0.9945	0.9944
	Power		**1**	**1**	**1**	**1**	**1**
	Exponential		0.9848	0.9841	0.9838	0.9836	0.9835
	Polynomial		**1**	**1**	**1**	**1**	**1**
		$\Delta\varepsilon_{r,34}$	2	1.4	1	0.6	0.2
Bottom reflection	Inverted		0.9845	0.9943	0.9953	0.9954	0.9955
	Power		0.9982	1	1	0.9999	0.9999
	Exponential		0.9719	0.9844	0.9859	0.9860	0.9863
	Polynomial		**1**	**1**	**1**	**1**	**1**

To further explore the influence of central frequency on the antenna height-reflection amplitude relationship, six additional numerical models were created using antennas with different central frequencies for a two-asphalt layer system, with $\varepsilon_{r,1} = 4$ and $\Delta\varepsilon_{r,12} = 2$. The selected central frequency included commonly used frequencies of commercial air-coupled GPR, including 2 GHz, 1.5 GHz, 1.2 GHz, and 1 GHz. Additionally, two lower frequencies, 900 MHz, and 700

MHz, were included to assess the lower limit of antenna frequency applicable to the proposed HC-SR method, although they are primarily used with ground-coupled antennas.

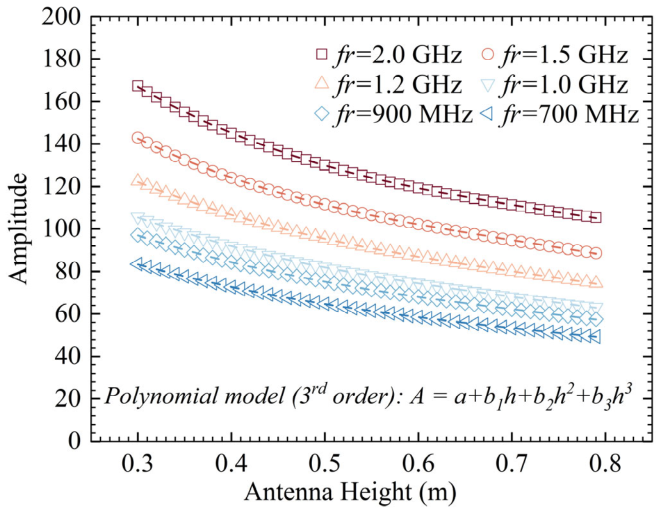

(a)

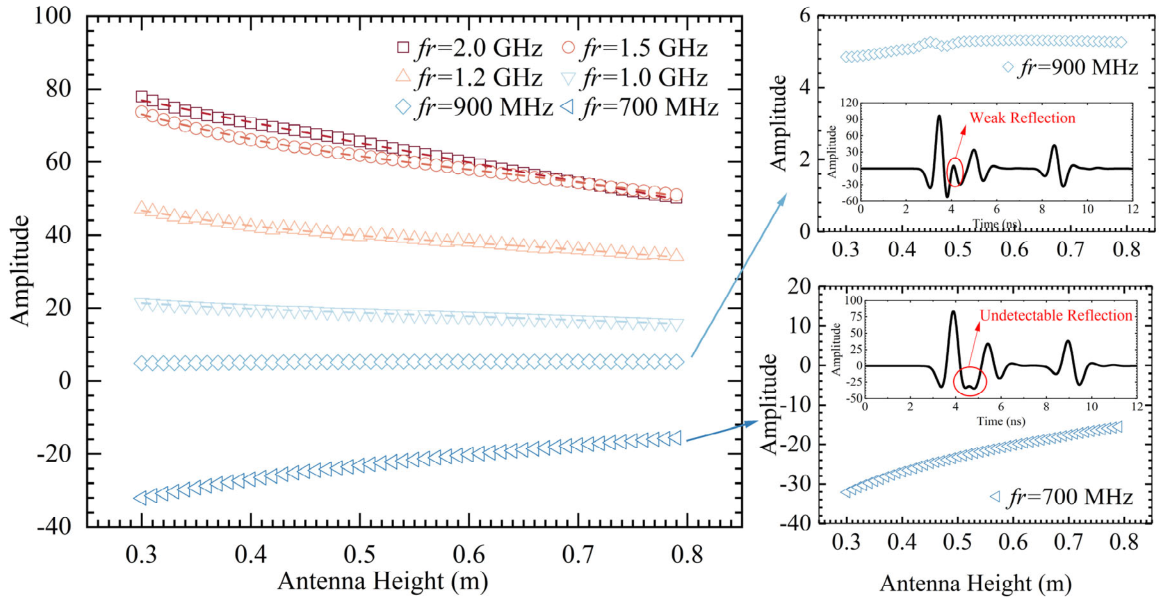

(b)

Figure 4.10 Correlation between antenna height and interface reflection amplitude in two-asphalt layer pavement system with different antenna central frequencies: (a) surface reflection case; (b) interface reflection case

As depicted in Figure 4.10 (a), the correlation between antenna height and surface reflection amplitude still followed the 3rd order polynomial model. At a given antenna height, higher central frequencies resulted in higher surface reflection amplitudes. The same trend applies to the interface reflection case, as seen in Figure 4.10 (b). However, due to lower depth resolution, the 900 MHz and 700 MHz antennas exhibited weaker or undetectable interface reflections. The interface reflection could be easily camouflaged by white noise, indicating the inapplicability of using antennas with a central frequency lower than 1 GHz for multi-asphalt layer thickness determination.

The proposed polynomial model can be described in the form of the following equation:

$$\begin{cases} A_i' = a_i + b_i h^3 + c_i h^2 + d_i h = g_i(h) \\ A_{r,i} = a_i + b_i h_r^3 + c_i h_r^2 + d_i h_r = g_i(h_r) \end{cases} \quad i = 0, 1, 2 \ldots n \qquad (4-12)$$

Where A_i' is the revised reflection amplitude of the interface between the i^{th} and $(i+1)^{th}$ layer. Especially, when i = 0 and n, corresponding A_0' and A_n' represents the revised surface and the bottom reflection amplitude of the whole asphalt layer, respectively; a_i, b_i, c_i, and d_i are fitting parameters of the polynomial model; $A_{r,i}$ is the reflection amplitudes between the i^{th} and $(i+1)^{th}$ layers at the reference antenna height, which is the height when the incident wave amplitude was collected using a copper plate as well as conducting the field survey, an unchanged parameter for a single GPR survey; and $g_i(h)$ and $g_i(h_r)$ are the polynomial expression of the reflection amplitude at the actual antenna height h and the reference antenna height h_r, respectively. By rearranging Equation (4-12), a succinct form could be achieved as shown in the following equation:

$$\begin{cases} A_0' = A_{r,0}\dfrac{g_0(h)}{g_0(h_r)} \\ A_1' = A_{r,1}\dfrac{g_1(h)}{g_1(h_r)} \\ \quad\cdots \\ A_n' = A_{r,n}\dfrac{g_n(h)}{g_n(h_r)} \end{cases} \xrightarrow{\frac{g_i(h)}{g_i(h_r)} = corr_i} \begin{cases} A_0' = A_{r,0}corr_0 \\ A_1' = A_{r,1}corr_1 \\ \quad\cdots \\ A_n' = A_{r,n}corr_n \end{cases}$$

$$\xrightarrow[A_{r,i} \to \frac{A_{r,i}}{A_{inc,h}}]{A_i' \to \frac{A_i'}{A_{inc,h}}} \begin{cases} \dfrac{A_0'}{A_{inc,h}} = \dfrac{A_{r,0}}{A_{inc,h}} corr_0 \\ \dfrac{A_1'}{A_{inc,h}} = \dfrac{A_{r,1}}{A_{inc,h}} corr_1 \\ \quad\cdots \\ \dfrac{A_n'}{A_{inc,h}} = \dfrac{A_{r,n}}{A_{inc,h}} corr_n \end{cases} \qquad (4-13)$$

where $corr_i = g_i(h)/g_i(h_r)$, defined as the coefficient of anntena vibration, which reflects the deviation degree of reflection amplitude that is affected by the antenan vibration, and $A_{inc,h}$ is the reflection amplitude of the incident EM wave at the actual antenna height collected using a copper plate, which is also governed by the polynomial model: $A_{inc,h} = j(h) = a_{inc,i} + b_{inc,i}h^3 + c_{inc,i}h^2 + d_{inc,i}h$. Noted that this value should also be revised during field applications. However, existing literatures, as well as the reported projects rarely consider it, leading to inaccurate antenna height correction. By substituting Equation (4-13) into Equation (4-5) - (4-8), the corrected dielectric constant of the multi-layer pavement system considering the antenna height effect could be obtained, as well as the corrected reflection coefficient.

$$\varepsilon'_{r,1} = \left(\frac{1 + \frac{A_{r,0}}{A_{inc,h}} corr_0}{1 - \frac{A_{r,0}}{A_{inc,h}} corr_0} \right)^2 \tag{4-14}$$

$$\varepsilon'_{r,2} = \varepsilon'_{r,1} \left(\frac{1 - \left(\frac{A_{r,0}}{A_{inc,h}}\right)^2 corr_0^2 + \frac{A_{r,1}}{A_{inc,h}} corr_1}{1 - \left(\frac{A_{r,0}}{A_{inc,h}}\right)^2 corr_0^2 - \frac{A_{r,1}}{A_{inc,h}} corr_1} \right)^2 \tag{4-15}$$

$$\varepsilon'_{r,3} = \varepsilon'_{r,2} \left(\frac{1 - \left(\frac{A_{r,0}}{A_{inc,h}}\right)^2 corr_0^2 - \gamma'_1 \frac{A_{r,1}}{A_{inc,h}} corr_1 + \frac{A_{r,2}}{A_{inc,h}} corr_2}{1 - \left(\frac{A_{r,0}}{A_{inc,h}}\right)^2 corr_0^2 - \gamma'_1 \frac{A_{r,1}}{A_{inc,h}} corr_1 - \frac{A_{r,2}}{A_{inc,h}} corr_2} \right)^2 \tag{4-16}$$

$$\varepsilon'_{r,n} = \varepsilon'_{r,n-1} \left(\frac{1 - \left(\frac{A_{r,0}}{A_{inc,h}}\right)^2 corr_0^2 - \sum_{i=1}^{n-2} \gamma'_i \frac{A_i}{A_{inc}} corr_i + \frac{A_{r,n-1}}{A_{inc,h}} corr_{n-1}}{1 - \left(\frac{A_{r,0}}{A_{inc,h}}\right)^2 corr_0^2 - \sum_{i=1}^{n-2} \gamma'_i \frac{A_i}{A_{inc}} corr_i - \frac{A_{r,n-1}}{A_{inc,h}} corr_{n-1}} \right)^2 \tag{4-17}$$

$$\gamma'_i = \frac{\sqrt{\varepsilon'_{r,i+1}} - \sqrt{\varepsilon'_{r,i}}}{\sqrt{\varepsilon'_{r,i+1}} + \sqrt{\varepsilon'_{r,i}}} \tag{4-18}$$

Equations (4-14) - (4-18) presented above constitute the proposed height-correction surface reflection (HC-SR) method. In contrast to the typical surface reflection method, the proposed method replaces amplitude values from GPR raw data with back-calculated values obtained from the polynomial antenna height-amplitude relationship. The key contribution lies in calculating the antenna height using the two-way travel time between direct wave and the surface reflection. This time-of-flight is sorely affected by the speed of light in air, and the inherent dielectric constant of air, reducing the influence of antenna vibration (as indicated in Equation (4-1)) The performance of the HC-SR method can be evaluated using the following equations:

$$\Delta\varepsilon_{r,i} = \varepsilon'_{r,i} - \varepsilon_{r,i} \qquad (4-19)$$

$$\Delta\varepsilon_{r,i}^{(inherent)} = \varepsilon'_{r,i} - \varepsilon_{r,i}^{(ground\ truth)} \qquad (4-20)$$

where $\Delta\varepsilon_{r,i}$ is the achieved dielectric constant improvement of the proposed method; $\Delta\varepsilon_{r,i}^{(inherent)}$ is the inherent estimation error of the surface reflection method itself, which might be caused by the accumulative error during the least squares fitting, and the resolution limitation of the adopted GPR system; and $\varepsilon_{r,i}^{(ground\ truth)}$ is the ground truth dielectric constant value, which could be acquired by the input in the simulation or on-site cores in field applications. The dielectric constant estimation error of the first and second asphalt layers before and after antenna height correction are displayed in Figure 4.11 and 4.12, respectively, with the reference antenna height of 0.55m. From Figure 4.11, it can be observed that the dielectric constant estimation error increases as the actual antenna height gradually deviates from the reference antenna height. This error also increases with higher dielectric constants of the first asphalt layer. Within the typical range of dielectric constants for the in-service asphalt pavement, the maximum dielectric constant estimation error of the first asphalt layer could exceed 6 if the antenna height effect is not considered using the SR method. The siguation is even worse for the estimation of the second layer's dielectric constant, as depicted in Figure 4.12, where the maximum error could exceed 8. This phenomenon may be attributed to the cumulative errors that arise due to the top-down estimation manner of each asphalt layer's dielectric constant, as described in Equation (4-14) - (4-17).

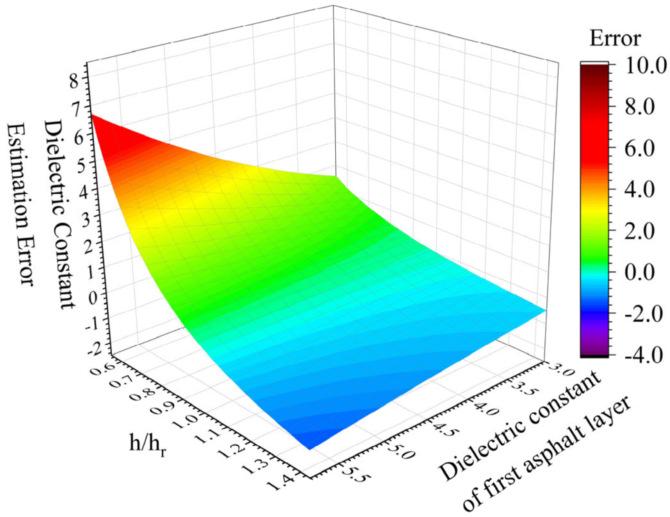

Figure 4.11 Dielectric constant estimation error of the first asphalt layer before and after multi-asphalt layer antenna height correction at h_r = 0.55m

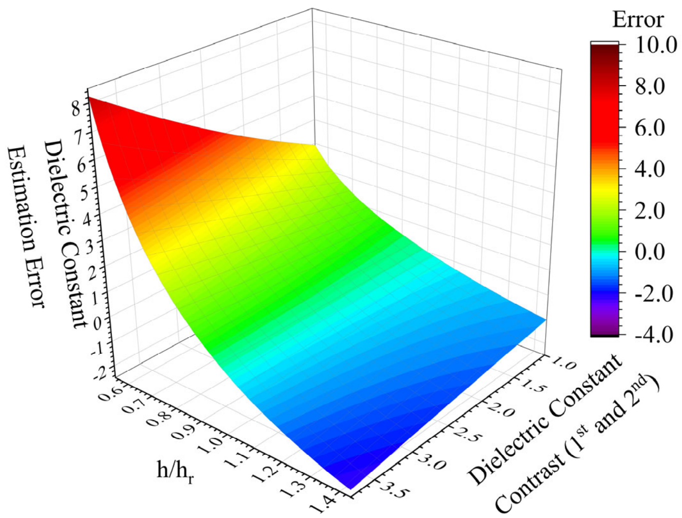

Figure 4.12 Dielectric constant estimation error of the second asphalt layer before and after multi-asphalt layer antenna height correction at h_r = 0.55m

In addition to the antenna height shifting effect, the SR method itself can introduce an inherent error. This error may arise from the basic assumption of homogeneity in the layered medium and the neglect of EM wave attenuation along the depth. Figure 4.13 presents the estimation results of dielectric constant and the back-calculated layer thickness after antenna height effect correction when $\varepsilon_{r,1}$ = 3 and $\Delta\varepsilon_{r,12}$ = 3. It can be observed that the dielectric constant estimation of the first layer closely matches the ground truth value, resulting in a contiguous thickness estimation result. However, the estimated dielectric constant exhibits a hyperbolic offset as the antenna height increases regarding the second layer situation. This inherent error isrelatively smaller than the errors caused by antenna height changes, and the back-calculated thickness still performs well with an offset of less than 3 mm. Such a level of thickness estimation error is acceptable in field applications since it is close to the GPR depth resolution at this central frequency [98]. To minimize this error, a practical strategy is to set the reference antenna height at the lower limit of the recommended antenna installation height by the GPR vendor when designing the system configuration.

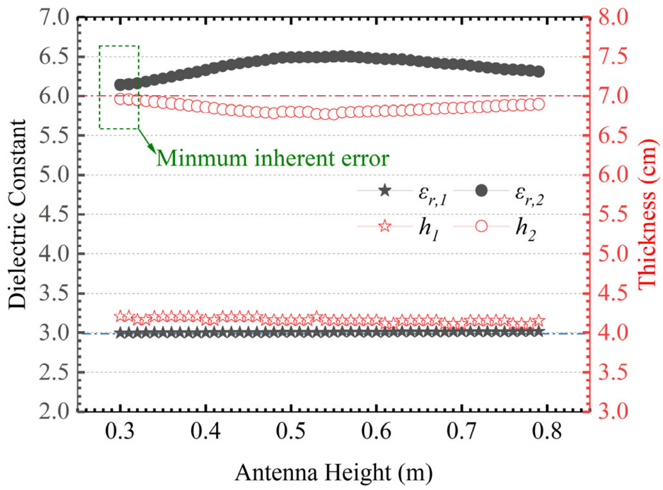

Figure 4.13 Inherent dielectric constant and thickness estimation of the first and second asphalt layer using HC-SR method at $\varepsilon_{r,1} = 3$ and $\Delta\varepsilon_{r,12} = 3$

4.2.2 Validation Model

A numerical model containing two asphalt layers was built to validate the performance of the built antenna height and reflection amplitude correlation model in a multi-asphalt layer pavement system. The geometry configuration remained the same as the previous models, with the only difference being that the thickness of the first asphalt layer was randomly vibrated between 0.4 ± 0.02 m. The antenna height was set to fluctuate within 0.5 ± 0.02 m above the asphalt pavement surface, representing the most unfavourable condition for using the proposed HC-SR method. The spatial sampling rate was set to 250 traces/m, resulting in an adjacent trace distance of 0.004 m. 2545 samples were generated in the single A-Scan signal with a time duration of 12 ns. Each sample change correspond to a time interval alteration of 12/2545 ns. The number of 2545 was determined based on the model's simulated time duration and step size. The FDTD simulation in gprMax executes the EM wave propagation in the time mode by central-difference spatial and temporal derivatives. Given the simulated time duration and minimum derivative step size in gprMax, the simulation steps can be obtained automatically, which is 2545.The dielectric constant of the first and second asphalt layers were set to 4 and 6, respectively, while those of the base layer and subgrade remained unchanged from the previous models. Figure 4.14 (a) displays the synthesized B-scan radargram, which reflects the actual antenna height shifting effect in field surveys. The antenna height was back-calculated using the TWTT between the direct coupling signal and the surface reflection signal, as described in Equation (4-1). The dielectric constant back-calculating results before and after the multi-layer antenna height shifting correction are shown in Figure 4.14 (b), and the corresponding estimation error results are presented in Figure 4.14 (c).

It can be observed that without considering the antenna height shifting effect, the dielectric constant profile fluctuates due to low-frequency, large-amplitude vibration caused by changing pavement topography or surface unevenness. The true dielectric constant value will be camouflaged either way and this phenomenon becomes more pronounced when determining the thickness of the second asphalt layer. Figure 4.14 (b) demonstrates that the dielectric constant estimation profile can be significantly smoothed for both asphalt layers after applying the HC-SR method. The reduced errors in both layers confirm the effectiveness of the proposed method. It should be noted that there was an averaged dielectric constant estimation error (around 0.27 mm in this case) in the second layer situation. This error is caused by the inherent calculation error associated with the surface reflection method itself, as previously discussed. In this case, the inherent error is less than 4%, indicating an acceptable estimation compared to uncorrected values (up to 18%).

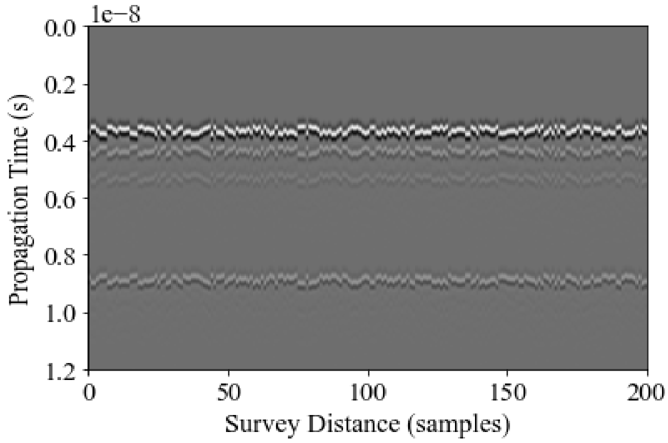

(a)

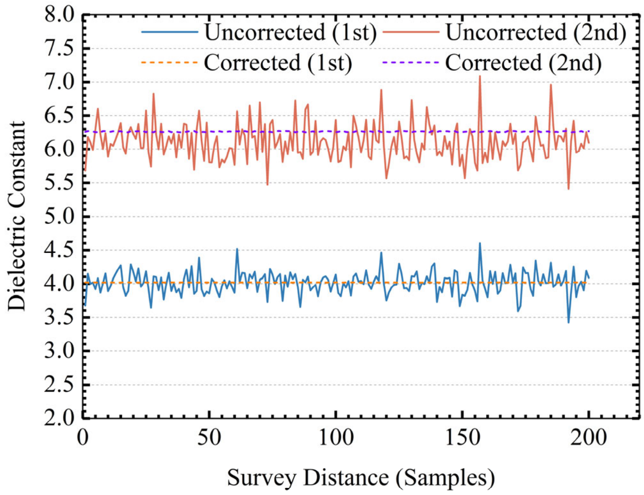

(b)

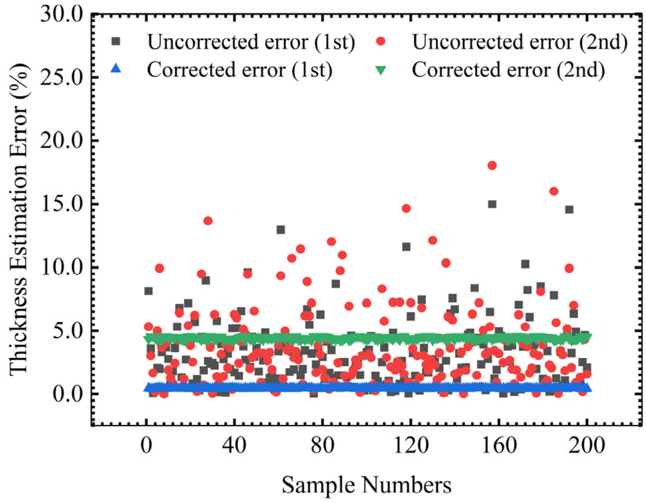

(c)

Figure 4.14 Validation model outcomes: (a) B-scan radargram; (b) Dielectric constant back-calculating results before and after applying multi-layer antenna height correction method; (c) Inherent estimation error of HC-SR method

4.3 Field Validation and Discussion

4.3.1 Test Setting and Procedure

Case I

Field tests were conducted on Yuk Choi Road, situated on the campus of the Hong Kong Polytechnic University, Hong Kong SAR. The road has been in service for over 40 years and has undergone multiple localized maintenance and rehabilitation operations, resulting in an uneven pavement surface. Due to the extended service period, the original pavement design information was unavailable before GPR surveys. A 15 m road section was selected for field tests, and a 2 GHz air-coupled GPR system was employed. The GPR system was mounted on a customized cart, and the antenna was deliberately subjected to vibrations by loosening the fixing nail connecting it to the cart from the wooden frame. This ensured a random bouncing action during the surveys. Alternatively, for van-mounted GPR systems, the operator could stand on the van and sway to achieve the bouncing effect. The continuous survey and the bouncing tests are illustrated in Figure 4.15 (a) and (b), respectively. The survey process for each section involved stationary bumping tests on the pavement surface, bumping tests with a metal plate beneath the antenna, and continuous surveys of the entire section. Following the GPR tests, six cores were randomly selected and drilled to provid ground truth value for layer thickness information.

Figure 4.15 Field GPR tests: (a) Continuous survey; (b) Bouncing tests

Case II

Another field test was conducted at a circular-shaped full-scale accelerated pavement testing facility in Hong Kong, SAR. The pavement section under investigation consisted of a two-asphalt pavement system constructed with Mastic asphalt (MA) mixture and stone mastic asphalt (SMA) mixture. The pavement testbed was divided into four sections with different mix design and material property combinations, but each section underwent an equal number of wheel loadings. GPR data was collected perpendicular to the traffic lanes, using the same equipment, setup, and data acquisition procedure as in Case I. One core sample was drilled in each section, resulting in a total of four cores, as depicted in Figure 4.16.

Figure 4.16 Field GPR tests of case II: (a) GPR survey; (b) drilled core samples

4.3.2 Test Results

Case I

Figure 4.17 (a)-(d) show the calibration results of antenna height-reflection amplitude correlation from the on-site bouncing test for surface, interface, bottom, copper plate cases, respectively. The correlation models were evaluated based on their R^2 values, as presented in Table 4.5. The polynomial model consistently outperformed the other models, achieving the highest R^2 in all four cases. For surface, bottom, and copper reflection, all models except the inverted model provided a good fit to the field data, consistent with previous studies findings. The inverted model did not mathematically converge in these cases. In the case of interface and bottom reflections, particularly the interface case, the proposed polynomial model demonstrated superior performance compared to the other models.These observations align with the simulation results. Despite the dispersive nature of the data in the interface case, an R^2 of 98.13 was achieved using the proposed polynomial model, indicating robust correction performance. The necessity of the proposed model was further emphasized in the determination of sublayer thickness, as a more accurately adjusted interface reflection amplitude leads to more precise thickness estimation when utilizing the SR method. The 3rd-order polynomial relationship for each reflection case are provided in Figure 4.17 (a)-(d). These equations were used to adjust the continuous GPR survey data and correct the multi-layer thickness determination results.

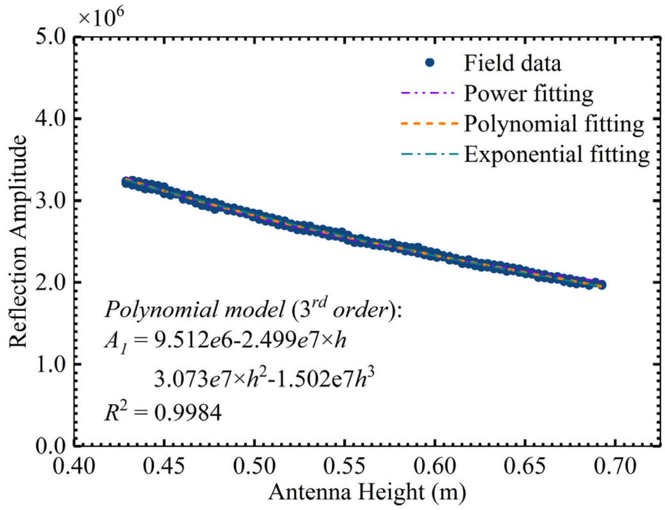

(a)

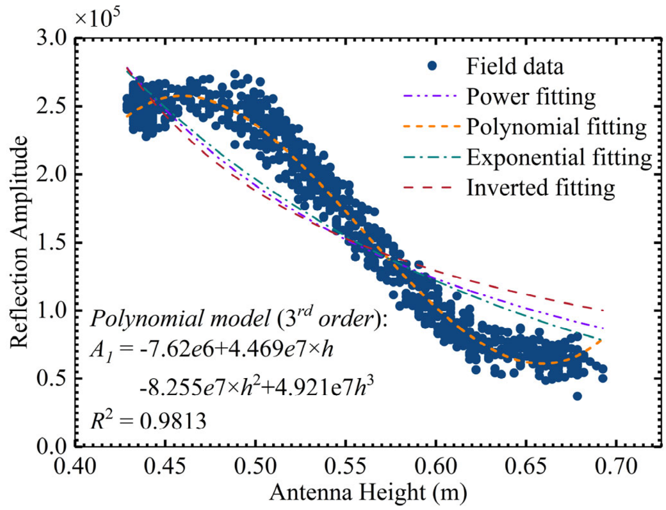

(b)

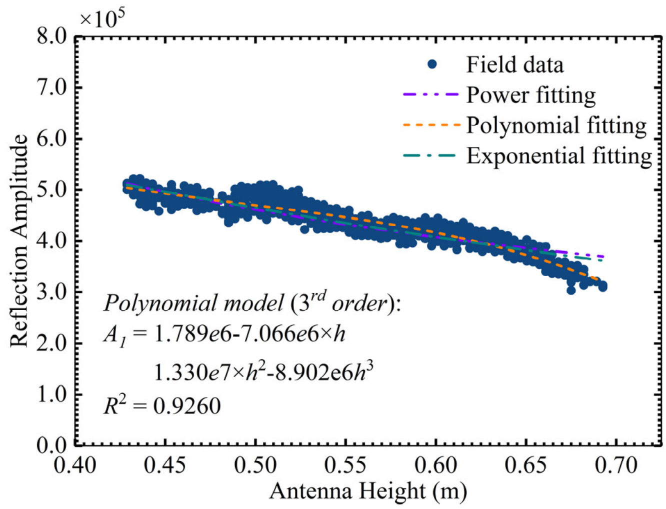

(c)

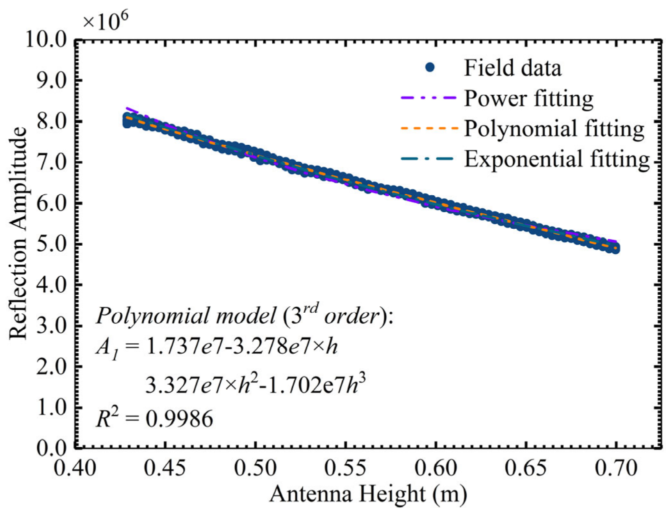

(d)

Figure 4.17 Correlation between antenna height and reflection amplitude from field collected data: (a) surface amplitude; (b) interface (1st and 2nd) amplitude; (c) bottom amplitude; (d) incident amplitude

Table 4.5 R^2 for different type of models for surface/interface/bottom/copper reflection amplitude

Type A_i	R^2			
	Surface (A_0)	Interface (A_1)	Bottom (A_2)	Copper (A_{inc})
Inverted	-	0.8041	-	-
Power	0.9967	0.8428	0.8655	0.9884
Exponential	0.9982	0.8715	0.8877	0.9970
Polynomial	**0.9984**	**0.9813**	**0.9260**	**0.9986**

The raw GPR B-scan of the selected section from the survey road is presented in Figure 4.18. Reflections from two asphalt layers can be observed, and the presence of antenna height vibrations is noticeable. Signals beneath the asphalt layers exhibit ripple characteristics, possibly indicating an uneven base layer intruded by paralleled utility pipes. However, this region falls beyond the scope of current study and will not be further analyzed. Figure 4.19 shows the estimated dielectric constant profiles using the regular SR method and the proposed HC-SR method. Prior to the antenna height shifting correction, the dielectric constant values of both the first and second asphalt layers fluctuated as the GPR moved along the road. This pattern was particularly pronounced in the second asphalt layer dielectric constant esitmation, which varied dynamically from 4.1 to 10.2. This phenomenon deviates from expectations and highlights the erroneous back-calculated dielectric constant as a primary source of thickness estimation errors. Although the dielectric constant of an in-service asphalt pavement may exhibit a gradient change along the depth due to aging effects, it should not demonstrate significant horizontal variation after final compaction until the end of its service life. Utilizing such raw dielectric constant profile estimated from the SR method could introduce further errors in the thickness profile. After applying the proposed HC-SR method, the dielectric constant of the first and second asphalt layers were smoothed and reached values of 5.655 and 6.361, respectively. TWTT profiles were obtained using matched filter method. Then, the thickness of each asphalt layer was calculated using SR and HC-SR methods, as shown in Figure 4.20. Some sharp variating regions of the thickness profiles for both layers that were visibly seen got smoothed after considering antenna height shifting effect. This shows the superiority of the proposed HC-SR method in terms of promoting thickness determination accuracy.

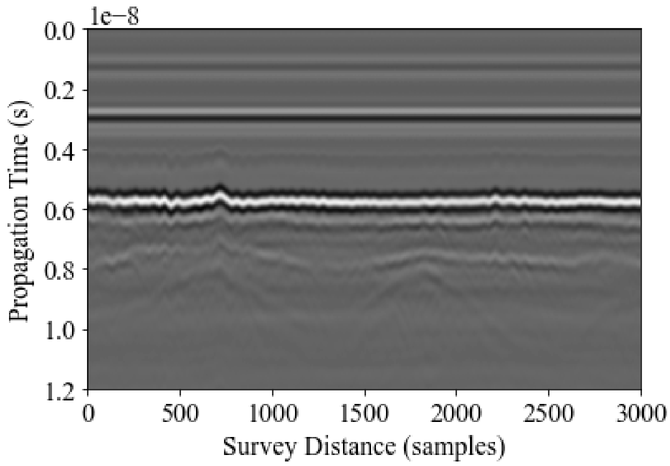

Figure 4.18 B-scan radargram of selected pavement section of the surveyed road

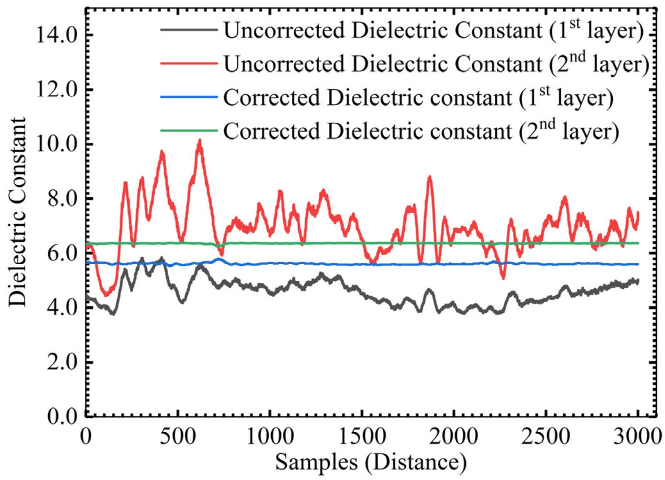

Figure 4.19 Dielectric constant estimation results of the first and second asphalt layer before and after using the multi-layer height correction method

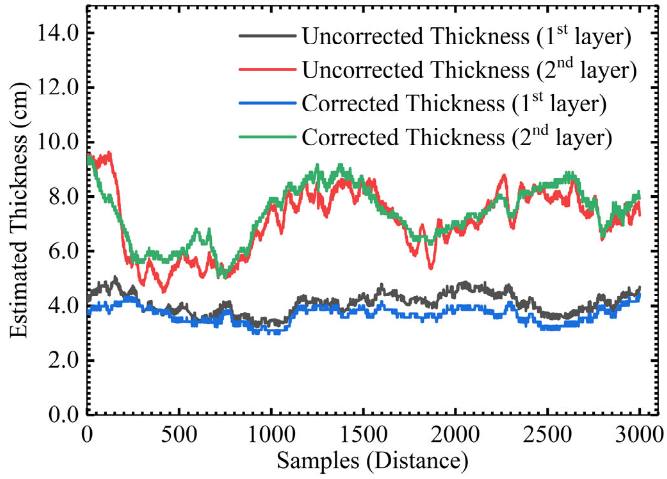

Figure 4.20 Thickness estimation results of the first and second asphalt layer before and after using the multi-layer height correction method

Six core samples were randomly drilled at different locations along the surveyed section with the thickness of each sub-layer being measured, as depicted in Figure 4.21 (a). Figure 4.21 (b), (c), and (d), show the uncorrected, corrected, and ground truth thickness results of first layer, second layer, and the total asphalt layer, respectively. It is evident that the thickness estimation performance without antenna height correction is inadequate, with average error of 20.7%, 28.2%, and 24.2% for the first, second, and total asphalt layer thickness, respectively. After applying the HC-SR method, the average errors reduced to 7.4%, 8.3%, and 6.8% for the respective layers, highlighting the necessity of antenna height correction. Outliers, such as core 3 and core 5 in the first layer case, and core 6 in the second layer case, had a significant impact on the achieved improvement. After removing these outliers, the estimation errors reduced to 1.5% and 3.9% for the first and second layer thickness estimation, respectively. Overall, compared to the traditional SR method, the average estimation errors improved by 13.3%, 19.9%, and 17.4% for the first, second, and total asphalt layer thickness, respectively. The relative layer thickness estimation error using different height correction models are illustrated in Figure 4.22 (a), (b), and (c). The proposed model slightly outperformed the others in the second asphalt thickness prediction, but overall, all three height correction models yielded similar prediction results.

(a)

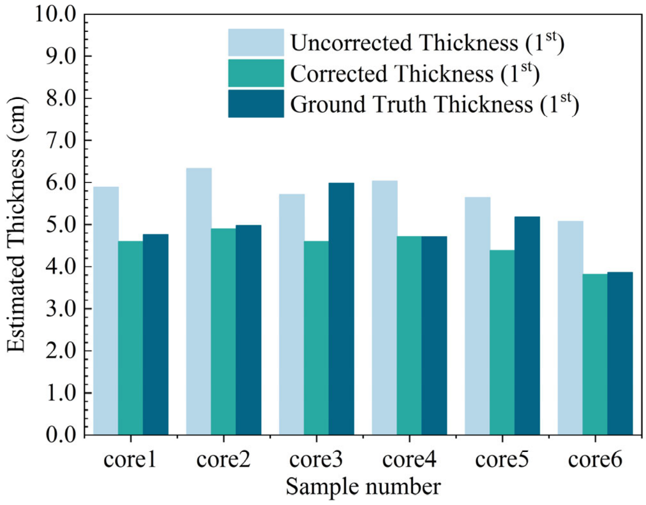
Uncorrected Thickness (1st)
Corrected Thickness (1st)
Ground Truth Thickness (1st)
Estimated Thickness (cm)
10.0
9.0
8.0
7.0
6.0
5.0
4.0
3.0
2.0
1.0
0.0
core1
core2
core3
core4
core5
core6
Sample number

(b)

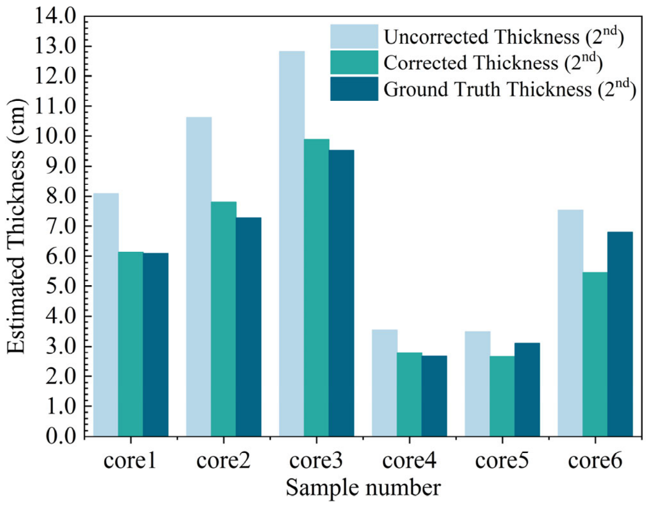
Uncorrected Thickness (2nd)
Corrected Thickness (2nd)
Ground Truth Thickness (2nd)
Estimated Thickness (cm)
14.0
13.0
12.0
11.0
10.0
9.0
8.0
7.0
6.0
5.0
4.0
3.0
2.0
1.0
0.0
core1
core2
core3
core4
core5
core6
Sample number

(c)

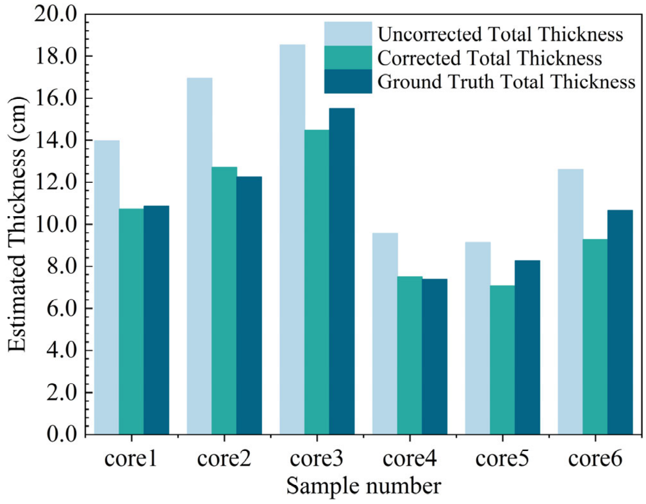

(d)

Figure 4.21 Validation results of multi-layer height correction method using ground truth core sample data in Case I: (a) drilled on-site core samples; (b) first layer thickness results; (c) second layer thickness results; (d) Total thickness results

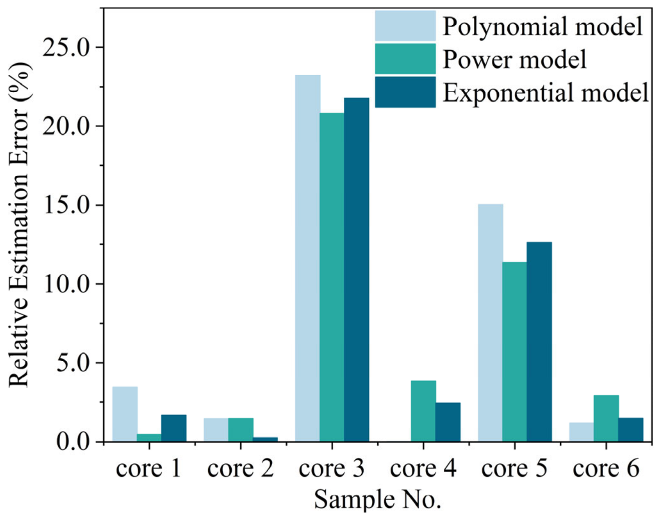

(a)

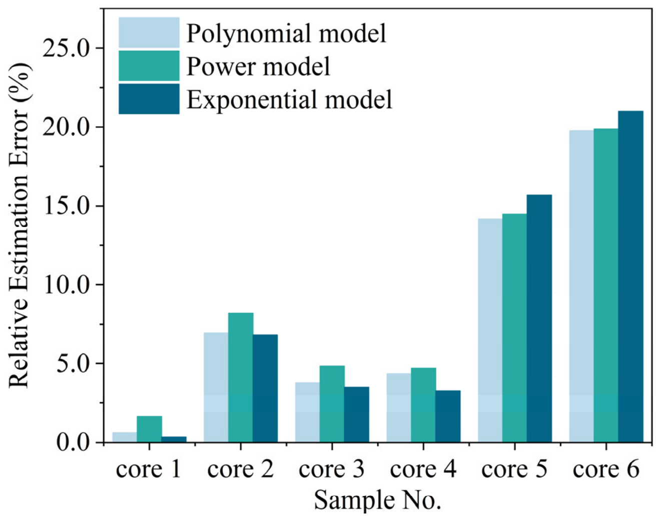

(b)

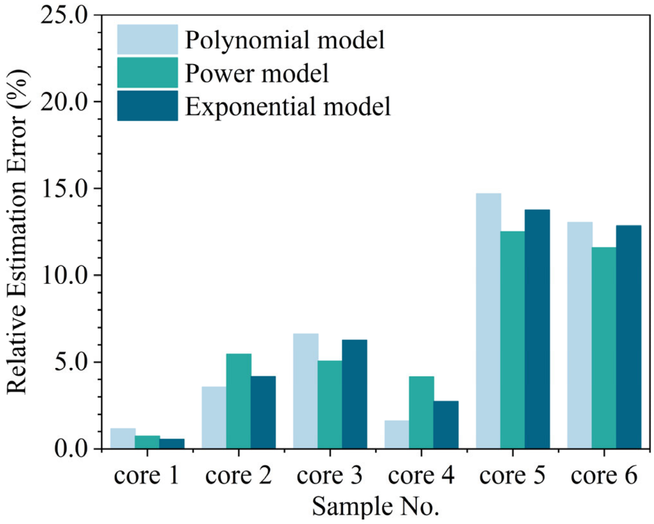

(c)

Figure 4.22 Relative thickness estimation error using different height correction models in case I: (a) first asphalt layer; (b) second asphalt layer; (c) total asphalt layer

Case II

Figure 4.23 presents the thickness prediction results for the two-asphalt layer using the typical SR and proposed HC-SR method. With the typical SR method, the average thickness prediction errors for the first layer, second layer, and total asphalt layer were 6.30%, 22.5%, and 8.88%, respectively, compared to the ground truth thickness values. After applying the proposed HC-SR method, these errors reduced to 2.01%, 3.56%, and 1.57%, respectively, resulting in an average prediction accuracy increase of 4.29%, 18.9%, and 7.29%. The superiority of the HC-SR was further validated, especially in predicting the second layer thickness involving interface reflection. The relative layer thickness estimation error using different height correction models are shown in Figure 4.24 (a), (b), and (c). The proposed polynomial model outperformed the other two height correction models, especially for the second asphalt layer thickness prediction. An exception occurred with the core 2 data in Figure 4.24 (c), where the power model performed the best due to its overestimation of the first layer thickness and underestimation of the second layer thickness. This phenomenon highlights the superiority of the proposed polynomial model when predicting the thickness of each asphalt layer separately.

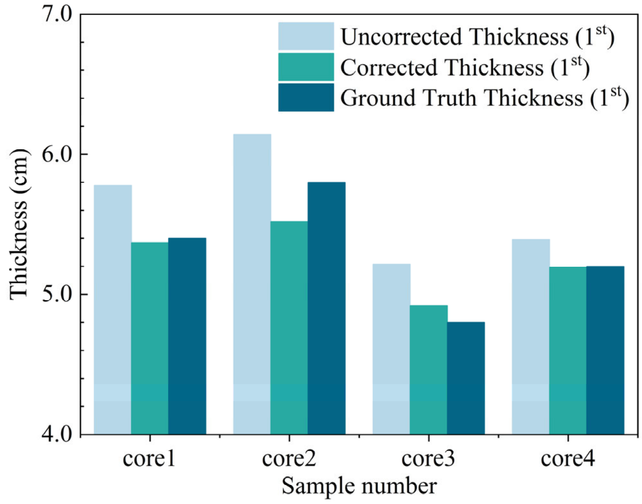

(a)

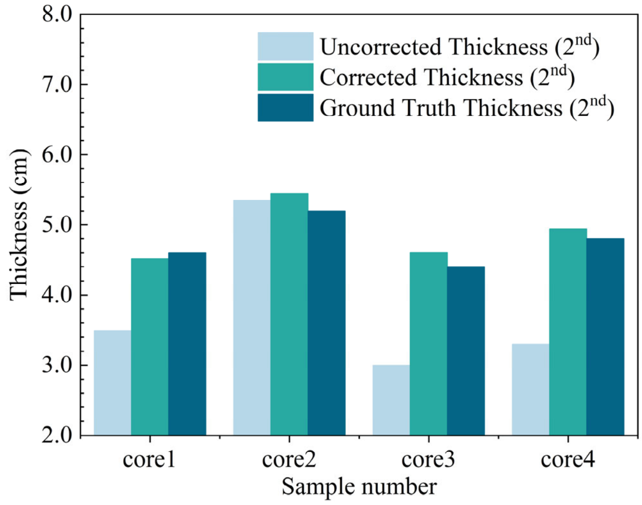

(b)

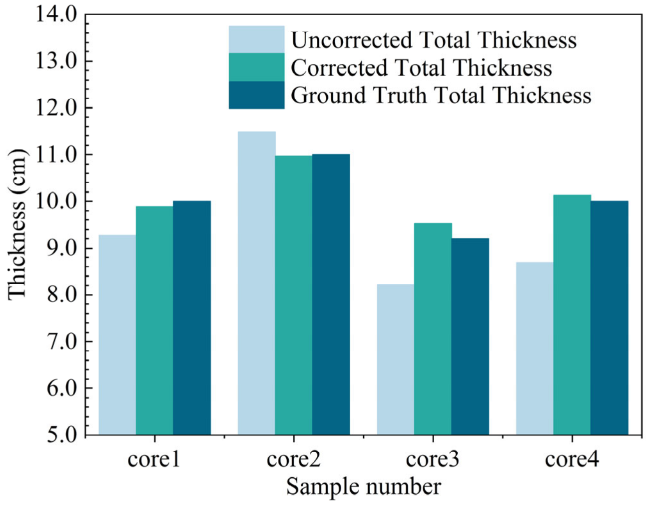

(c)

Figure 4.23 Validation results of multi-layer height correction method using ground truth core sample data in Case II: (a) first layer thickness results; (b) second layer thickness results; (c) Total thickness results

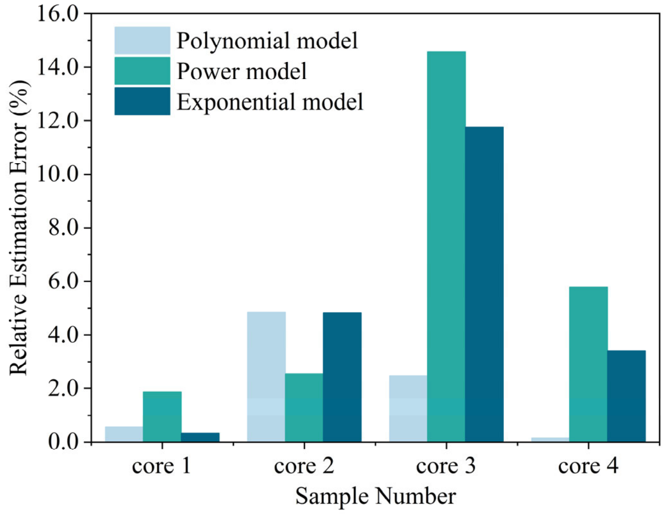

(a)

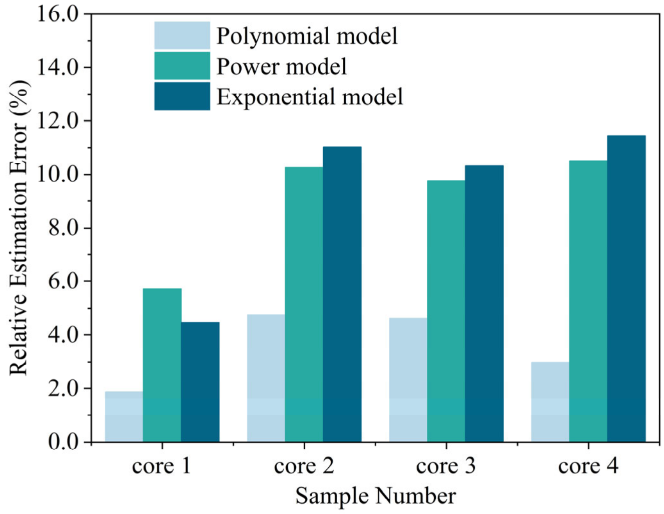

(b)

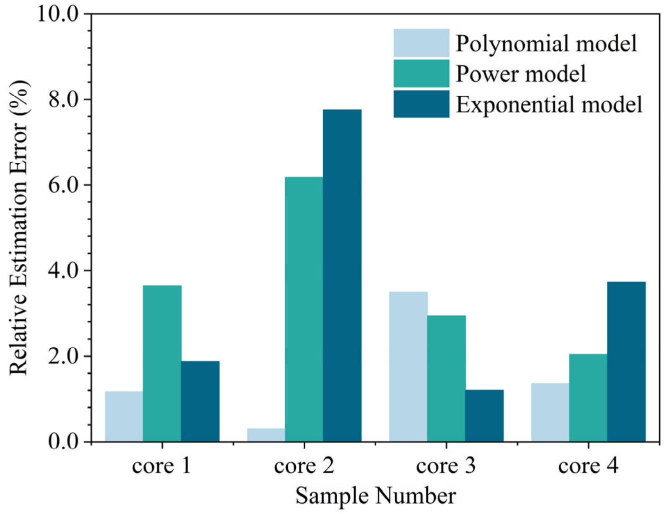

(c)

Figure 4.24 Relative thickness estimation error using different height correction models in case II: (a) first asphalt layer; (b) second asphalt layer; (c) total asphalt layer

Figure 4.25 shows the recommanded workflow for applying the proposed HC-SR method for asphalt pavement thickness determination. The practical benefit of this method lies in the improved subsurface layer thickness detecting accuracy, without significantly increasing the time and labor consumptions of the GPR operators and the constructors. For instance, conducting two bouncing tests (towards the pavement and copper plate) only add less than 1 minute to the preparation time before conducting GPR survey, compared to the traditional stationary signal shooting towards copper plate, which takes around 40 s. The calibration process of each reflection amplitude does not significantly burden the post-processing step, as the algorithm can be pre-programmed and used for multiple projects. However, it is recommended to conduct the calibration step for the polynomial coefficients in each field test, even for the same antenna frequency. This is because these coefficients are influenced by the dielectric properties of the target materials and the thickness of the individual pavement layers.

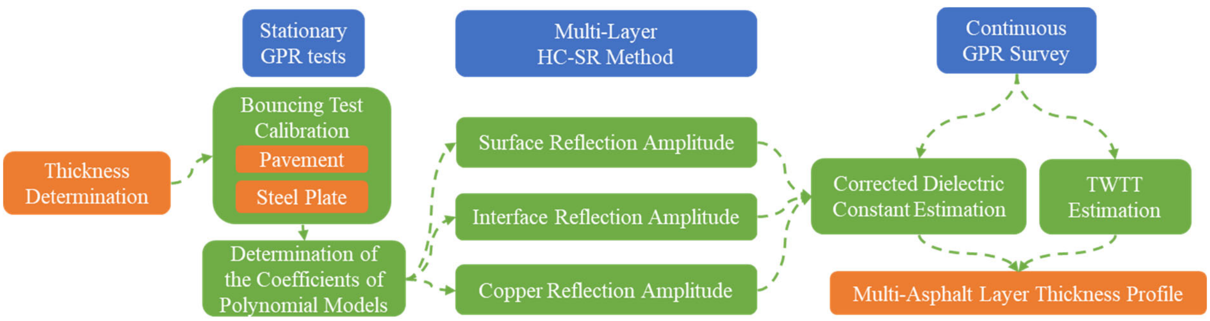

Figure 4.25 The workflow of applying the proposed HC-SR method for asphalt pavement thickness determination

4.4 Summary

In this chapter, the relationship between the antenna-surface height and the amplitude of each reflection in the GPR signal was investigated through FDTD simulation. An HC-SR method was proposed to eliminate the vibration effect caused by high-frequency tire-pavement interaction during high-speed surveys or unexpected low-frequency swaying or shifting. The proposed method was validated through in-situ core measurements and continuous GPR surveys. The deliverables of this study contribute to the capacity of individual estimation of sub-surface asphalt layer thickness with higher accuracy. The main findings are drawn as follows:

(1) The relationship between antenna-surface height and reflection amplitude follows a third-order polynomial law, which outperforms the power law, exponential law, and the inverted law as suggested in the literature. This phenomenon is more robust for interface reflection amplitude cases than surface and bottom reflection cases, enhancing the estimation accuracy of individual layer thickness.

(2) The thickness profile could be significantly smoothed, after the irregular vibration effect is removed by using the proposed HC-SR method. The overall GPR-based average error of thickness estimation was improved by 13.3%, 19.9%, and 17.4% for the first, second, and whole asphalt layers, respectively, compared to the traditional SR method.

(3) It is suggested implementing bouncing tests towards both the target pavement and the copper plate in real applications, replacing stationary signal shooting sorely on the copper plate. The proposed HC-SR method is also recommended for dielectric constant estimation instead of using the traditional SR method. Air-coupled antennas with central frequency higher than 1 GHz is recommended. The proposed workflow improves GPR-based thickness determination accuracy without significantly sacrificing applicability because the on-site preparation work is short, and the HC-SR method could be pre-programmed into the post-processing steps.

CHAPTER 5 IN-SITU GROUTING RATE PREDICTION OF SEMI-FLEXIBLE PAVEMENT USING GROUND-PENETRATING RADAR

The objectives of this chapter are firstly, to formulate a composite dielectric constant model for SFP guided by EM mixing theory. Subsequently, to derive the correlation between grouting rate and the dielectric constant, which can be used to inform uneven distribution of the grouting material within SFP. Sensitivity analysis is applied to the proposed model to ascertain the influence of each critical parameter. Additionally, the validity of the proposed model is verified through meso-scale numerical simulations of SFP and GPR systems, as well as indoor GPR tests on PA matrix, pure cement grouts, and SFP specimens. Finally, this study proposes an on-site procedural framework for applying GPR and the proposed method for practical grouting rate estimation. The outcomes of this study yield an automated, non-destructive estimation method for grouting rate with heightened precision, which accelerates the adoption and enhances the application of SFP.

5.1 Model Derivation

5.1.1 SFP Composite Dielectric Constant Model and Grouting Rate Prediction Model

EM mixing theory reveals that the bulk dielectric constant of a composite material is determined by the dielectric constant of its components, as well as their volumetric fractions. A general power-law mixing formula was provided by Sihvola (1989) for heterogeneous materials, such as asphalt mixture and concrete, as shown in the following equation:

$$\varepsilon_{eff}^{\beta} = \sum_{i=1}^{N} V_i \varepsilon_i^{\beta} \qquad (5-1)$$

Where ε_{eff} is the bulk dielectric constant of the composite mixture; V_i and ε_i is the volumetric fraction and the dielectric constant of the i^{th} phase, respectively; and β is an empirical power parameter. When β equals 0.5, the formula converts to the CRIM model [99]; when β equals 0.33, the formula converts to the Looyenga model [100].

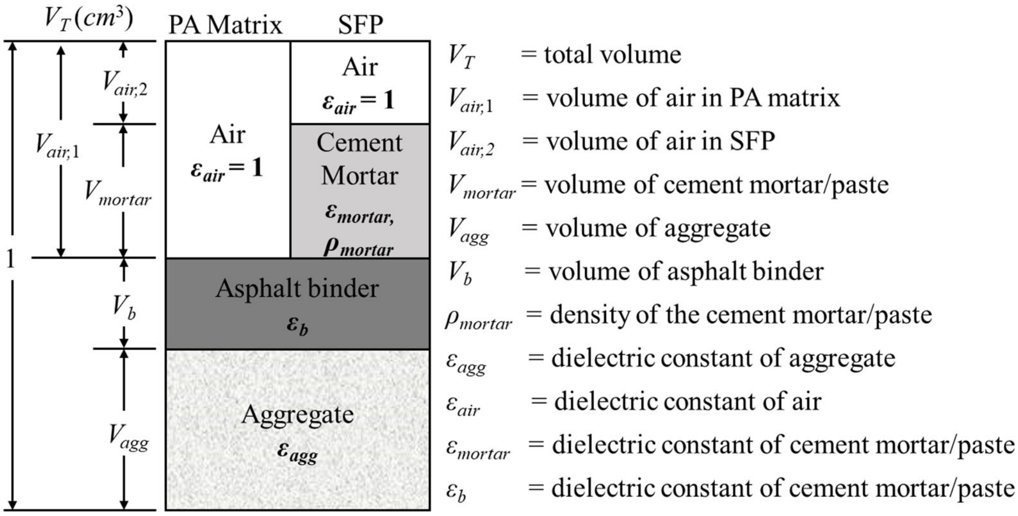

Figure 5.1 Composition and Parameters of PA matrix and SFP

Figure 5.1 shows the geometric properties of the PA matrix and the SFP. The formula of the PA matrix could be expressed as Equation (5-2) using the general formula of the EM mixing theory:

$$\varepsilon_{PA}^{\beta} = V_{agg}\varepsilon_{agg}^{\beta} + V_b\varepsilon_b^{\beta} + V_{air,1}\varepsilon_{air}^{\beta} \qquad (5-2)$$

where ε_{PA}, ε_{agg}, ε_b, and ε_{air}, is the dielectric constant of the PA matrix, aggregate, binder, and air, respectively; and V_{agg}, V_b, and $V_{air,1}$ is the volume weight of aggregate, binder, and air, respectively. By treating the asphalt mixture skeleton as an integral entity, Equation (5-2) becomes Equation (5-3):

$$\varepsilon_{PA}^{\beta} = (V_{agg} + V_b)\varepsilon_{PA,E}^{\beta} + V_{air,1}\varepsilon_{air}^{\beta} \qquad (5-3)$$

where $\varepsilon_{PA,E}$ is the equivalent dielectric constant of the asphalt mixture skeleton. It is noted that $\varepsilon_{PA,E}$ only represents the bulk dielectric constant of the asphalt mixture skeleton under the volumetric proportion of $(V_{agg} + V_b)$ and $V_{air,1}$ at this specific stage, devoid of intrinsic physical significance. Equation (5-3) can be algebraically rearranged to yield an expression for $\varepsilon_{PA,E}$, as illustrated in Equation (5-4):

$$\varepsilon_{PA,E} = \sqrt[\beta]{\frac{\varepsilon_{PA}^{\beta} - V_{air,1}\varepsilon_{air}^{\beta}}{\left(V_{agg} + V_b\right)}} \qquad (5-4)$$

In the PA matrix, the asphalt binder mainly wraps the coarse aggregate to form the asphalt mixture skeleton, providing cohesiveness and transferring compressive, tensile, and shear stress [101]. The thickness of the asphalt binder film is generally under 20 microns [102]. The radius of the spherical scatterers, composed of aggregate and the asphalt binder, barely increases, compared with the aggregate as the sole scatterers in previous EM mixing theory. This observation validates the applicability of the power-law model to the composite dielectric constant model for SFP [5]. The bulk dielectric constant of SFP was given in Equation (5-5) by treating the aggregate and the asphalt binder as an integrated unity:

$$\varepsilon_{SFP}^{\gamma} = \left(V_{agg} + V_b\right)\varepsilon_{PA,E}^{\gamma} + V_{air,2}\varepsilon_{air}^{\gamma} + V_{mortar}\varepsilon_{mortar}^{\gamma} \qquad (5-5)$$

where ε_{SFP} and ε_{mortar} is the bulk dielectric constant of the SFP and the grouting material, respectively; $V_{air,2}$ accounts for the remaining air void content of the SFP after grouting; V_{mortar} denotes the volumetric fraction of the grout; and γ is an empirical power parameter analogous to β. The relationship between the initial air void content of the PA matrix, the volume of the grouted cement mortar, and the remaining air void content in SFP is shown in Equation (5-6). By substituting Equation (5-6) into Equation (5-5), Equation (5-7) was obtained. By considering the geometry property of PA matrix as seen in Equation (5-8), substituting Equation (5-4) into Equation (5-7), as well as rearranging Equation (5-7), the expression of the remained air void content in SFP was obtained as seen in Equation (5-9):

$$V_{air,1} = V_{air,2} + V_{mortar} \qquad (5-6)$$

$$\varepsilon_{SFP}^{\gamma} = \left(V_{agg} + V_b\right)\varepsilon_{PA,E}^{\gamma} + V_{air,1}\varepsilon_{mortar}^{\gamma} + (\varepsilon_{air}^{\gamma} - \varepsilon_{mortar}^{\gamma})V_{air,2} \qquad (5-7)$$

$$V_{agg} + V_b = 1 - V_{air,1} \qquad (5-8)$$

$$V_{air,2} = \frac{V_{air,1}\varepsilon_{mortar}^{\gamma} + \left(1 - V_{air,1}\right)\sqrt[\frac{\beta}{\gamma}]{\frac{\varepsilon_{PA}^{\beta} - V_{air,1}\varepsilon_{air}^{\beta}}{(V_{agg}+V_b)}} - \varepsilon_{SFP}^{\gamma}}{(\varepsilon_{mortar}^{\gamma} - \varepsilon_{air}^{\gamma})} \qquad (5-9)$$

By substituting Equation (5-9) into the definition of the grouting rate of SFP (Equation (5-10)), eventually, an SFP grouting rate detection formula were derived based on a novel SFP composite dielectric constant model, as seen in Equation (5-11), referred to as the Leng-Wang-Sui (LWS) model in this paper:

$$G_r = \frac{V_{air,1} - V_{air,2}}{V_{air,1}} = 1 - \frac{V_{air,2}}{V_{air,1}} \qquad (5-10)$$

$$G_r = 1 - \frac{\varepsilon_{mortar}^{\gamma} + \left(\frac{1}{V_{air,1}} - 1\right)\sqrt[\frac{\beta}{\gamma}]{\frac{\varepsilon_{PA}^{\beta} - V_{air,1}\varepsilon_{air}^{\beta}}{(1-V_{air,1})}} - \frac{1}{V_{air,1}}\varepsilon_{SFP}^{\gamma}}{\left(\varepsilon_{mortar}^{\gamma} - \varepsilon_{air}^{\gamma}\right)} \qquad (5-11)$$

5.1.2 Sensitivity Analysis

In the proposed LWS model, the grouting rate hinged on six key parameters, including ε_{PA}, ε_{SFP}, ε_{mortar}, β, γ, and $V_{air,1}$. A methodical sensitivity analysis was employed to elucidate the influence of each parameter within the LWS model. The analysis incorporated both the CRIM model and Looyenga model to guide the selection of β and γ. The results of this sensitivity analysis are depicted in Figure 5.2. The analysis revealed that discrepancies in the primary parameters exert a substantial impact on the grouting rate estimation. For example, an erroneous assumption of ε_{SFP} at 5 rather than 7, as illustrated in Figure 5.2 (b), precipitates a marked decrease in the predicted grouting rate from 92% to a mere 21%.

The selection of the power indices β and γ predominantly influences the low ε_{mortar} range and the high ε_{SFP} range. Specifically, these effects are most pronounced in the context of low moisture content during the preparation of grouting materials (low ε_{mortar} range) and the elevated moisture content during the curing phase of SFP (high ε_{SFP} range). This highlights the criticality of accounting for and mitigating the impact of moisture content throughout the accuracy of the LWS model's predictions.

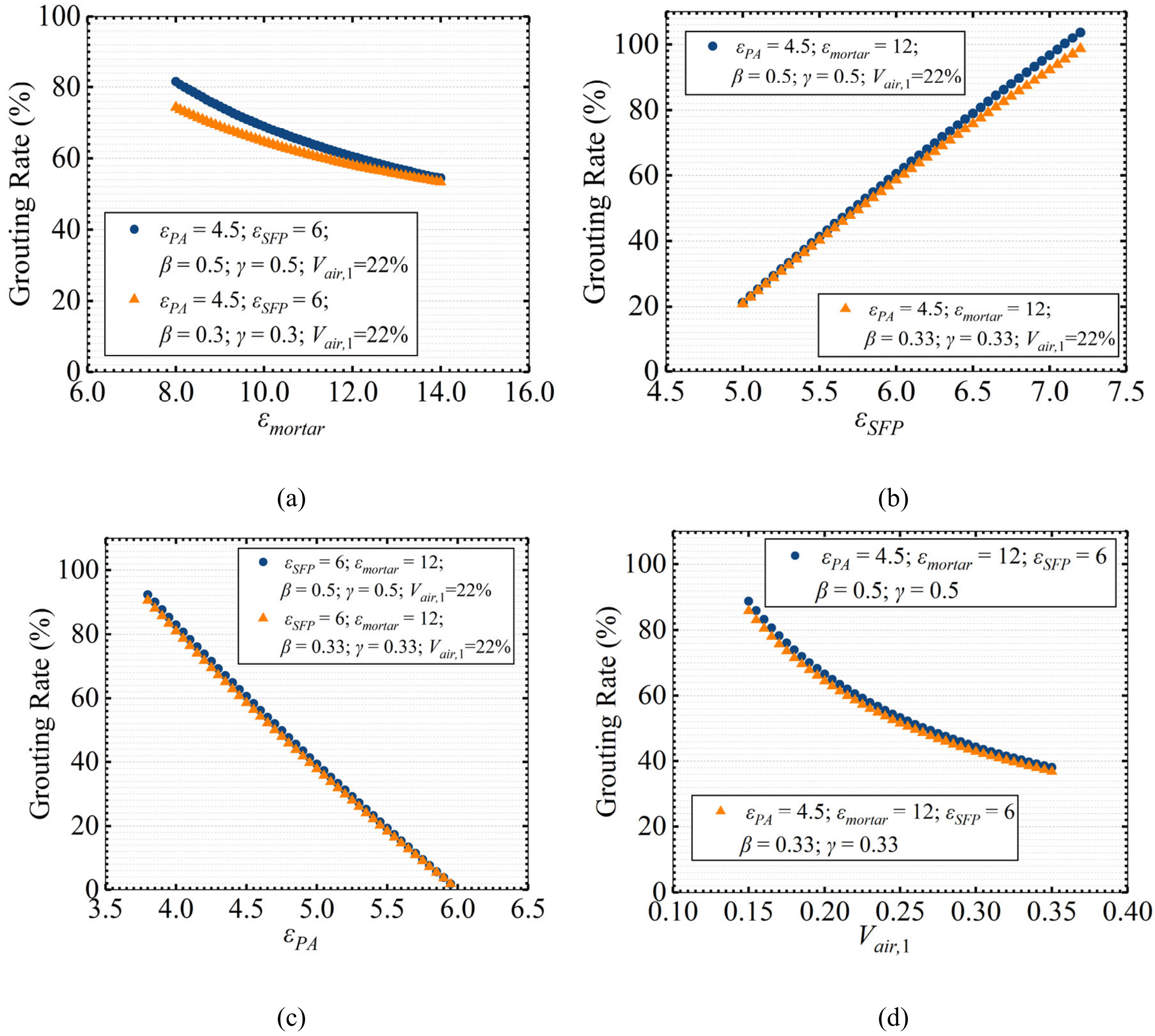

Figure 5.2 Sensitivity analysis results of the four primary parameters in the proposed LWS model under different β and γ selection; (a) ε_{mortar}; (b) ε_{SFP}; (c) ε_{PA}; (d) $V_{air,1}$

The efficacy of the proposed LWS model for predicting the grouting rate of SFP is contingent upon the precise understanding of the influence and interplay of its constituent parameters. To this end, a global sensitivity analysis was implemented employing the Saltelli-Sobol method [103], renowned for its Monte Carlo simulation foundation. The execution of this analysis was facilitated by the SALib package library in Python [104]. In excess of 140000 parameter sequences, encompassing ε_{PA}, ε_{SFP}, ε_{mortar}, β, γ, and $V_{air,1}$, were generated via the Saltelli sampler. Subsequent Sobel sensitivity analysis was used to delineate each parameter's contribution and interaction within the model. This was quantified through a trio of indices, including the first-order indices and the total sensitivity indices gauging the individual contribution of each parameter, and the second-order sensitivity indices evaluating the interactions between parameter pairs [103].

Analysis results were depicted in Figure 5.3 and 5.4, which illustrate the dominance of ε_{PA} and ε_{SFP} in affecting the grouting rate prediction, thus aligning with insights from prior sensitivity assessments. Additionally, Figure 5.5 demonstrates that $V_{air,1}$ and ε_{mortar} affect the performance of the LWS model due to their correlation with ε_{PA} and ε_{SFP}. The analyses jointly underscore the criticality of precise measurement or estimation of ε_{PA} and ε_{SFP} post grouting and curing in using LWS model for SFP grouting rate prediction. Overall, the sensitivity of the parameters can be ranked in descending order of influence: $\varepsilon_{PA} > \varepsilon_{SFP} > V_{air,1} > \varepsilon_{mortar}$.

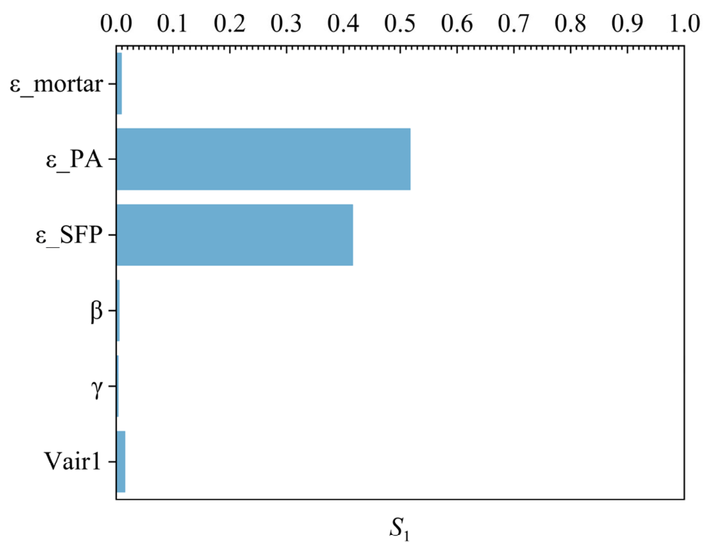

Figure 5.3 Sobol-Saltelli first-order sensitivity indices for the LWS model

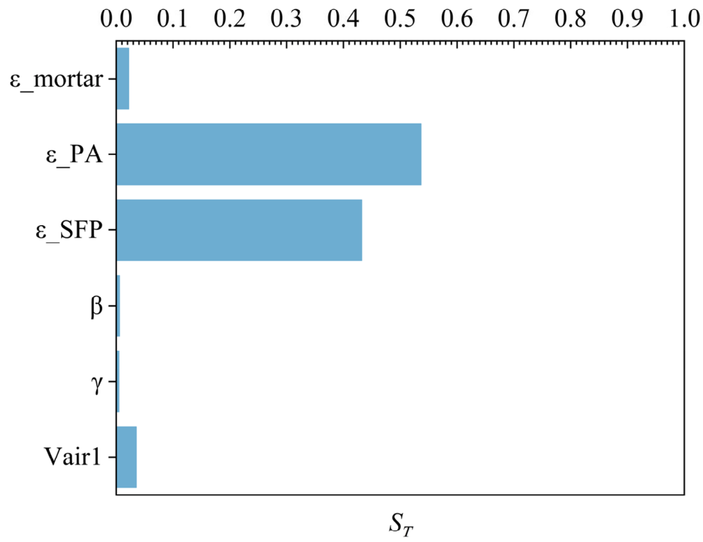

Figure 5.4 Sobol-Saltelli total effect sensitivity indices for the LWS model

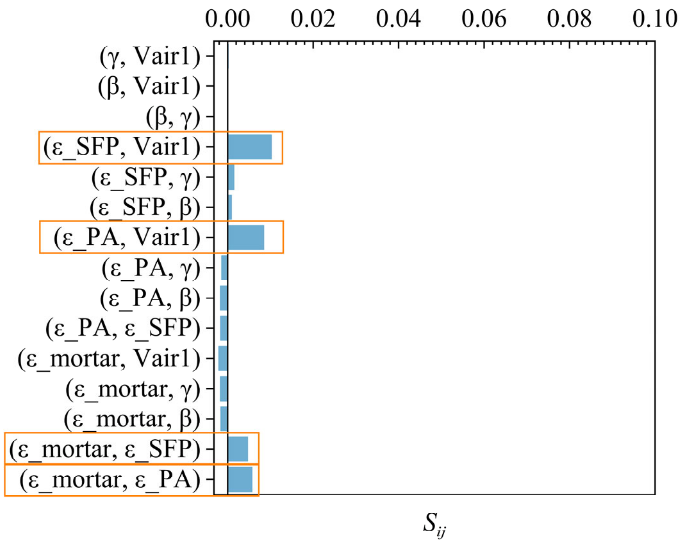

Figure 5.5 Sobol-Saltelli second-order sensitivity indices for the LWS model

5.2 Performance Validation Using FDTD Simulation

5.2.1 Numerical Model Setup and Organization

To assess the effectiveness of the derived LWS model, 2-D numerical models of GPR-SFP system were constructed using gprMax 2D. Figure 5.6 illustrates the detailed schematic of a 2-meter longitudinal cross-section of SFP, showcasing a depth of 10 cm. In this study, a 2 GHz air-coupled GPR system was utilized, with the antenna positioned at a height of 40 cm. The Ricker wave was used as the excitation source. To ensure an adequate horizontal sampling rate, the trace distance was set to 0.001 m. The vertical signal sampling rate was set as 5089 samples per trace, which was automatically calculated by gprMax based on the model's geometry and the spatial discretization.

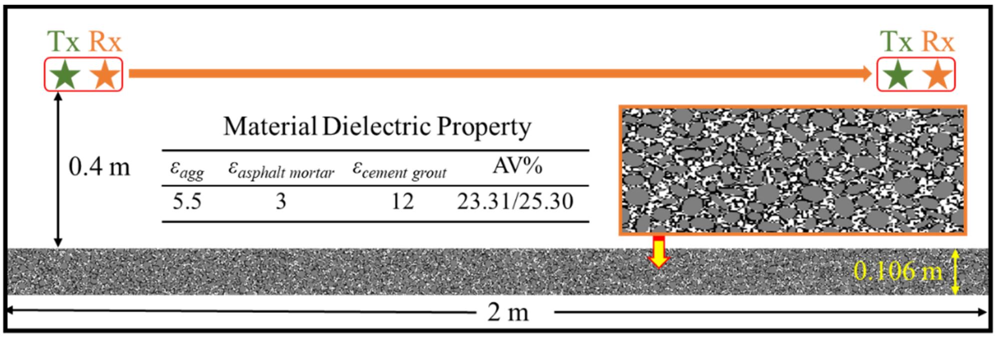

Figure 5.6 Numerical model setup and organization of GPR-SFP system

The meso-scale characteristics of SFP were considered when constructing the numerical model by employing a random aggregate generation technique. Two SFP gradations were designed with target (actual) air void contents of 23.31% and 25.30%, respectively. The meso-scale models were modelled as four-phase mixtures, consisting of random polygonal coarse aggregate (≥ 2.36 mm) as the skeleton, asphalt mortar (binder and fine aggregates) as the background material, air voids, and cement grout. The dielectric properties of the materials are detailed in Figure 5.6. The meso-scale models were constructed through a meticulously structured process, delineated as follows:

1. Calculate the number of aggregates in each sieve size based on the gradation, binder content, air void content of the PA matrix, and the overall model geometry.
2. Randomly generate and place the coarse aggregate within the designated zone. To prevent overlap between aggregates, the following governing parameters, as depicted in Figure 5.7, are considered and checked.

$$r_i = R_0 + (2\varphi - 1) \times R \qquad (5-12)$$

$$\theta_i = \frac{2\pi}{n} + (2\tau - 1) \times \frac{2\pi}{n} \times 0.5 \qquad (5-13)$$

where r_i is the polar radius of the irregular polygons; θ_i is the angle between polar radii; R_0 is the average aggregate radius; R is the range of fluctuation for aggregate radius; φ and τ are random number fluctuating in (0, 1), and n is the number of sections that the aggregate is divided into. To avoid overlaps between aggregates, the sum of circumscribed radii of any two adjacent aggregates should be less than the distance between their centroids, i.e., $d_i + d_j \leq D$.

3. Define the region within the model boundary that is not occupied by coarse aggregates as asphalt mortar.
4. Randomly generate air voids within the asphalt mortar region based on the target air void content of the PA matrix.
5. For a specific PA matrix model, randomly generate the cement grout within the air void region based on the target ground truth grouting rate, ranging from 0% to 100% with an interval of 5%.

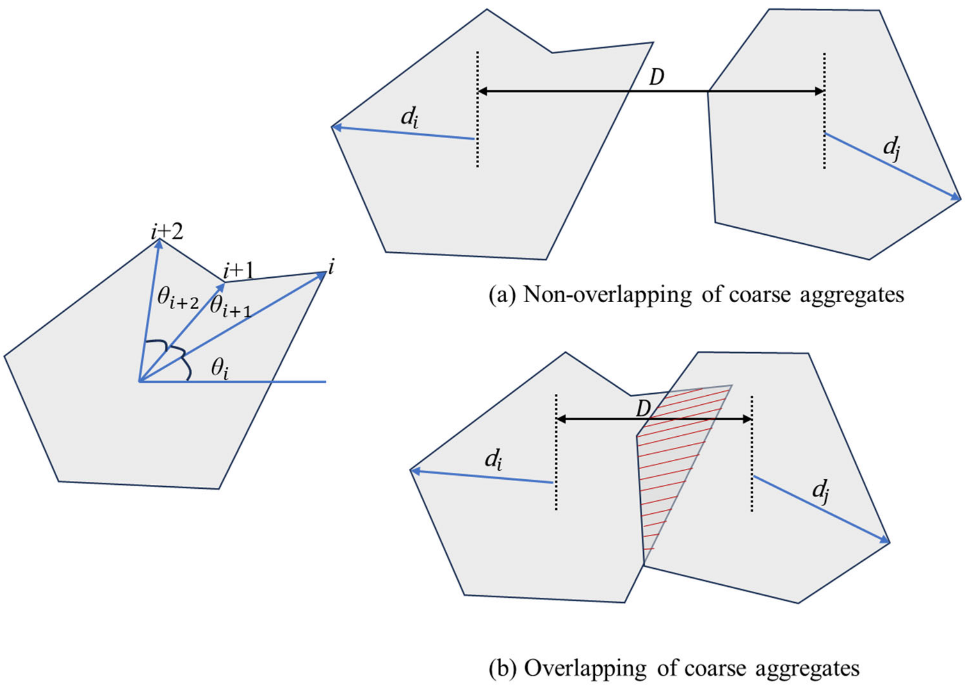

Figure 5.7 Schematic of generated aggregate particle and relationships of aggregate placement position

The first four steps were executed five times for each gradation, resulting in the establishment of 10 PA matrices with distinct meso-structures. This led to the creation of 210 SFP models with varying grouting rates. The dielectric constant of the SFP was determined using the TOF method.

5.2.2 Simulation Results and Discussion

Figure 5.8. illustrates the back-calculated dielectric constant of SFP models with varying grouting rates but the same PA matrix structure. As expected, there is a discernible increase in the bulk dielectric constant of the SFP as the air voids are gradually filled with injected grouts. Although slight differences in regression coefficients can be observed among different mixes, linear correlations between grouting rate and dielectric constant of SFP is evident, highlighting the effectiveness of meso-scale SFP models.

Figure 5.9. presents the estimation error of SFP grouting rate using the proposed LWS model, including the mean value and the standard deviation. In general, the estimation error profile for each mix is characterized by a convex trajectory. The maximum estimation error occurred around 40% and 50% grouting rates, with values of 5.7% and 5.3% for mix I and II, respectively. Notably, as grouting rates extend beyond these critical points, there is a marked improvement in the model's accuracy, with the average error decreasing and the variance constricting. Upon reaching a grouting rate threshold of 80%, a prevalent benchmark in real-world SFP implementations, the estimation error attenuates to about 4.0%, accompanied by a variance reduction to approximately 1.0%. This level of precision is further enhanced when the pavement is completely grouted, where the estimation error converges towards 2%, signifying the LWS model's applicability at accurate predictions. The observed variance in error is attributable to the realistic representation of the meso-scale structure within the model, which is a factor that has rarely been considered in previous FDTD simulation of pavement systems.

This consideration endows the numerical models with a notable advantage in reflecting the true heterogeneity of SFP materials, thereby enhancing the reliability of grouting rate estimation.

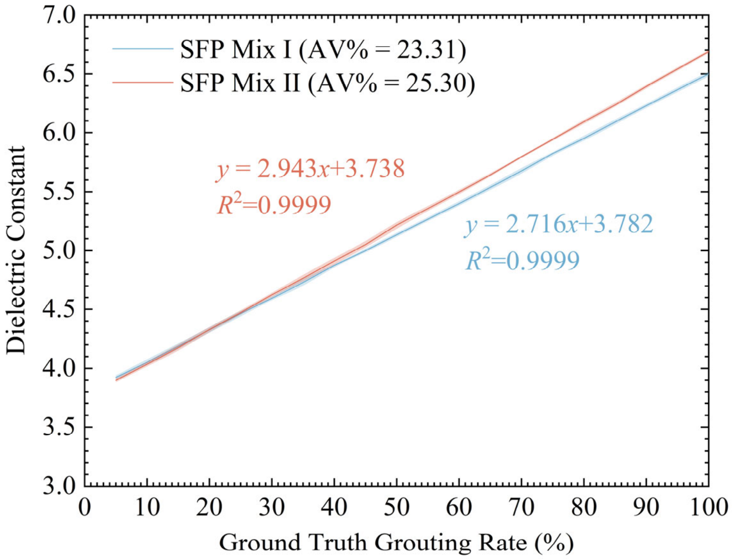

Figure 5.8 Dielectric constant of SFP under different grouting rate

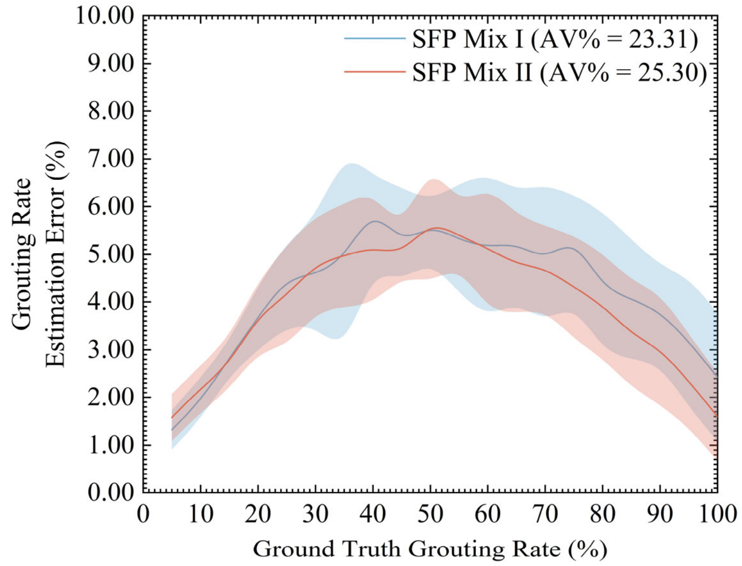

Figure 5.9 Grouting rate estimation error using LWS model at different ground truth grouting rates levels

5.3 Laboratory Test Validation

5.3.1 Specimen Preparation and GPR Setup

A series of controlled laboratory tests were conducted to validate the effectiveness of the proposed LWS model. These tests incorporated GPR measurements on materials integral to

SFP construction, specifically pure cement grout, the PA matrix, and the SFP itself. To facilitate the testing, a slab made of cement grout, supplied by Subote New Materials Co., Ltd. in Jiangsu province, China, was manufactured. The slab dimensions were precisely controlled, being 450 mm in length, 350 mm in width, and 74 mm in thickness. Further, SGC specimens, encompassing both PA matrix and SFP were sequentially manufactured with dimensions of 150 mm in diameter and 97.5 mm in height. The adoption of the SGC specimens is grounded in their widespread recognition and endorsement within the pavement engineering community, particularly due to their compliance with Superpave specifications, which is an essential factor for validation of the LWS model. The PA matrix was carefully wrapped and sealed in thin plastic film and complemented with taps to ensure proper containment of the cement grout. Consistent with the guidelines provided by the material supplier, both the slab and SGC specimens were maintained in a static state within the curing environment for a duration of 14 days, ensuring optimal material properties for testing. A total of 18 SGC specimens of PA matrix were manufactured featuring varying air void content ranging from 20% to 30%. This variability was crucial in evaluating the performance of the LWS model across different porosity levels prevalent in the field applications. Figure 5.10 showcases the manufactured slab and SGC specimens.

(a) (b) (c) (d)

Figure 5.10 Materials and Specimens: (a) cement mortar slab; (b) PA matrix; (c) Preparation; (d) SGC specimens of SFP

The feasibility of utilizing GPR for evaluating SGC specimens, shanking the footprint of the emitted short EM wave, has been verified by prior investigations [105]. In this study, 2 GHz palm antenna was employed due to its handleability and high resolution. It is critical to underscore the proper positioning of the antenna in relation to the specimen during measurements. Direct contact between the antenna and the specimens is to be avoided to prevent the masking of the target reflection of the specimen surface by the direct coupling pulse from the antenna transmitting and receiving pair. The GPR manufacturer recommends a minimum clearance of 12 cm above the specimen to ensure a visible target signal reflection. However, adherence to this recommended antenna elevation introduces a challenge. Such antenna height results in a larger spatial footprint, specifically the first Fresnel zone, which surpass the boundaries of the SGC specimen. The radius of the Fresnel zone can be as determined using the following equation [90]:

$$r_f = \frac{1}{2}\sqrt{2\lambda h} \qquad (5-14)$$

where r_f is the radius of the Fresnel zone; h is the height between antenna and the specimen upper surface; λ is the wavelength of the EM wave, which could be calculated using the following relation: $\lambda = c/(\sqrt{\varepsilon} f)$; ε is the dielectric constant of the medium between antenna and the surface (in this case, the medium is the free space with a dielectric constant of 1; and f is the central frequency of the antenna (2 GHz).

Utilizing Equation (5-14), it has been determined that with an antenna height of 12 cm, the radius of the EM wave footprint is calculated to be 9.49 cm. This value surpasses the radius of a standard SGC specimen, which is 7.5 cm. Consequently, this leads to the undesirable phenomenon of edge diffraction of EM energy from the antenna. This effect results in the erroneous detection of interface reflections on both lateral faces of the specimen within the GPR signal waveform [106].

To avoid this edge diffraction effect, a spacer method was employed [94, 95]. This technique is graphically demonstrated in Figure 5.11. The underlying principle of this method is to reduce the propagation velocity of the EM waves by introducing an intermediary material with a known and distinct dielectric constant positioned between the antenna and the specimen surface, as depicted in Figure 5.11. In accordance with Snell's law, the refractive path of the EM wave bends more closely towards the normal (perpendicular) within a medium that possesses a higher dielectric constant compared to that of air. This leads to a reduction in the radius of the first Fresnel zone when the wave enters the upper surface of SGC specimen. and keep it within. One critical aspect to consider is the selection of the spacer material. Its dielectric constant must be different from that of SGC specimen to ensure that the reflections from the specimen's surface and bottom are clearly distinguishable in the GPR A-scan readings.

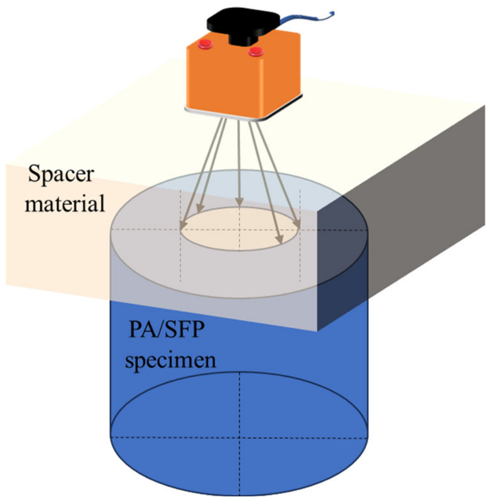

Figure 5.11 GPR measurements on SGC specimens using the spacer method

In this section, a 4 cm thick POM plastic plate with a known dielectric constant of 2.88 was used as the spacer between the GPR and the test specimen. The employment of this POM spacer effectively contracted the radius of the first Fresnel zone to 7.28 cm, marginally less than the SGC specimen's radius of 7.5 cm. Through this optimized antenna-spacer configuration and given the specimen's thickness of 9.75 ± 0.5 cm, the GPR system was capable of distinctly positioning the surface and the bottom reflection of the specimen from other multiple diffraction reflections, as validated in the literatures [94, 95].

The GPR measurement procedure entailed a sequence of four distinct experimental setups. Each setup was systematically analyzed to interpret the corresponding GPR signals: (1) spacer only, (2) spacer with a steel plate, (3) spacer with the SGC specimen, and (4) spacer with both the SGC specimen and the steel plate, marked as signal I, II, III, and IV, as demonstrated in Figure 5.12. The steel plate functions as a perfect EM reflector, ensuring full return of the EM energy back to the antenna, thereby serving as a measurement of the incident reflection. Two synthetic signals can be obtained by subtracting signal I from signal II, and by subtracting signal III from signal IV, respectively. This enabled the unambiguous identification of the SGC specimen's surface and bottom reflections by locating the first prominent negative peak within the synthetic signals, as explicated in Figure 5.13.

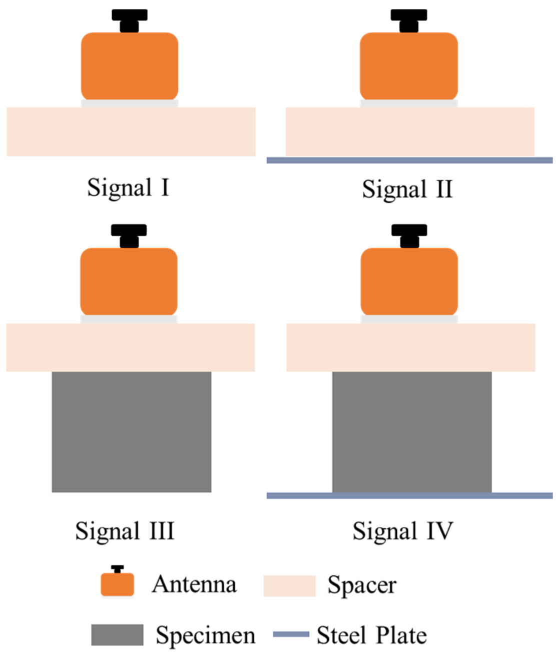

Figure 5.12 GPR measurement configurations using the spacer method

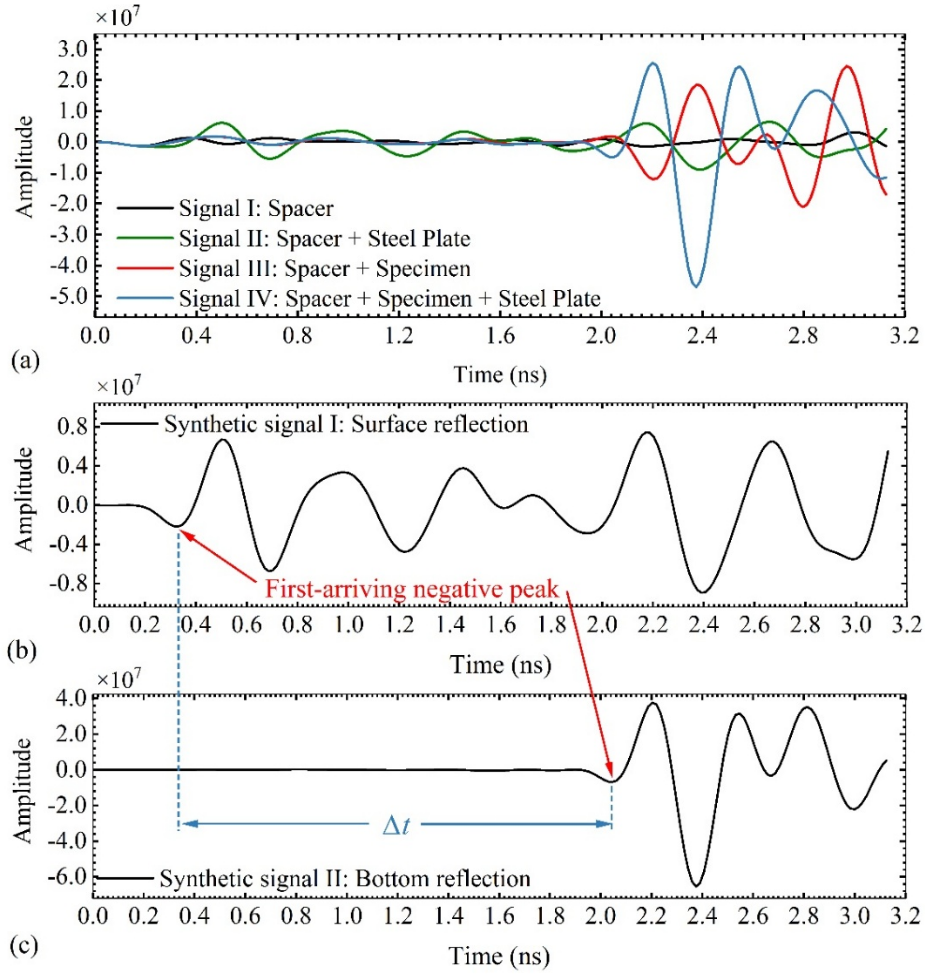

Figure 5.13 Raw GPR signals and the synthetic signals: (a) Raw GPR waveforms under adopted configurations; (b) synthetic signal for surface reflection positioning; (c) synthetic signal for bottom reflection positioning

The dielectric constant of the SGC specimens were also calculated using TOF method. However, it should be noted that the time-of-flight between the specimen surface reflection and the bottom reflection does not represent the true two-way travel time for the EM wave travelling through the SGC specimen. This discrepancy is depicted in Figure 5.14. Authentic formula for TWTT calculation was derived using the following equations [95].

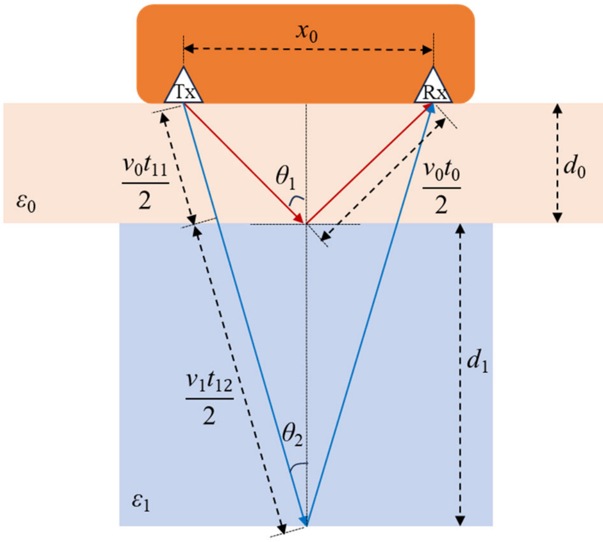

Figure 5.14 Dielectric constant calculation using TOF method under spacer method configuration

$$\theta_1 = \frac{x_0}{2}\tan\left(\frac{x_0}{2d_0}\right) \quad (5-15)$$

$$\theta_2 = \frac{x_0}{2}\tan\left(\frac{x_0}{2(d_0+d_1)}\right) \quad (5-16)$$

$$t_0 = \frac{2d_0}{\left(\frac{c}{\sqrt{\varepsilon_0}}cos\theta_1\right)} \quad (5-17)$$

$$t_1 = t_{11} + t_{12} = \frac{2d_0}{\left(\frac{c}{\sqrt{\varepsilon_0}}cos\theta_2\right)} + \frac{2d_1}{\left(\frac{c}{\sqrt{\varepsilon_1}}cos\theta_2\right)} \quad (5-18)$$

$$t_1 - t_0 = \Delta t \quad (5-19)$$

where θ_1 and θ_2 are the reflection angle of EM wave in the spacer and SGC specimen, respectively; d_0 and d_1 are the thickness of the spacer and SGC specimen, respectively; x_0 is the distance between the transmitter and the receiver of the antenna, which equals 6 cm according to the GPR vendor. ε_0 and ε_1 are the dielectric constant of the spacer and the SGC specimen, respectively; t_0 is TWTT of the surface reflection pulse; t_1 is TWTT of bottom reflection pulse that equals the sum of time of flight in the spacer and SGC specimen; and Δt is the time difference of the first-arriving negative peak between the surface and bottom reflection in Figure 5.13 (b) and (c). By substituting Equations (5-15) - (5-18) into Equation (5-19), the dielectric constant of SGC specimen could be calculated as follows:

$$\varepsilon_1 = \left[\frac{c\Delta t cos\theta_2}{2d_1} - \frac{d_0}{d_1}\sqrt{\varepsilon_0}\left(1 - \frac{cos\theta_2}{cos\theta_1}\right)\right]^2 \qquad (5-20)$$

The dielectric constant of the cement grout, PA matrix, and the SFP of 18 SGC specimen were obtained using Equation (5-20). The air void content of each specimen was measured using volumetric method before grouting [107]. The ground truth value of the grouting rate of the specimen was measured using the following equation:

$$G_r = \frac{m_0 - m_1}{\pi \rho V_{air,1} h r^2} \qquad (5-21)$$

where m_0 and m_1 are the weight of the SGC specimen after and before filling the grouting material; ρ is the density of the grouting material, which is 1.977 g/cm^3; h is the height of the specimen; and r is the radius of the specimen.

5.3.2 Results and Discussion

The geometry characteristics of the fabricated 18 SGC specimens are detailed in Table 5.1. Measured parameters include the actual height of the specimen, actual air void content of the PA matrix, and the measured specimen weight before and after the grouting. The average thickness of all analyzed specimens was measured at 9.59 cm, with a mean square error (MSE) of 0.31 cm. The actual air void content of the PA matrix exhibited a considerable range, spanning from 18.62% to 29.38%. Noted that this variation was intentionally introduced by utilizing three distinct gradations with designed air void content of 20%, 25%, and 30%, respectively. These specific gradations were sourced from in-place SFP projects, thereby providing a realistic assessment of the LWS model in real-world applications.

Table 5.1 Geometry properties of the SGC specimens

No.	Height (cm)	$V_{air,1}$ (%)	M_0 (g)	M_1 (g)	Grouting Rate (%)
1	8.70	18.62	3252.80	3457.30	36
2	9.50	21.34	3433.50	3742.60	44
3	9.40	21.74	3380.10	3872.60	69
4	9.90	22.00	3548.00	3725.20	23
5	9.50	27.99	3246.00	3757.40	55
6	9.80	26.80	3403.90	3765.70	39
7	9.60	26.61	3342.90	3639.30	33
8	10.20	29.38	3417.00	3995.20	55
9	9.70	23.18	3423.50	3529.40	13
10	9.60	21.90	3445.00	3621.80	24
11	9.60	23.19	3387.80	3613.5	29
12	9.40	22.71	3447.10	3796.10	47
13	9.40	21.01	3411.40	3845.60	63
14	9.60	25.51	3285.60	3582.30	35
15	9.60	28.11	3274.70	3836.50	60
16	10.00	24.72	3458.60	3978.00	60
17	9.70	21.98	3477.30	3671.80	26
18	9.50	23.09	3357.10	3657.50	39

The ground truth grouting rate results are also can be seen in Table 5.1. The grouting rate observed across the SGC specimens varied from 23% to 69%, independent from the initial air void content of PA matrix. During the grouting process, the specimens were consistently subjected to vibration on a jolt table to facilitate uniform distribution of the grout. The grouting procedure was halted upon visual confirmation that the penetration of the cement grout had ceased. This phenomenon revealed that insufficient grouting exists in both low and high air void content situations (with regard to SFP). The necessity of in-situ grouting rate monitoring is also highlighted.

The results of grouting rate prediction using LWS model with both CRIM and Looyenga power index selection, as well as the ground truth value using Equation (5-21), are presented in Figure 5.15. It is evident that the LWS model performed well in estimating the grouting rate. The mean estimation errors across all specimens were quantified at 11.30% for the LWS model employing the CRIM, and 10.57% for the LWS model employing the Looyenga power index selection, respectively, as shown in Figure 5.16. It is worth noting that the model accuracy was compromised by two anomalous specimens (No. 9 and No. 11), which exhibited significantly unreasonable prediction results. These outliers were attributed to substandard wrapping practices during the grouting process. The integrity of the thin plastic film utilized for encasing the specimens was found compromised, leading to leakage of the cement grout. This leakage resulted in the inadvertent formation of an additional layer at the bottom of the specimens, composed exclusively of the grout material, which in turn, impaired the prediction accuracy. Upon the exclusion of these aberrant cases, a notable enhancement in the mean estimation accuracy was observed for the remaining 16 specimens, with improved values dropping to 6.9% for the CRIM power index selection and 6.24% for the Looyenga power index selection. A consistent estimation error between simulation and laboratory test results was found. Furthermore, the analysis disclosed an improved performance of the LWS model when the power index β and γ were set to 0.3 rather than 0.5.

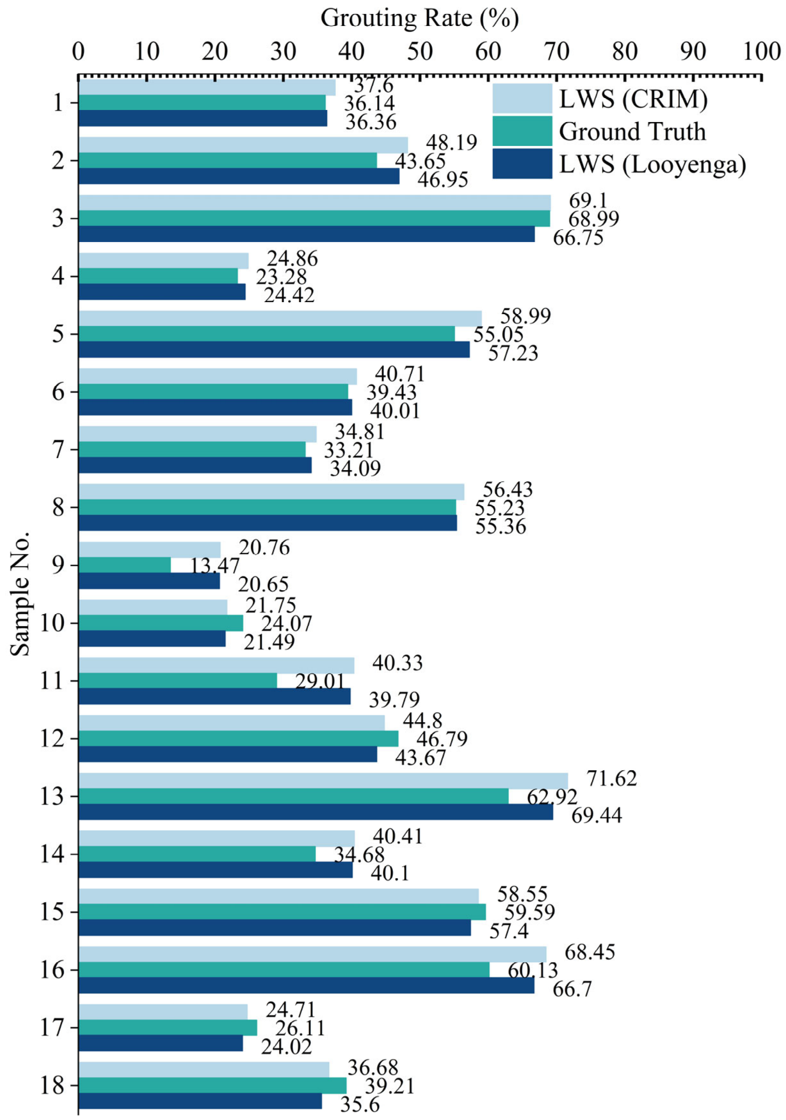

Figure 5.15 Results of the ground truth grouting rate and the predicted value using LWS model with both the CRIM and Looyenga β and γ selection

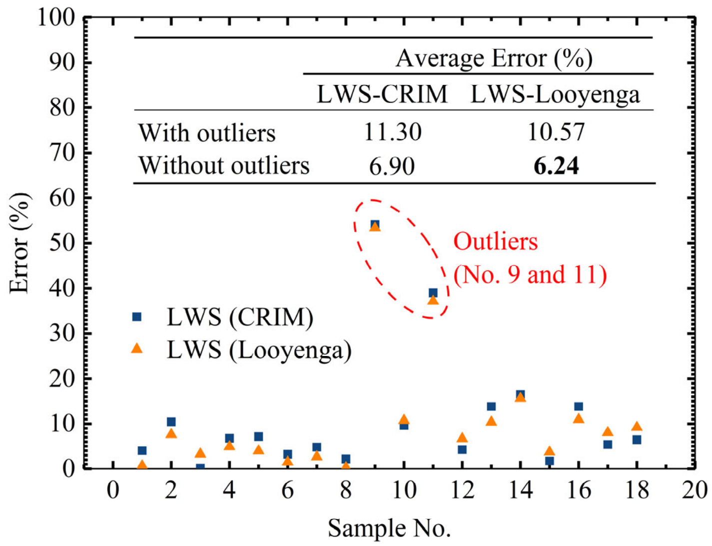

Figure 5.16 Estimation error of the LWS model with both the CRIM and Looyenga β and γ selection

To facilitate the implementation of the proposed grouting rate monitoring method within SFP pavements, a practical workflow is recommended, as depicted in Figure 5.17. Firstly, the dielectric constant of the used grouting material should be determined through indoor GPR measurement on grouting material slabs or SGC specimens. Subsequently, on-site GPR measurements should be conducted after the construction of the PA matrix and the SFP, respectively. The initial air void content of the PA matrix could be obtained using extracted in-situ cores during quality control (QC) procedures. It is important that the third GPR measurement on the grouted SFP must be conducted after the curing period to avoid incorrect ε_{SFP} measurements influenced by varying internal moisture content. The removal of the exceeding slurry of cement grouts on the pavement surface is equally important because the grouting rate prediction would be affected if thin cement grout layer exists. Finally, the proposed LWS model with $\beta$and γ set as 0.33 can be employed to predict in-situ grouting rate of the constructed SFP. For field applications, the air-coupled horn antenna or 3D antenna can be used instead of the palm antenna utilized in laboratory tests. This allows for traffic-speed surveys without causing delays in the SFP construction process.

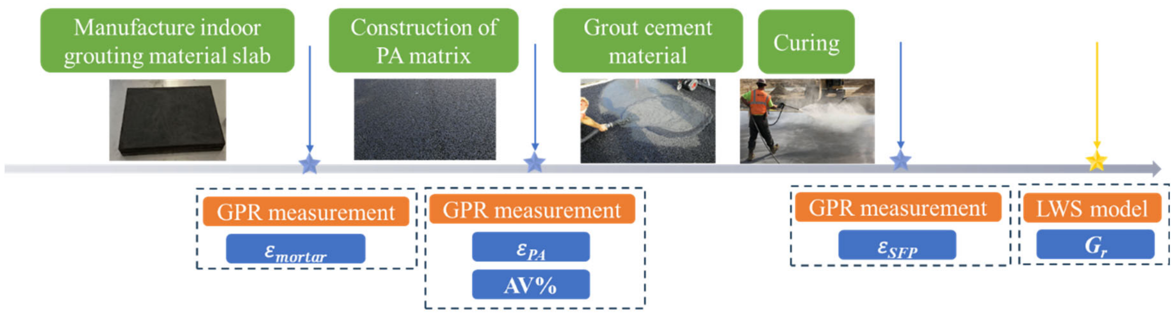

Figure 5.17 A recommended workflow of in-situ grouting rate prediction/measurement using the proposed LWS model

5.4 Summary

In this chapter, the feasibility of estimating the in-situ grouting rate of SFP using GPR was investigated. An automatic grouting rate determination method designated as the LWS model was developed based on a novel composite dielectric constant model of SFP. A comprehensive sensitivity analysis was conducted to evaluate the influence of primary parameters in the LWS model. FDTD numerical models considering meso-scale characteristics of SFP using a random aggregate generation technique were built and analyzed. Controlled laboratory tests were performed on grouting material slabs and SGC specimens using a 2 GHz palm antenna and in conjunction with a spacer method. The performance of the proposed model was validated from both simulation and laboratory test results. A practical workflow for field SFP applications using GPR and the proposed LWS model for in-situ grouting rate estimation was provided. The main findings of this chapter are drawn as follows:

(1) The in-situ grouting rate of SFP can be accurately estimated using GPR in tandem with the proposed LWS model. Meso-scale numerical simulations of GPR-SFP system reveal a convex correlation between the estimation error of LWS model and the actual grouting rate, with a peak error margin of less than 6% identified when the SFP grouting level approximate 50%. This margin of error is reduced to about 4.0% when the grout rate transcends an 80% threshold. Corresponding laboratory evaluations align with these findings, registering an average estimation error below 7%, thereby endorsing the model's capability for precise in-situ grouting rate assessments of SFP.

(2) The LWS model's prediction accuracy is highly contingent upon the dielectric constants of the PA matrix and SFP itself. The initial air void content in PA matrix, alongside the dielectric constant of the cement grout correlate to these two dielectric constants, thus influencing the prediction outcome. It is recommended that the power index β and γ be calibrated to 0.33, contrary to the conventional value of 0.5, to enhance the model's precision.

(3) An applicable workflow was provided for SFP projects with the implementation of multiple GPR measurements during each stage of construction, providing accurate in-situ grouting rate estimation. Two critical practices include the removal of excess

cement slurry post grouting and the deferral of GPR measurements until post-curing of SFP to mitigate potential inaccuracies. For traffic-speed surveys, the utilization of a high-frequency air-coupled horn antenna is advocated, promoting operational efficiency without compromising the SFP construction schedule.

CHAPTER 6 NON-INVASIVE MOISTURE CONTENT QUANTIFICATION OF FLEXIBLE PAVEMENT USING GPR

This chapter aims to develop a novel GPR-based MC prediction model with improved accuracy. To overcome the limitations of existing models, the proposed model is derived from a generalized power-law mixing theory, incorporating the effects of aggregate shape and air void content through optimized power indices. Meso-scale material characteristics of asphalt mixtures will be integrated into macro-scale GPR-pavement system simulations, enabling the generation of extensive numerical datasets to refine model coefficients. Finally, the proposed model will be validated through controlled laboratory GPR tests on both dry and wet asphalt mixtures. The outcomes of this research will facilitate real-time, non-destructive determination of asphalt pavement MC, enabling rapid and accurate early warnings of potential moisture-induced pavement failures

6.1 Moisture Content Prediction Model

The dielectric constant of the wet asphalt mixture can also be expressed using the power-law EM mixing theory with the aggregate and the binder treated as an integrated unity:

$$\varepsilon_{WAC}^{\gamma} = (V_s + V_b)\varepsilon_{AC,E}^{\gamma} + V_{a,2}\varepsilon_a^{\gamma} + V_w\varepsilon_w^{\gamma} \qquad (6-1)$$

where ε_{WAC} and ε_W are the dielectric constant of wet asphalt mixture and moisture, respectively; $V_{a,2}$ and V_W are the remaining air void content, and volume of moisture, respectively, and γ is another power index. Considering the relationship between the moisture volume and the air void content variation as seen in Figure 6.1, Equation (6-1) can be rearranged into Equation (6-2) by substituting Equation (5-4):

$$V_w = V_{a,1} - V_{a,2} \qquad (6-2)$$

$$\varepsilon_{WAC}^{\gamma} = (V_s + V_b)\varepsilon_{AC,E}^{\gamma} + V_{a,1}\varepsilon_w^{\gamma} + (\varepsilon_a^{\gamma} - \varepsilon_w^{\gamma})V_{a,2} \qquad (6-3)$$

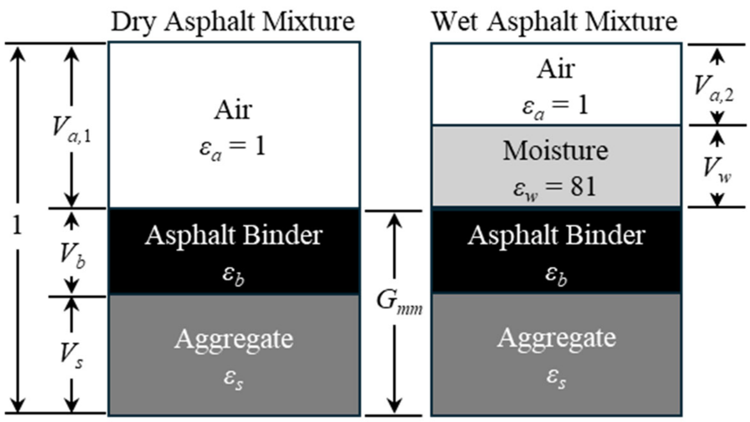

Figure 6.1 Wet asphalt mixture composition and parameters

Considering the volumetric relationship within the dry asphalt mixture, the calculation formula for air void content in wet asphalt mixture can be obtained:

$$V_s + V_b = 1 - V_{a,1} \qquad (6-4)$$

$$V_{a,2} = \frac{V_{a,1}\varepsilon_w^{\gamma} + \left(1 - V_{a,1}\right)\sqrt[\frac{\beta}{\gamma}]{\frac{\varepsilon_{AC}^{\beta} - V_{a,1}\varepsilon_a^{\beta}}{(1 - V_{a,1})}} - \varepsilon_{WAC}^{\gamma}}{(\varepsilon_w^{\gamma} - \varepsilon_a^{\gamma})} \qquad (6-5)$$

The calculation formula for moisture content can be finally obtained by considering the definition of saturation degree and its relationship to moisture content:

$$SR = \frac{V_w}{V_{a,1}} = \frac{V_{a,1} - V_{a,2}}{V_{a,1}} = \left(1 - \frac{V_{a,2}}{V_{a,1}}\right) \qquad (6-6)$$

$$SR = 1 - \frac{\varepsilon_w^{\gamma} + \left(\frac{1}{V_{a,1}} - 1\right)\sqrt[\frac{\beta}{\gamma}]{\frac{\varepsilon_{AC}^{\beta} - V_{a,1}\varepsilon_a^{\beta}}{(1 - V_{a,1})}} - \frac{1}{V_{a,1}}\varepsilon_{WAC}^{\gamma}}{\left(\varepsilon_w^{\gamma} - \varepsilon_a^{\gamma}\right)} \qquad (6-7)$$

$$MC = \frac{SR \times V_{a,1}}{\left(1 - V_{a,1}\right) \times G_{mm}} \times 100\% \qquad (6-8)$$

$$MC = \frac{1}{G_{mm}}\left[\frac{V_{a,1}}{1-V_{a,1}} - \frac{\varepsilon_w^{\gamma} V_{a,1} + (1-V_{a,1})\sqrt[\frac{\beta}{\gamma}]{\frac{\varepsilon_{AC}^{\beta} - V_{a,1}\varepsilon_a^{\beta}}{(1-V_{a,1})}} - \varepsilon_{WAC}^{\gamma}}{(\varepsilon_w^{\gamma} - \varepsilon_a^{\gamma})(1-V_{a,1})}\right] \times 100\% \qquad (6-9)$$

Given that the dielectric constant of air and moisture remain almost constant in the temperature range for GPR road survey [57], the moisture content prediction model can be further simplified:

$$\begin{cases} \varepsilon_w = 81 \\ \varepsilon_a = 1 \end{cases} \qquad (6-10)$$

$$MC = \frac{1}{G_{mm}}\left[\frac{V_{a,1}}{1-V_{a,1}} - \frac{81^{\gamma} V_{a,1} + (1-V_{a,1})\sqrt[\frac{\beta}{\gamma}]{\frac{\varepsilon_{AC}^{\beta} - V_{a,1}}{(1-V_{a,1})}} - \varepsilon_{WAC}^{\gamma}}{(81^{\gamma} - 1)(1-V_{a,1})}\right] \times 100\% \qquad (6-11)$$

Equation (6-11) is referred to as Leng-Sui (LS) model in this chapter. This model includes six parameters: ε_{WAC}, ε_{AC}, G_{mm}, $V_{a,1}$, β, and γ. Among these, ε_{WAC}, and ε_{AC} can be determined through GPR surveys conducted on dry and wet asphalt pavement, respectively. G_{mm} is a mixture design property that can be obtained from the pavement construction design file. $V_{a,1}$ can either be selected as the target air void content of the whole pavement construction project or predicted from dry GPR data using some widely accepted in-situ density model, such as the ALL model. Therefore, β and γ remain as the only unknown coefficients, whose value will be optimized in the next section using simulation and non-linear regression methods.

6.2 Coefficient Optimization Using Macro-to-Meso-Scale EM Modelling

The optimal value of β and γ can be determined through regression analysis by comparing the moisture content predicted by the LS model with ground truth data. However, obtaining extensive ground truth data directly from in-situ cores is impractical, as drilling is invasive and detrimental to pavement structures. Instead, computer-aided numerical simulations offer an efficient alternative, generating substantial dataset with EM responses closely aligned with real-world applications. In this study, the open-source software gprMax 2D was employed to construct numerical models.

Traditionally, the pavement layer is modelled as a single layer with a uniform dielectric constant, which fails to account for variations caused by different moisture content. To address this limitation, a macro-to-meso-scale EM modelling approach was adopted in this study. A macro-scale asphalt pavement was developed, incorporating the material's meso-scale pore characteristics. The bulk dielectric constant of the asphalt layer was determined by the dielectric constants and volumetric fractions of its individual constituents, rather than being predefined. This approach effectively captures moisture content variations and has been validated, demonstrating accurate simulation results consistent with field data.

6.2.1 Model Establishment

Figure 6.2 illustrates the geometry of the asphalt pavement and the configuration of GPR antenna. A 2-meter-long asphalt layer with a thickness of 10 cm was positioned at the centre of the model region. For wet asphalt pavement cases, a thin metal layer was placed beneath the asphalt layer to provide a clear reflection, mitigating potential ambiguities caused by the dispersive effects of high moisture content. The air-coupled GPR antenna, comprising a transmitter and receiver pair using a Ricker waveform as the excitation source, was positioned 40 cm above the asphalt surface. The GPR antenna moved from 0.4 m to 1.6 m horizontally, resulting in a total survey distance of 1.2 m, while avoiding edge effect. The central frequency of the antenna was set to 2 GHz, matching one of the most used commercial air-coupled horn antennas for pavement condition evaluation. The horizontal sampling rate was set to 250 trace per meter, corresponding to a trace interval of 4 cm. The time sampling rate was automatically calculated by gprMax based on the model geometry and grid resolution. The total time range was set to 12 ns to ensure all key reflections were fully captured and displayed.

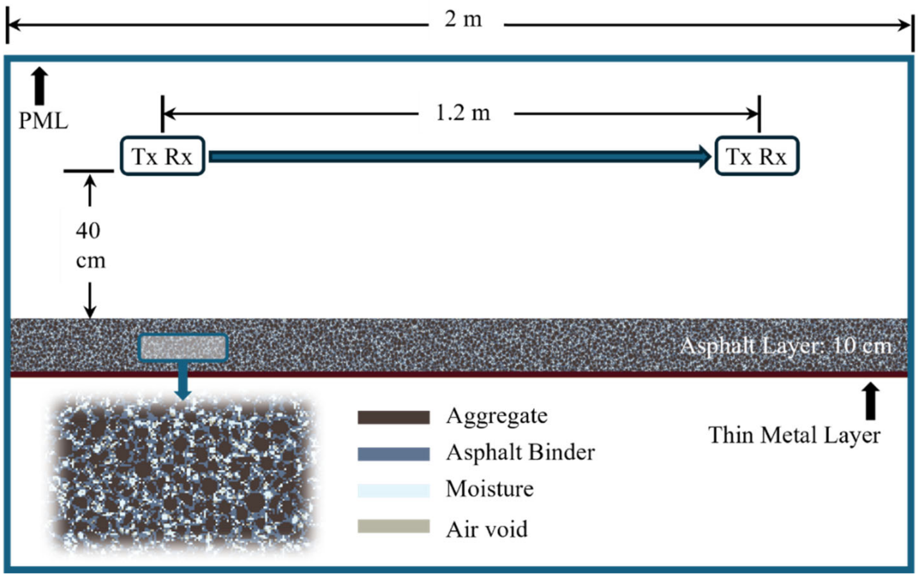

Figure 6.2 Model geometry and GPR antenna configuration

The meso-scale characteristics of the asphalt layer were generated using the same random aggregate generation technique. The process consisted of the following six steps:

1. Define the asphalt layer region and calculate the total number of aggregates in each sieve size based on the model geometry and mix gradation.
2. Randomly generate polygonal coarse aggregate and place them within the defined zone.
3. Go through a verification procedure ensuring that no overlaps occur between aggregates.
4. Define the remaining region as the asphalt binder.
5. Randomly generate polygonal air void within asphalt binder region based on the target air void content.
6. Replace air void regions with moisture at random, based on the target degree of saturation.

In this study, the same 11 types of asphalt mixture in chapter 3 were considered, including AC, SMA, and PA with different NMAS. For each mix type, three parallel models with varying pore structures were generated to eliminate the statistical error. Five air void contents were considered for each mix type, covering the typical range used in field projects. Six saturation degree gradients were applied to capture the EM responses under varying moisture contents. In total, a dataset containing 990 (11×3×5×6) models were created for coefficient optimization, as shown in Figure 6.3

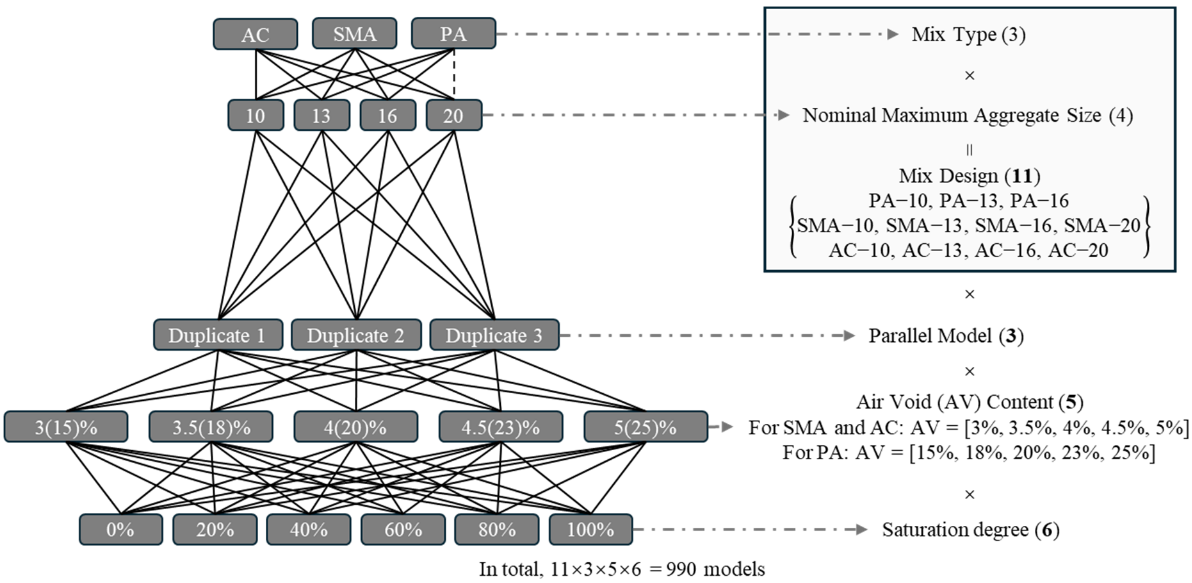

Figure 6.3 Model organization

Table 6.1 summarizes the dielectric property settings for aggregate, asphalt binder, air, and moisture. The dielectric constant values of aggregate and binder was selected based on their typical ranges. However, it is important to note that the dielectric property of moisture cannot be directly predefined as its usual value of 81 in the meso-scale simulations. In gprMax, the effective dielectric constant of the composite is calculated as a weighted average of the individual components, which differs from the true value of a composite governed by EM mixing theory. Using the usual dielectric constant value for moisture can introduce an offset, as verified by various researchers [57, 108]. This offset can be ignored for dry asphalt mixture but not for wet asphalt mixture because of the extremely higher dielectric constant of moisture, as well as the non-negligible dispersive phenomenon.

To address this issue, Lachowicz and Rucka (2019) proposed a solution that involves using a substitute dielectric constant for moisture in EM simulations of meso-scale pore characteristics in porous medium. This substitute value is back-calculated using field core data and the EM mixing theory equation, and its effectiveness has been validated by other studies [57]. Based on their findings, the substitute dielectric constant for moisture was set to 42, with a loss factor (ε_r'') of 4, as the dielectric conductivity of moisture cannot be ignored [57, 108].

Table 6.1 Substitute dielectric constant settings in numerical models

	Aggregate	Asphalt Binder	Air	Moisture
Dielectric constant	6	3	1	42
Loss factor	0	0	0	4

6.2.2 Evaluation Matrix

The dielectric constant profile of both the dry and the wet asphalt layer was calculated using the TOF method, which takes the material heterogeneity along depth into account and can be seen as the ground truth data. A non-linear least square curve fitting was utilized to find the optimal β and γ by minimizing the root mean square error (RMSE) between the MC predicted using the proposed LS model and the ground truth MC:

$$(\beta_{opt}, \gamma_{opt}) = \underset{\beta,\gamma}{argmin} \sqrt{\frac{1}{N}\sum_{i=1}^{N}\left(MC_{predicted}(i,\beta,\gamma) - MC_{ground\ truth}(i)\right)^2} \qquad (6-12)$$

where $MC_{predicted}(i,\beta,\gamma)$ is the predicted moisture content using the proposed LS model; $MC_{ground\ truth}(i)$ is the ground truth moisture content calculated using equation 12 and the input saturation degree, and N is the number of models for each case, which equals to 300 for AC and SMA mixture and 240 for PA mixture.

6.2.3 Coefficient Optimization Result

A decoupling process was applied to the raw GPR data to remove the direct coupling pulse, which can obscure the pavement reflections of interest. The decoupled GPR A-scan and B-scan radargrams for asphalt pavements with different moisture content (saturation degrees) are shown in Figure 6.4. The surface and bottom reflections of the asphalt layer are clearly identifiable, and the TWTT increases with higher moisture content. Additionally, the amplitude of the bottom reflection decreases as moisture content increases, indicating signal attenuation caused by the presence of moisture. This phenomenon is also evident in the B-scan radargram, where the second reflection becomes increasingly blurred. For the PA mixture, the bottom reflection of the pavement structure becomes undetectable when the saturation degree reaches 100%. Therefore, only 240 wet models were used for PA mixture coefficient optimization, compared to 300 models used for AC and SMA mixtures.

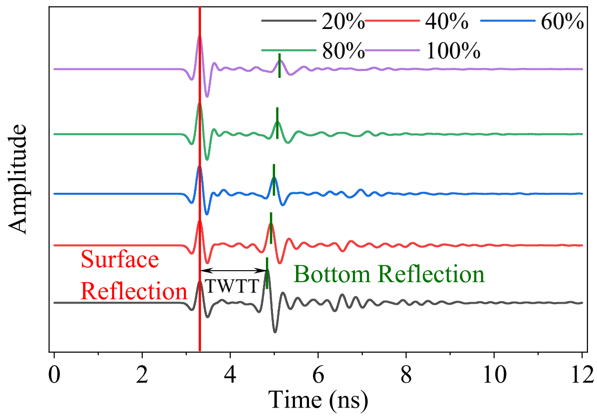

(a)

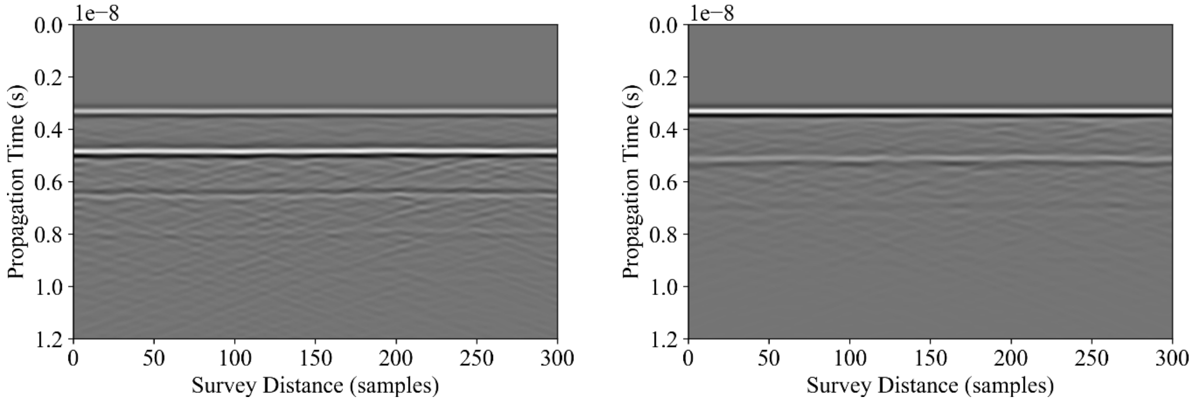

(b) (c)

Figure 6.4 Decoupled GPR A-scan and B-scan for asphalt concrete with different saturation degree: (a) A-scan with saturation degree from 20% to 100%; (b) B-scan (saturation degree equals 20%); (c) B-scan (saturation degree equals 100%)

The bulk dielectric constant of asphalt pavement at each moisture content level was calculated, as shown in Figure 6.5. The relationship between the bulk dielectric constant and the moisture content exhibited strong linearity across all three types of asphalt mixtures. A relatively higher deviation was observed in the PA mixture, indicating greater variability in the bulk dielectric constant of the mixture at higher internal moisture levels. This can be attributed to increased EM energy attenuation caused by the higher dielectric conductivity of moisture [109]. These results validate the effectiveness of the macro-to-meso-scale EM modelling approach, as both the observed linearity and the deviations caused by energy attenuation were accurately captured.

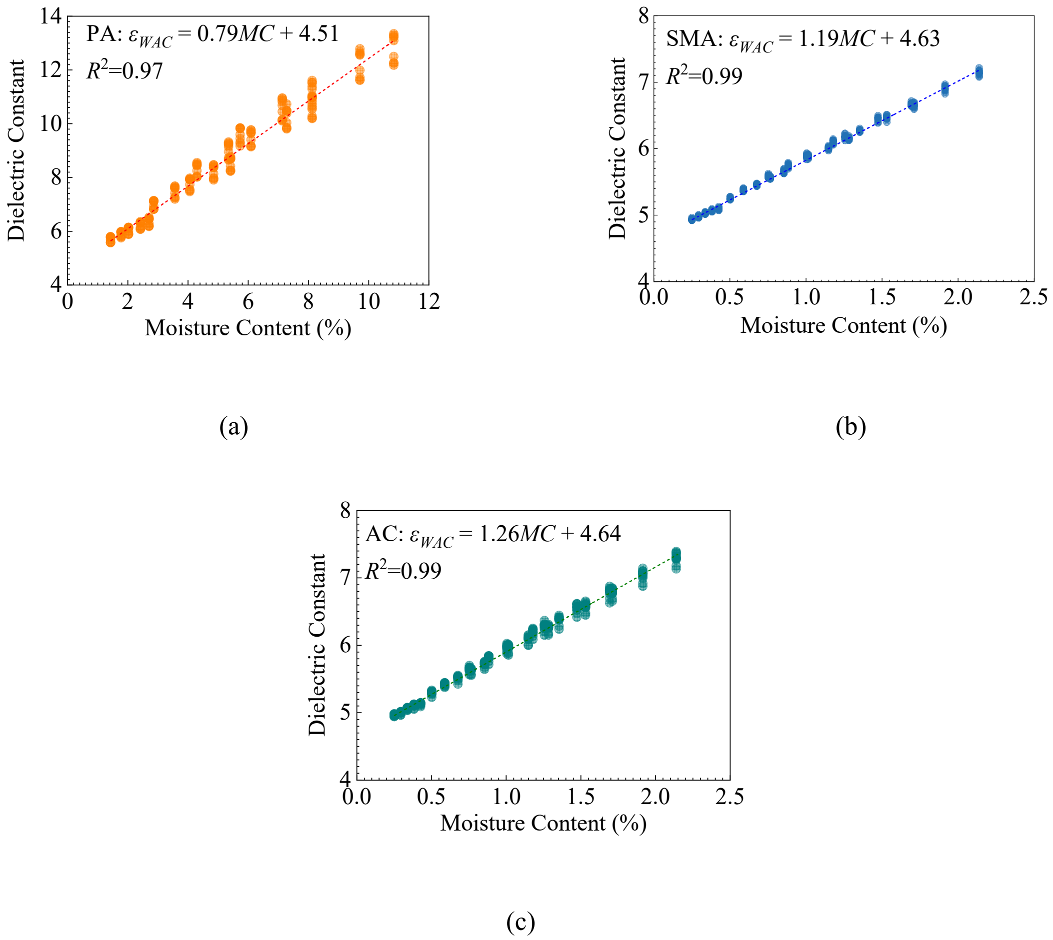

Figure 6.5 Relationship between moisture content and dielectric constant of wet asphalt mixtures: (a) PA; (b) SMA; (c) AC

The optimal coefficient for the proposed LS model were determined using the non-linear least square curve fitting method, as described in Equation (6-12). Through minimizing the RMSE, the optimal values of β and γ were found to be 0.23 and 0.47 for the PA mixture, 1.28 and 0.73 for the SMA mixture, and 1.35 and 0.76 for the AC, as illustrated in Figure 6.6. By substituting these values of β and γ into Equation (6-11), the final LS model equations were established for PA, SMA, and AC mixture, as shown in Equation (6-13) to (6-15). The performance of the LS models will be evaluated in the following section using laboratory testing data.

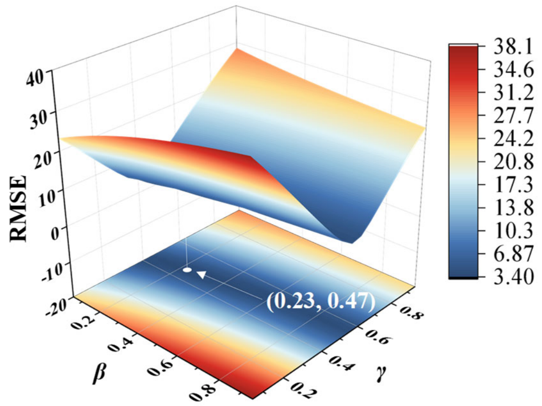

(a)

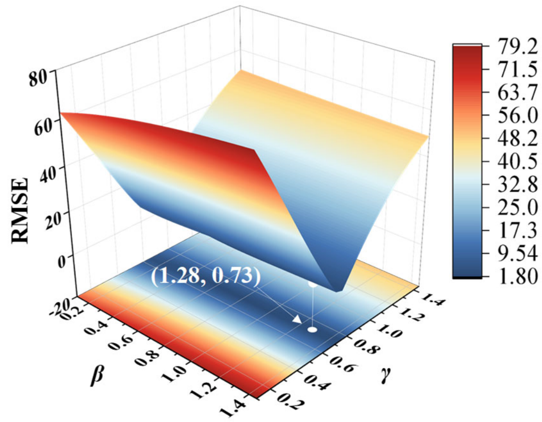

(b)

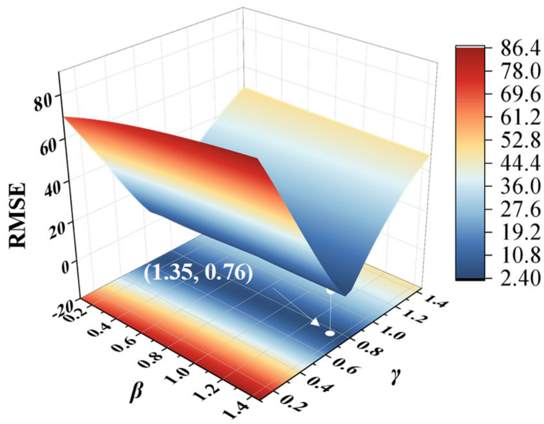

(c)

Figure 6.6 RMSE under different β and γ value and the optimum coefficient combination for different mix types: (a) PA; (b) SMA; (c) AC

$$MC = \frac{1}{G_{mm}}\left[\frac{V_{a,1}}{1-V_{a,1}} - \frac{7.89V_{a,1} + \left(1-V_{a,1}\right)^{0.49}\sqrt{\frac{\varepsilon_{AC}^{0.23}-V_{a,1}}{(1-V_{a,1})}} - \varepsilon_{WAC}^{0.47}}{6.89\left(1-V_{a,1}\right)}\right] \times 100\% \qquad (6-13)$$

$$MC = \frac{1}{G_{mm}}\left[\frac{V_{a,1}}{1-V_{a,1}} - \frac{24.73V_{a,1} + \left(1-V_{a,1}\right)^{1.75}\sqrt{\frac{\varepsilon_{AC}^{1.28}-V_{a,1}}{(1-V_{a,1})}} - \varepsilon_{WAC}^{0.73}}{23.73\left(1-V_{a,1}\right)}\right] \times 100\% \qquad (6-14)$$

$$MC = \frac{1}{G_{mm}}\left[\frac{V_{a,1}}{1-V_{a,1}} - \frac{28.21V_{a,1} + \left(1-V_{a,1}\right)^{1.77}\sqrt{\frac{\varepsilon_{AC}^{1.35}-V_{a,1}}{(1-V_{a,1})}} - \varepsilon_{WAC}^{0.76}}{27.21\left(1-V_{a,1}\right)}\right] \times 100\% \qquad (6-15)$$

6.3 Laboratory Test Validation

Laboratory tests on SGC specimens were conducted to validate the performance of the proposed LS model. A total of 22 SGC specimens, each with a diameter of 150 mm, were prepared to represent major gradations of asphalt mixtures, including three types of PA, four types of AC, and four types of SMA. The mass of each specimen was first measured in air. Subsequently, all specimens were placed in a vacuum chamber filled with water to facilitate the water penetration, as illustrated in Figure 6.5. Afterward, the water content was determined by measuring the mass of surface-dry wet specimens. To prevent water from escaping from the wet PA mixture during mass measurements and GPR data collection, an ultra-thin parafilm was tightly wrapped around the periphery and bottom surface of the PA specimens.

(a) (b)

Figure 6.7 Moisture penetration procedure: (a) vacuum chamber; (b) specially wrapped PA mixture

Key parameters for each specimen, including the serial number (mixture type), specimen height, air void content, G_{mm}, and ground truth moisture content, are provided in Table 6.2. G_{mm} is measured for each mix type using loose aggregate coated with asphalt binder. G_{mb} of AC and SMA mixture were measured using the SSD method, and the G_{mb} of PA mixture was measured using the CoreLok method. AV was then calculated as follows:

$$AV = \left(1 - \frac{G_{mb}}{G_{mm}}\right) \times 100 \qquad (6-16)$$

Table 6.2 Geometry and ground truth moisture content of SGC specimens

Sample No.	Height (cm)	Air void content (%)	G_{mm}	Moisture content (%)
PA10_1	8.8	22.37	2.423	3.85
PA10_2	8.5	22.58	2.423	4.00
PA13_1	8.7	17.63	2.451	3.10
PA13_2	8.6	18.36	2.451	3.07
PA16_1	9.5	20.47	2.440	3.05
PA16_2	8.5	21.29	2.440	2.81
SMA10_1	9.0	3.41	2.402	0.55
SMA10_2	8.7	3.47	2.402	0.57
SMA13_1	8.5	4.00	2.416	0.78
SMA13_2	9.0	4.61	2.416	0.84
SMA16_1	8.8	3.86	2.402	0.99
SMA16_2	8.8	3.91	2.402	0.91
SMA20_1	8.7	2.18	2.430	0.35
SMA20_2	8.8	2.37	2.430	0.35
AC10_1	9.0	4.65	2.406	0.66
AC10_2	8.5	3.89	2.406	0.62
AC13_1	8.6	5.32	2.420	1.01
AC13_2	8.9	5.86	2.420	1.17
AC16_1	9.0	4.44	2.461	0.79
AC16_2	8.6	3.41	2.461	0.66
AC20_1	8.8	4.04	2.440	0.72
AC20_2	8.9	4.11	2.440	0.65

GPR measurements were conducted for both dry and wet specimens using a GSSI 2GHz palm antenna in a spacer-inserted configuration. Data collection followed the same procedure in chapter 5. The MC prediction results are presented in Figure 6.8, where the performance of the proposed LS model is compared with the MISO model and the ACA model. The absolute MC prediction error was used as the evaluation metric instead of relative error. This choice was made because the MC in asphalt mixture often remains at a low value, particularly in mixtures with low air void content and low permeability, such as AC and SMA. The results show that the proposed LS model significantly outperformed the other two models, achieving the lowest average MC prediction error of 0.210% across the 22 tested SGC samples. In comparison, the ACA model and the MISO model yielded higher average errors of 0.783% and 1.630%, respectively.

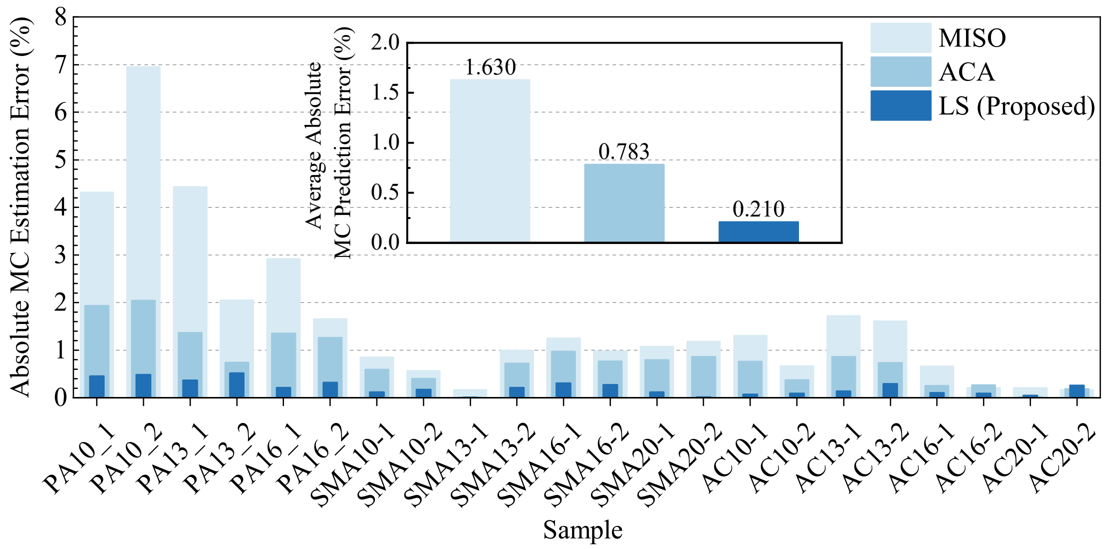

Figure 6.8 MC prediction performance between the proposed LS model, and the MISO model and the ACA model

The proposed LS model demonstrates improved MC prediction accuracy across all three types of asphalt mixtures, with particularly significant improvements observed for PA mixtures. For instance, the average MC prediction error for PA mixtures was 0.391% with the LS model, compared to 1.446% for the ACA model and 3.718% for the MISO model. This enhanced performance can be attributed to differences in the underlying EM mixing model used for derivation. Both the ACA model and the MISO model are based on the modified Bottcher model, which incorporates a shape factor to account for deviations from the spherical assumption of the mixture inclusions. However, this shape factor is typically calibrated using data from a limited number of laboratory samples or drilled in-situ cores. Therefore, the calibrated shape factor might not be optimal. Additionally, these models perform reasonably well for dense-graded asphalt mixtures, they tend to produce higher estimation error when applied to open-graded mixtures, as demonstrated by field data from various projects.

In contrast, the LS model in this study was derived using the general power-law EM mixing theory rather than the modified Bottcher model. The two key power indices, β and γ, were determined separately for each mix type through non-linear regression applied to a large volume of simulated data, which closely aligns with field ground truth data. This data-driven approach effectively reduces multi-source errors within the model through statistical optimization. Consequently, the LS model demonstrates enhanced accuracy, particularly for PA mixtures, which are more likely to exhibit higher MC values due to their higher amount of connected air void channels.

A flowchart can be summarized for MC quantification in asphalt pavement using the proposed LS model and GPR in field applications, as illustrated in Figure 6.9. Main steps include:

1. Collect mix design from the project information and select the LS model according to the corresponding mix type (PA, SMA or AC).
2. Conduct GPR survey on sunny days after pavement construction, obtaining dielectric constant of dry asphalt mixture (ε_{AC}). Calculate the air void profile using ALL model ($V_{a,1}$).
3. Conduct GPR surveys on wet asphalt pavement after rainfall events when pavement surface is dry, obtaining dielectric constant of wet asphalt mixture (ε_{WAC}). Calculate the moisture content using LS model.

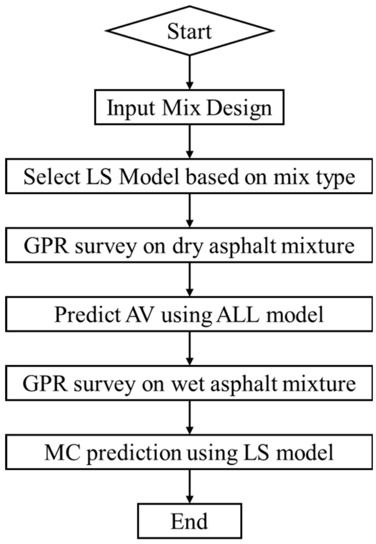

Figure 6.9 Flowchart of MC prediction using LS model for field project

6.4 Summary

This chapter proposed a novel moisture content prediction model, termed the LS model, grounded in the general power-law EM mixing theory and the dielectric constant profiles measured using GPR. Key parameters of the model were optimized using FDTD simulation data, incorporating a macro-to-meso-scale EM modelling technique. The moisture content prediction performance of the proposed model was validated through controlled laboratory tests on SGC specimens. Main findings are drawn as follows:

(1) By integrating GPR surveys with the proposed model, the in-situ moisture content of asphalt pavement can be accurately determined in a non-destructive and real-time manner. The macro-to-meso-scale EM modelling approach effectively simulates the GPR-pavement system, yielding EM responses closely aligned with to real-world conditions. This approach addresses the challenge of limited field GPR data and supports the coefficient optimization process for the LS model.

(2) The optimal values of the power indices β and γ were determined as follows: 0.23 and 0.47 for PA mixture, 1.28 and 0.73 for SMA mixture, and 1.35 and 0.76 for AC mixture,

respectively, using a non-linear least square curve fitting approach. Laboratory tests demonstrated that the proposed LS model achieved an average absolute moisture content prediction error of 0.21%, significantly outperforming the MISO model (1.63%), and the ACA model (0.78%).

(3) A workflow of MC prediction using the proposed LS model was recommended, including information collection from mix design, LS model selection based on mis type, air void content prediction of dry mixtures using ALL model, GPR surveys on both dry and wet mixtures, as well as final MC calculations using LS model. This workflow can be utilized to quantify MC in field applications, such as MC determination in cold in-place recycling mixtures, or MC prediction of asphalt pavement after rainfalls.

CHAPTER 7 FINDINGS, CONCLUSIONS, AND RECOMMENDATIONS

This study aims to enhance the accuracy of volumetric property predictions in flexible and semi-flexible pavement QA programs using GPR by proposing and validating innovative models and methodologies. Specifically, it aims to address four key research gaps: (1) inaccuracies in in-situ density prediction caused by the homogeneous materials assumption, (2) the inability to achieve multi-layer thickness profiling due to vibration effects, (3) limitations in existing MC prediction models, and (4) the absence of a grouting rate prediction model for SFP. To tackle these challenges, a modified ALL model is proposed for in-situ density prediction, effectively eliminating dielectric constant estimation errors through the use of the SR method. Additionally, an HC-SR method is introduced for multi-asphalt-layer thickness profiling, mitigating vibration effects caused by antenna shifting and swaying. A novel LS model is developed for MC prediction in flexible pavements, utilizing an authentic simulation of meso-scale pore structures. For SFP grouting rate prediction, a novel LWS model and its corresponding QA procedure are proposed.

7.1 Findings and Conclusions

The following key findings have been obtained based on the outcomes of this study:

1. For in-situ density prediction using the proposed modified ALL model, the optimal random pore distribution coefficients for AC, SMA, and PA mixtures were determined as 0.966, 0.964, and 0.926, respectively, using a non-linear regression algorithm. This improved bulk specific gravity prediction accuracy by 1.9%, 2.7%, and 6.7%, respectively.
2. The coefficient for PA mixtures exhibited a positive correlation with air void content, while remaining invariant for SMA and AC mixtures. Antenna-surface height influenced predicted dielectric constant profiles but can be statistically neglected on

the proposed coefficient due to the compensatory effect of under- and overestimations.

3. The relationship between antenna-surface height and reflection amplitude followed a third-order polynomial law, outperforming other models (e.g., power, exponential, and inverted laws), particularly for interface reflection amplitudes.
4. The proposed HC-SR method effectively removed vibration effects caused by antenna movement, significantly smoothing the thickness profile. The GPR-based thickness estimation error was reduced by 13.3%, 19.9%, and 17.4% for the first, second, and entire asphalt layers, respectively, compared to the traditional SR method.
5. It is recommended to implement bouncing tests on both the pavement and a copper plate in real applications and to replace traditional SR methods with the HC-SR method for dielectric constant estimation. The use of air-coupled antennas with central frequencies above 1 GHz is also advised.
6. The proposed workflow improves GPR-based thickness determination accuracy without significantly increasing on-site preparation time, as the HC-SR method can be pre-programmed into post-processing steps.
7. By integrating GPR surveys with the proposed LS model, in-situ MC of asphalt pavement can be accurately determined in a non-destructive and real-time manner. The macro-to-meso-scale EM modelling approach effectively simulated the GPR-pavement system, producing results closely aligned with real-world conditions.
8. Optimal power indices β and γ in proposed LS model were determined as 0.23 and 0.47 for PA mixtures, 1.28 and 0.73 for SMA mixtures, and 1.35 and 0.76 for AC mixtures, respectively, using non-linear least square curve fitting. Laboratory tests demonstrated the LS model's superior accuracy, with an average absolute MC

prediction error of 0.2%, outperforming the MISO model (1.6%) and the ACA model (0.8%).

9. A comprehensive workflow for MC prediction using the proposed LS model was recommended. This includes collecting mix design data, selecting appropriate LS models based on mixture type, predicting air void content of dry mixtures using the ALL model, conducting GPR surveys on both dry and wet mixtures, and calculating final MC values using the LS model.
10. Meso-scale numerical simulations revealed a convex correlation between the estimation error of the LWS model and the actual grouting rate, with a peak error margin of less than 6% at a 50% grouting rate. This error margin decreased to 4% when the grouting rate exceeded 80%. Laboratory tests recorded an average estimation error below 7%.
11. The prediction accuracy of the LWS model mainly depended on the estimation dielectric constants of the PA matrix and the SFP. The initial air void content in the PA matrix and the dielectric constant of the cement grout were identified as crucial factors influenced by these dielectric constants. To enhance model precision, the power indices β and γ should be calibrated to 0.33 instead of the conventional value of 0.5.
12. Two key practices for improving accuracy include removing excess cement slurry post-grouting and deferring GPR measurements until the SFP has cured. For traffic-speed surveys, high-frequency air-coupled horn antennas are recommended to ensure operational efficiency without disrupting the SFP construction schedule.

Based on the findings listed above, the following general conclusions have been drawn:

1. The modified ALL model significantly enhances in-situ density prediction accuracy using GPR, making it a more reliable tool for flexible pavement QA programs.

2. The HC-SR method improves multi-layer asphalt thickness determination accuracy by eliminating vibration effects, ensuring higher profiling precision.
3. The LS model provides accurate, non-destructive, real-time MC predictions for flexible pavements, with applications in cold in-place recycling mixtures and post-rainfall MC assessments.
4. The LWS model, combined with the proposed QA procedure, accurately estimates the in-situ grouting rate of SFP, enabling effective quality control during construction.

7.2 Recommendations for Future Research

As the application of GPR as a reliable NDT method for QA programs in flexible and semi-flexible pavements is still an emerging field, further research should address the following areas to enhance volumetric property prediction accuracy and broaden GPR's applicability:

1. Evaluate the performance of the modified ALL model using air-coupled antennas with central frequencies other than 2 GHz. Additionally, explore the influence of aggregate dielectric constants on in-situ density predictions.
2. Investigate advanced image processing algorithms to improve thickness profiling accuracy in cases where low dielectric contrast between adjacent asphalt layers renders interface reflections invisible.
3. Enhance the LS model to address energy attenuation effects at extremely high moisture content levels, improving its applicability across a broader range of field conditions.
4. Refine the power indices of the proposed LWS model to account for the effects of fluctuating moisture contents during the curing process of SFP.

REFERENCES

[1] H. L. Von Quintus (2009). *NDT technology for quality assurance of HMA pavement construction* (Vol. 626). Transportation Research Board.

[2] W. W. L. Lai, X. Derobert, and A. P. Annan (2018). A review of Ground Penetrating Radar application in civil engineering: A 30-year journey from Locating and Testing to Imaging and Diagnosis. *NDT & E International*, *96*, 58-78.

[3] J. L. Davis, and A. P. Annan (1989). Ground-penetrating radar for high-resolution mapping of soil and rock stratigraphy 1. *Geophysical prospecting*, *37*(5), 531-551.

[4] D. J. Daniels (2004). *Ground penetrating radar* (Vol. 1). London: The Institute of Engineering and Technology.

[5] A. Sihvola, and I. V. Lindell (1989). Polarizability and effective permittivity of layered and continuously inhomogeneous dielectric spheres. *Journal of electromagnetic waves and applications*, *3*(1), 37-60.

[6] I. L. Al-Qadi, S. Lahouar, and A. Loulizi (2003). Successful application of ground-penetrating radar for quality assurance-quality control of new pavements. *Transportation research record*, *1861*(1), 86-97.

[7] A. Loizos, and C. Plati (2007). Accuracy of pavement thicknesses estimation using different ground penetrating radar analysis approaches. *NDT & e International*, *40*(2), 147-157.

[8] Q. Cao, and I. L. Al-Qadi (2021). Signal stability and the height-correction method for ground-penetrating radar in situ asphalt concrete density prediction. Transportation Research Record, 2675(9), 835-847.

[9] Z. Leng, I. L. Al-Qadi, P. Shangguan, and S. Son (2012). Field application of ground-penetrating radar for measurement of asphalt mixture density: case study of Illinois route 72 overlay. *Transportation research record*, *2304*(1), 133-141.

[10] L. Abufares, U. M. Ali, Q. Cao, S. Wang, X. Sui, and I. L. Al-Qadi (2021). GPR application for moisture content prediction of cold in-place recycling. In *Airfield and Highway Pavements 2021* (pp. 231-239).

[11] M. L. Afonso, M., Dinis-Almeida, L. A. Pereira-de-Oliveira, J. Castro-Gomes, and S. E. Zoorob (2016). Development of a semi-flexible heavy duty pavement surfacing incorporating recycled and waste aggregates–Preliminary study. *Construction and Building Materials*, *102*, 155-161.

[12] P. Cihackova, P. Hyzl, D. Stehlik, O. Dasek, O. Šernas, and A. Vaitkus (2015). Performance characteristics of the open-graded asphalt concrete filled with a special cement grout. *The Baltic Journal of Road and Bridge Engineering*, *10*(4), 316-324.

[13] A. Hassani, M. Taghipoor, and M. M. Karimi (2020). A state of the art of semi-flexible pavements: Introduction, design, and performance. *Construction and Building Materials*, *253*, 119196.

[14] Y. Mehta, and R. Roque (2003). Evaluation of FWD data for determination of layer moduli of pavements. *Journal of Materials in Civil Engineering*, *15*(1), 25-31.

[15] B. Umashankar, C. Hariprasad, and G. T. Kumar (2016). Compaction quality control of pavement layers using LWD. *Journal of Materials in Civil engineering*, *28*(2), 04015111.

[16] H. Azari, and S. Lin (2019). Evaluation of the impact echo method for concrete bridge decks with asphalt overlays. *Transportation research record*, *2673*(2), 436-444.

[17] J., Norambuena-Contreras, Castro- D. Fresno, A. Vega-Zamanillo, M. Celaya, and I. Lombillo-Vozmediano (2010). Dynamic modulus of asphalt mixture by ultrasonic direct test. *Ndt & E International*, *43*(7), 629-634.

[18] J. S. Heisey, K. H. Stokoe, and A. H. Meyer (1982). Moduli of pavement systems from spectral analysis of surface waves. *Transportation research record*, *852*(22-31), 147.

[19] H. M. Jol (Ed.). (2008). *Ground penetrating radar theory and applications*. elsevier.

[20] S. Wang, X. Sui, Z. Leng, J. Jiang, and G. Lu (2022). Asphalt pavement density measurement using non-destructive testing methods: Current practices, challenges, and future vision. *Construction and building materials*, *344*, 128154.

[21] F. Liu, J. Liu, and L. Wang (2022). Asphalt pavement crack detection based on convolutional neural network and infrared thermography. *IEEE Transactions on Intelligent Transportation Systems*, *23*(11), 22145-22155.

[22] X. Zhang, T. Liu, C. Liu, and Z. Chen (2014). Research on skid resistance of asphalt pavement based on three-dimensional laser-scanning technology and pressure-sensitive film. *Construction and Building Materials*, *69*, 49-59.

[23] G. K. Chang, Q. Xu, J. L. Rutledge, and S. I. Garber (2014). *A study on intelligent compacting and in-place asphalt density* (No. FHWA-HIF-14-017). United States. Federal Highway Administration. Office of Pavement Technology.

[24] A. P. Annan (2025). Chapter 11: Ground-penetrating radar. *Near-surface Geophysics*, edited by Dwain K. Butler, 357-438. Tulsa, Oklahoma: Society of Exploration Geophysicists.

[25] C. A. Balanis (1999). *Advanced engineering electromagnetics*. John Wiley & Sons. New York.

[26] A. Benedetto, and L. Pajewski (2015). *Civil engineering applications of ground penetrating radar*. Springer. New York.

[27] GSSI Antenna Manual, 2017. https://www.geophysical.com/wpcontent/uploads/2017/10/GSSI-Antenna-Manual.pdf.

[28] T. Aschenbrener, and N. Tran (2020). Optimizing in-place density through improved density specifications. *Transportation Research Record*, *2674*(3), 211-218.

[29] C. S. Hughes (1989). *Compaction of asphalt pavement (No. 152): Compaction of asphalt pavement*. Transportation Research Board. National Research Council. Washington, DC.

[30] B. M. Killingsworth (2004). *Quality Characteristics for Use with Performance Related Specifications for Hot Mix Asphalt. Research results digest*, *291*. Transportation Research Board. National Research Council. Washington, DC.

[31] T. Saarenketo, and T. Scullion (2000). Road evaluation with ground penetrating radar. *Journal of applied geophysics*, *43*(2-4), 119-138.

[32] K. R. Maser, T. Scullion, and R. C. Briggs (1991). Use of radar technology for pavement layer evaluation. *NASA STI/Recon Technical Report N*, *93*, 21744.

[33] S. Lahouar (2003). *Development of data analysis algorithms for interpretation of ground-penetrating radar data*. Virginia Polytechnic Institute and State University.

[34] K. Hoegh, L. Khazanovich, S. Dai, and T. Yu (2015). Evaluating asphalt concrete air void variation via GPR antenna array data. *Case Studies in Nondestructive Testing and Evaluation*, *3*, 27-33.

[35] K. Hoegh, S. Dai, T. Steiner, and L. Khazanovich (2018). Enhanced model for continuous dielectric-based asphalt compaction evaluation. *Transportation Research Record*, *2672*(26), 144-154.

[36] Z. Leng, I. L. Al-Qadi, and S.Lahouar (2011). Development and validation for in situ asphalt mixture density prediction models. *NDT & e International*, *44*(4), 369-375.

[37] Z. Leng (2011). *Prediction of in-situ asphalt mixture density using ground penetrating radar: theoretical development and field verification*. University of Illinois at Urbana-Champaign.

[38] X. Xiong, S. Xiao, Y. Tan, X. Zhang, D. Zhang, M. Han, and W. Wang (2021). Estimation of density and moisture content in asphalt mixture based on dielectric property. *Construction and Building Materials*, *298*, 123518.

[39] K. R. Maser, T. J. Holland, R. Roberts, and J. Popovics (2006). NDE methods for quality assurance of new pavement thickness. *The International Journal of Pavement Engineering*. *7(1)* pp. 1-10, https://doi.org/10.1080/10298430500501985.

[40] R. S. McDaniel (2019). *Impact of asphalt thickness on pavement quality. No. Project 20-05 Topic 49-05.* Washington, DC: The National Academies Press. https://doi.org/10.17226/25498.

[41] C. Plati, A. Loizos, and K. Gkyrtis (2020). Assessment of modern roadways using non-destructive geophysical surveying techniques. *Surveys in Geophysics*. *41(3)*. pp. 395-430, https://doi.org/10.1007/s10712-019-09518-y.

[42] M. Solla, V. Pérez-Gracia, and S. Fontul (2021). A review of GPR application on transport infrastructures: troubleshooting and best practices. *Remote Sensing. 13(4)* 672, https://doi.org/10.3390/rs13040672.

[43] A. Benedetto, F. Tosti, L. B. Ciampoli, and F. D'amico (2017). An overview of ground-penetrating radar signal processing techniques for road inspections. *Signal processing*, *132*, 201-209.

[44] P. Shangguan, I. L. Al-Qadi, Z. Leng, R. L. Schmitt, and A. Faheem (2013). Innovative approach for asphalt pavement compaction monitoring with ground-penetrating radar. *Transportation research record*, *2347*(1), 79-87.

[45] S. Wang, and I. L. Al-Qadi (2021). Impact and removal of ground-penetrating radar vibration on continuous asphalt concrete pavement density prediction. *IEEE Transactions on Geoscience and Remote Sensing*, *60*, 1-14.

[46] W. He, T. Hao, H. Ke, W. Zheng, and K. Lin (2020). Joint time-frequency analysis of ground penetrating radar data based on variational mode decomposition. *Journal of Applied Geophysics*, *181*, 104146.

[47] H. Zhou, X. Feng, Z. Dong, C. Liu, and W. Liang (2022). Diffraction Suppression for Ground Penetrating Radar Data Using FX Domain Variational Mode Decomposition. In *IGARSS 2022-2022 IEEE International Geoscience and Remote Sensing Symposium* (pp. 2107-2110). IEEE.

[48] K. Maser (2020). Measurement of as-built conditions using ground penetrating radar. In *Structural Materials Technology* (pp. 61-67). CRC Press.

[49] T. Scullion, and Y. Chen (1992). Implementation of the Texas ground penetrating radar system.

[50] A. Frid, and V. Frid (2018). Irregular changes in antenna height during high-speed scanning as a source of essential errors in measuring the thickness of asphalt. In *2018 17th International Conference on Ground Penetrating Radar (GPR)* (pp. 1-4). IEEE.

[51] M. E. Kutay, and A. H. Aydilek (2009). Pore pressure and viscous shear stress distribution due to water flow within asphalt pore structure. *Computer-Aided Civil and Infrastructure Engineering*, *24*(3), 212-224.

[52] M. R. Kakar, M. O. Hamzah, and J. Valentin (2015). A review on moisture damages of hot and warm mix asphalt and related investigations. *Journal of Cleaner Production*, *99*, 39-58.

[53] R. L. Schmitt, J. S. Russell, A. S. Hanna, H. U. Bahia, and G. A. Jung (1998). Summary of current quality control/quality assurance practices for hot-mix asphalt construction. *Transportation Research Record*, *1632*(1), 22-31.

[54] J. A. Huisman, S. S. Hubbard, J. D. Redman, and A. P. Annan (2003). Measuring soil water content with ground penetrating radar: A review. *Vadose zone journal*, *2*(4), 476-491.

[55] A. Benedetto, and F. Benedetto (2011). Remote sensing of soil moisture content by GPR signal processing in the frequency domain. *IEEE Sensors Journal*, *11*(10), 2432-2441.

[56] G. C. Topp, J. L., Davis, and A. P. Annan (1980). Electromagnetic determination of soil water content: Measurements in coaxial transmission lines. *Water resources research*, *16*(3), 574-582.

[57] Q. Cao, and I. L. Al-Qadi (2021). Effect of moisture content on calculated dielectric properties of asphalt concrete pavements from ground-penetrating radar measurements. *Remote Sensing*, *14*(1), 34.

[58] L. Abufares, Q. Cao, and I. L. Al-Qadi (2023). Model development for moisture content and density prediction for non-dry asphalt concrete using GPR data. *International Journal of Pavement Engineering*, *24*(1), 2189720.

[59] M. L Afonso, M. Dinis-Almeida, L. A. Pereira-de-Oliveira, J. Castro-Gomes, and S. E. Zoorob (2016). Development of a semi-flexible heavy duty pavement surfacing incorporating recycled and waste aggregates–Preliminary study. *Construction and Building Materials. 102,* pp.155-161.

[60] P. Cihackova, P. Hyzl, D. Stehlik, O. Dasek, O. Šernas, and A. Vaitkus (2015). Performance characteristics of the open-graded asphalt concrete filled with a special cement grout. *The Baltic Journal of Road and Bridge Engineering. 10(4),* pp. 316-324.

[61] T. Q. Ling, Z. J. Zhao, C. H. Xiong, Y. Y. Dong, Y. Y. Liu, and Q. Dong (2009). The application of semi-flexible pavement on heavy traffic roads. *International Journal of Pavement Research and Technology*. *2(5),* pp. 211-217.

[62] B. Yang, and X. Weng (2015). The influence on the durability of semi-flexible airport pavement materials to cyclic wheel load test. *Construction and Building Materials*. *98,* pp, 171-175.

[63] X. Cai, J. Yang, X. Chen, J. Zhang, and H. Zhang (2020). Interlocking property evaluation of dual skeleton in semi-flexible pavement material by micromechanical model and X-ray computed tomography. *Construction and Building Materials*. *254,* 118934.

[64] M. Gong, Z. Xiong, H. Chen, C. Deng, X. Chen, J. Yang, and J. Hong (2019). Evaluation on the cracking resistance of semi-flexible pavement mixture by laboratory research and field validation. *Construction and Building Materials*. *207,* pp. 387-395.

[65] J. Cai, J. Pei, Q. Luo, J. Zhang, R. Li, and X. Chen (2017). Comprehensive service properties evaluation of composite grouting materials with high-performance cement paste for semi-flexible pavement. *Construction and Building Materials*. *153,* pp. 544-556.

[66] S. Luo, X. Yang, K. Zhong, and J. Yin (2020). Open-graded asphalt concrete grouted by latex modified cement mortar. *Road Materials and Pavement Design*. *21(1),* pp. 61-77.

[67] S. An, C. Ai, D. Ren, A. Rahman, and Y. Qiu (2018). Laboratory and field evaluation of a novel cement grout asphalt composite. *Journal of Materials in Civil Engineering*. *30(8),* 04018179.

[68] A. Hassani, M. Taghipoor, and M. M. Karimi (2020). A state of the art of semi-flexible pavements: Introduction, design, and performance. *Construction and Building Materials*. *253,* 119196.

[69] I. L. Al-Qadi, H. Gouru, and R. E. Weyers (1994). Asphalt Portland cement concrete composite: laboratory evaluation. *Journal of transportation engineering*. *120(1),* pp. 94-108.

[70] A. Corradini, G. Cerni, A. D'Alessandro, and F. Ubertini (2017). Improved understanding of grouted mixture fatigue behavior under indirect tensile test configuration. *Construction and Building Materials*. *155,* pp. 910-918.

[71] X. Cai, L. Fu, J. Zhang, X. Chen, and J. Yang (2020). Damage analysis of semi-flexible pavement material under axial compression test based on acoustic emission technique. *Construction and Building Materials*. *239,* 117773.

[72] S. Hou, T. Xu, and K. Huang (2017). Aggregate gradation influence on grouting results and mix design of asphalt mixture skeleton for semi-flexible pavement. *Journal of Testing and Evaluation*. *45(2),* pp. 591-600.

[73] G. Bharath, M. Shukla, M. N. Nagabushana, S. Chandra, and A. Shaw (2020). Laboratory and field evaluation of cement grouted bituminous mixes. *Road Materials and Pavement Design*. *21(6),* pp. 1694-1712.

[74] X. Cai, H. Zhang, J. Zhang, X. Chen, J. Yang, and J. Hong (2019). Investigation on reinforcing mechanisms of semi-flexible pavement material through micromechanical model. *Construction and building materials*. *198,* pp. 732-741.

[75] J. Pei, J. Cai, D. Zou, J. Zhang, R. Li, X. Chen, and L. Jin (2016). Design and performance validation of high-performance cement paste as a grouting material for semi-flexible pavement. *Construction and Building Materials*. *126,* pp. 206-217.

[76] C.J.F. Böttcher, O. C. van Belle, P. Bordewijk, A. Rip, and D. D. Yue (1974). Theory of electric polarization. *Journal of The Electrochemical Society*. *121(6),* 211Ca.

[77] I. L. Al-Qadi, Z. Leng, S. Lahouar, and J. Baek (2010). In-place hot-mix asphalt density estimation using ground-penetrating radar. *Transportation research record*. *2152(1),* pp. 19-27.

[78] J. Behari (2005). *Dielectric Behavior of Soil*. Springer Netherlands. pp. 22-40.

[79] C. Warren, A. Giannopoulos, and I. Giannakis (2016). gprMax: Open-source software to simulate electromagnetic wave propagation for Ground Penetrating Radar. *Computer Physics Communications*. *209,* pp. 163-170.

[80] M. Gong, Y. Sun, and J. Chen (2021). Multi-scale analysis of asphalt pavement on curved concrete bridge deck considering effect of mesoscopic structure characteristics. *Construction and Building Materials*. *282*, 122724.

[81] M. Gong, Y. Sun, and J. Chen (2021). Mechanical response analysis of asphalt pavement on curved concrete bridge deck using a mesostructure-based multi-scale method. *Construction and Building Materials*, *285*, 122858.

[82] Q. Cao, and I. L. Al-Qadi (2021). Development of a numerical model to predict the dielectric properties of heterogeneous asphalt concrete. *Sensors*. *21(8),* 2643.

[83] Y. Cheng, H. Bi, Y. Gong, Y. Jiao, and X. Yang (2011). Comparative research on Superpave Gyratory Compaction method and Marshall Compaction method in the mix design of AC-16. In *Proceedings 2011 International Conference on Transportation, Mechanical, and Electrical Engineering (TMEE)*. pp. 2383-2385.

[84] Highway Department. The Government of the Hong Kong Special Administrative Region (2024). *Index of Provisionally Approved Mix Designs Anderson Asphalt Limited (Lam Tei Plant).*

[85] H. Nakanishi, M. O. Hamzah, M. M. Hasan, P. Karthigeyan, and O. Shaur (2019). Mix design and application of porous asphalt pavement using Japanese technology. In *IOP Conference Series: Materials Science and Engineering*. *512(1),* 012026.

[86] X. Sui, L. Cao, X. Ma, H. Wang, and Z. Dong (2020). Research on transversely isotropic permeability of asphalt pavement: Laboratory tests and computational simulation. *Construction and Building Materials*. *251,* 118958.

[87] Q. Huang, Z. Qian, J. Hu, and D. Zheng (2020). Evaluation of stone mastic asphalt containing ceramic waste aggregate for cooling asphalt pavement. *Materials*. *13(13)*, 2964.

[88] X. Wang, Z. Fan, L. Li, H. Wang, adn M. Huang (2019). Durability evaluation study for crumb rubber–asphalt pavement. *Applied Sciences*. *9(16),* 3434.

[89] T. Ji, P. Hao, H. She, K. Yang, H. Li, D. Wang, R. Kang, and J. Liu (2023). Durability behavior of asphalt mixtures in regard to material properties and gradation type. *Frontiers in Materials*. *10*, 1151479.

[90] G. Leucci, S. Negri, and M. T. Carrozzo (2003). Ground Penetrating Radar (GPR): an application for evaluating the state of maintenance of the building coating. *Annals of Geophysics*. *46 (3)*, pp 481-489.

[91] ASTM D6925-15 (2015). Standard test method for preparation and determination of the relative density of asphalt mix specimens by means of the superpave gyratory compactor.

[92] ASTM D2627 (2014). Standard test method for bulk specific gravity and density of non-absorptive compacted bituminous mixtures.

[93] ASTM D6752 (2004). Standard test method for bulk specific gravity and density of compacted asphalt mixtures using automatic vacuum sealing method.

[94] R. Roberts (2021). U.S. Patent No. 10,938,099. Washington, DC: U.S. Patent and Trademark Office.

[95] K. Hoegh, R. Roberts, S. Dai, and E. Zegeye Teshale (2019). Toward core-free pavement compaction evaluation: An innovative method relating asphalt permittivity to density. *Geosciences*. *9(7)*, 280.

[96] Y. Chen, F. Li, S. Zhou, and X. Zhang (2024). Improved density prediction model based on global optimization algorithm for GPR system. *Measurement. 237*, 115243.

[97] C. R. Rao, H. Toutenburg, C. R. Rao, and H. Toutenburg (1995). Linear models, New York: Springer, pp. 3-18.

[98] C. Le Bastard, V. Baltazart, Y. Wang, and J. Saillard (2007). Thin-pavement thickness estimation using GPR with high-resolution and superresolution methods. *IEEE Transactions on Geoscience and Remote Sensing*. *45(8)*, pp. 2511-2519.

[99] J. R. Birchak, C. G. Gardner, J. E. Hipp, and J. M. Victor (1974). High dielectric constant microwave probes for sensing soil moisture. *Proceedings of the IEEE*. *62(1)*, pp. 93-98.

[100] H. Looyenga (1965). Dielectric constants of heterogeneous mixtures. *Physica*. *31(3)*, pp. 401-406.

[101] Y. H. Huang (2004). *Pavement analysis and design*. *Vol. 2*, pp. 401-409.

[102] P. S. Kandhal, and S. Chakraborty (1996). Effect of asphalt film thickness on short-and long-term aging of asphalt paving mixtures. *Transportation Research Record*. *1535(1)*, pp. 83-90.

[103] A. Saltelli, M. Ratto, T. Andres, F. Campolongo, J. Cariboni, D. Gatelli, M. Saisana, and S. Tarantola (2008). Global sensitivity analysis: the primer.

[104] J. Herman, and W. Usher (2017). SALib: An open-source Python library for sensitivity analysis. *Journal of Open Source Software*, *2(9)*, 97.

[105] K. Hoegh, T. Steiner, E. Zegeye Teshale, and S. Dai (2020). Minnesota department of transportation case studies for coreless asphalt pavement compaction assessment. *Transportation Research Record*. *2674(2)*, pp. 291-301.

[106] S. Wang, Z. Leng, and X. Sui (2023). Detectability of concealed cracks in the asphalt pavement layer using air-coupled ground-penetrating radar. *Measurement*. *208*,112427.

[107] AASHTO, T 269 (2014). Standard method of test for percent air voids in compacted dense and open asphalt mixtures.

[108] J. Lachowicz, and M. Rucka (2019). A novel heterogeneous model of concrete for numerical modelling of ground penetrating radar. *Construction and Building Materials*, *227*, 116703.

[109] Z. Leng, and I. L. Al-Qadi (2010). Railroad ballast evaluation using ground-penetrating radar: laboratory investigation and field validation. *Transportation research record*. *2159(1)*, pp.110-117.